Using the Movability Number to model local clear-water scour in rivers

by

Benjamin Abban

A thesis submitted in partial fulfilment of the requirements for the degree of Master of Science in Engineering

Department of Civil Engineering
University of Cape Town

February 2007

Declaration

I, Benjamin Abban, understand the meaning of plagiarism and declare that all work in this dissertation, save for that which is properly acknowledged, is my own. Neither the whole work nor any part of it has been, or is to be submitted for another degree at this or any other university.

I empower the University of Cape Town to reproduce for the purpose of research the contents as a whole or in part in any manner whatsoever.

Signed by candidate

Benjamin Abban

14/02/07

Date

Acknowledgements

I first and foremost want to thank Associate Professor Neil Armitage for his supervision, encouragement, support and faith in me during my studies at the University of Cape Town. I also want to thank Dr Chris Meyer, Margie Cunninghame, Alamgir Kabir, Nic Gibson, Andrew McBride, Noor Hassen and Elvino Witbooi for their respective contributions and support towards the research. Finally, I would like to thank my parents, Mr and Mrs JF Abban, and my sisters, Rosemary, Catherine and Rita, for the immense love and support they gave me throughout the study period.

Abstract

Local scour is associated with a considerable number of bridge failures worldwide. It occurs at bridge piers and abutments as a result of interactions between complex flow features and the channel bed. The number of factors involved in the interactions makes it difficult to predict. A lot of research has therefore been performed by several investigators to gain insight into the scouring process and scour prediction. Currently, local scour is estimated using physical models, empirical formulae or numerical models. Of these methods, the use of numerical models appears to be more economical and ideal as it permits flexibility in the choice of flow parameters and allows different scenarios to be easily studied. The aim of this research was thus to investigation into the use of the commercial CFD code FLUENT 6.2 for scour prediction based on the Movability Number.

The research, which focused exclusively on local clear-water scour at bridge piers, stemmed from previous works performed by Armitage & McGahey (2003) and Cunninghame (2005) in which the Movability Number approach was developed and assessed. Results from these studies indicated that there was considerable potential in the Movability Number approach and, also, there was a need for a completely automated procedure for scour prediction based on the approach. For the current research therefore, an 'equilibrium model' was developed in which the river bed was successively modified in response to computed bed Movability Numbers until the final result reflected an equilibrium clear-water scour hole.

Unstructured grids were generated in GAMBIT 2.2 and imported into FLUENT for the simulations. The symmetry condition was applied and the grids were fined up in regions where large velocity gradients or changes in other fluid properties were expected. Before the clear-water scour evolution simulations were carried out, the performance of the standard k-ε model was compared with that of the Reynolds Stress model, and standard wall functions with non-equilibrium wall functions for a flat bed. Both turbulence models predicted similar scour patterns. Results of the numerical simulations were compared with data from a physical model and it was found that the non-equilibrium wall functions predicted scouring in regions on the bed where scour was not observed in the physical model. The standard wall functions, on the other hand, appeared to give realistic results. Since the standard k-ε model involved the solution of two transport equations whilst the Reynolds stress model involved the solution of seven, the former was used with the standard wall functions for the scour hole evolution simulations. It was believed that this would result in shorter simulation times. A scour potential was defined as the difference between a computed bed Movability Number and the critical Movability Number required for sediment movement. Scour was considered to occur at those locations where the scour potential values were greater than zero and the grid nodes were displaced in response. User-defined functions were written to perform the bed modifications and ensure the integrity of the mesh as the bed geometry changed.

Five physical scour experiments were simulated numerically. These physical experiments were performed as part of the research and were carried out in a 0.61m wide tilting flume in the Hydraulics laboratory of the Civil Engineering Department at the University of Cape Town. Results from the numerical simulations were compared with those from the physical models.

Although, the numerically estimated equilibrium scour depths were relatively close to those from the physical models, the shapes of the scour holes were not that similar. This was attributed to numerical difficulties in accurately predicting the flow field (and hence the Movability Numbers) at the bed. It was recommended that ways of improving the accuracy of the flow field prediction be found in order to accurately predict the bed Movability Numbers. In general, however, the Movability Number approach showed considerable potential for use in the prediction of local clear-water scour.

Table of contents

List of figures

List of tables

List of symbols

Symbol	Description	Unit
a	Largest triaxial dimension of sediment particle	m
a_n	nth interval	m
$\mathbf{a_n}$	Area normal vector	m^2
A	Cross-sectional area of flow	m^2
A^+	Damping constant	
b	Intermediate triaxial dimension of sediment particle	m
b_p	Pier breadth	m
B_c	Channel breadth	m
B_r	Roughness coefficient	
B_s	Roughness coefficient for sand	
c	Shortest triaxial dimension of sediment particle	m
c_p	Specific heat of fluid	
$\mathbf{c_f}$	Face centroid vector	m
C_d	Drag coefficient	
C, C_{diff}, C_D, C_k	Turbulence model constants	
C_s	Constant dependent on wall roughness	
C_{scour}	Coefficient in node displacement equation	m
C_1, C_2	Turbulence model constants	
C_μ, $C_{\varepsilon 1}$, $C_{\varepsilon 2}$	Turbulence model constant	
d	Sediment diameter	m
d_i	Median diameter of particle size interval	m
d_s	Maximum scour depth	m
d_{se}	Equilibrium scour depth	m
$d_{15.9}$	Sediment size for which 15.9% of the particles are finer	m
d_{50}	Median particle diameter	m
$d_{84.1}$	Sediment size for which 84.9% of the particles are finer	m
$\overline{d}$	Mean particle diameter	m
$\mathbf{e}$	Diagonal vector of bed face	m
$\mathbf{e_y}$	Unit vector in the vertical direction	m
E	Roughness coefficient	
$\mathbf{f}$	Diagonal vector of bed face	m
F_{Dcr}	Critical drag force for a given slope	N
F_{Dcr0}	Critical drag force for a horizontal bed	N
g	Acceleration due to gravity	m/s^2
$\mathbf{g}$	Gravity vector	m/s^2
h	Depth of flow	m
h_t	Fluid enthalpy	J
h_w	Head of water above weir	m
I	Intensity of motion	s^{-1}
k	Turbulent kinetic energy	m^2/s^2
k_r	Roughness height	m
k_s	Roughness height for sand	m
k_s^+	Dimensionless roughness height	
k_t	Thermal conductivity	W/(mK)
K_d	Empirical expression for sediment coarseness	

K_h	Empirical expression for flow shallowness	m
K_I	Empirical expression for flow intensity	
K_t	Empirical expression for time effects	
l	Mixing length	m
l_i	Mixing length for inner layer	m
l_o	Mixing length for outer layer	m
L	Distance from the bed to half the mean flow depth	m
L_m	Dissipation length scale	
$_m$	Denotes maximum value	
m	Number of particle displacements within time t	
m_{qp}	Mass transfer from fluid phase q to phase p	kg
Mn	Movability Number	
Mn_c	Critical Movability Number	
$Mn_{largest}$	Largest Mn on the bed	
n	Manning's coefficient	$sm^{1/3}$
n_b	Manning's roughness for bed	$sm^{1/3}$
n_g	Manning's roughness for glass side walls	$sm^{1/3}$
N	Number of grid nodes on a vertical line	
N_a	Total number of surface particles over sample area	
N_{dns}	Required number of grid points for direct numerical simulation	
o	Bed node vector	m
p	Pressure	N/m^2
p_i	Percentage by mass of particle size interval	
p	Bed node vector	m
P	Wetted perimeter	m
P_1, P_2	Pressure forces	N
P_i	Stream power input at a point	W/m^3
P_r	Power per unit volume required to keep particle in suspension	W/m^3
P_t	Stream power dissipated at a point	W/m^3
Pr_ε, Pr_k	Turbulent Prandtl numbers	
q	Vector on bed face in the longitudinal direction	m
Q	Flow rate	m^3/s
r	Ratio between two successive node intervals	
r	Bed node vector	m
R	Hydraulic radius	m
Re_d	Pier Reynolds number	
Re_f	Particle fall Reynolds number	
Re_h	Reynolds number based on channel height	
Re_k	Roughness Reynolds number	
Re_x	Local Reynolds number	
Re_*	Reynolds number based on shear velocity	
s	Bed node vector	m
S	Bed slope	m/m
S_f	Friction slope	m/m
$S_{\alpha q}$	Source term in continuity equation for phase q	
SF	Shape factor	
t	Time	s

t_e	Time taken to achieve equilibrium	s
$\mathbf{t}$	Vector on bed face in the transverse direction	m
T	Temperature	K
u_e	Edge velocity	m/s
u_p	Mean flow velocity at point P	m/s
u_*	Shear velocity	m/s
u_{*c}	Critical shear velocity	m/s
u_∞	Undisturbed approach velocity	m/s
u	Point velocity in x direction	m/s
U	Mean channel velocity	m/s
U_c	Critical mean velocity	m/s
v	Point velocity in y direction	m/s
ν_t	Eddy viscosity	Pa.s
$\mathbf{v}$	Velocity vector	m/s
V1, V2, etc	Vortices	
w	Point velocity in z direction	m/s
$\mathbf{w}$	Vector in horizontal plane	m
W	Weight of fluid element	N
x_u	User specified constant	
x	Distance from leading edge	m
y	Vertical distance from bed	m
y_{min}	Vertical distance – lower limit of integration	m
y_p	Distance from wall to point P	m
y^+	Wall unit	
y_0	Distance from bed where velocity magnitude is zero	m
z_0	Distance from wall where velocity magnitude is zero	m
α	Under-relaxation factor	
α_p	Volume fraction of phase p in a cell	
β	Longitudinal slope	°
β_t	Coefficient of thermal expansion	
χ	Function of Reynolds number	
δ	Thickness of viscous sub-layer	m
δ_{ij}	Kronecker delta	
δ_l	Thickness of laminar boundary layer	m
δ_t	Thickness of turbulent boundary layer	m
δ^*	Displacement thickness	m
$\triangle B$	Bed roughness factor	
$\triangle t$	Time step	s
$\triangle x$	Grid spacing	m
$\triangle \phi$	Computed change in ϕ	
$\triangle y$	Node displacement	m
$\triangle y_{max}$, $\triangle y_{max1}$	Maximum allowed node displacement	m
ε	Rate of viscous dissipation	m^2/s^3
ε_{ijk}	Permutation operator	
ϕ	Arbitrary fluid property	
ϕ_{max}	Maximum angle face makes with horizontal plane	°
ϕ_{old}	Old value of ϕ	

ϕ_r	Angle of repose	°
Φ	Energy dissipated per unit volume	W/m³
γ	Transverse slope	°
γ_w	Specific weight of water	N/m³
γ_s	Specific weight of particle	N/m³
γ_f	Specific weight of fluid	N/m³
κ	Von Karman constant	
λ	Coefficient of bulk viscosity	Pa.s
μ	Coefficient of dynamic viscosity	Pa.s
μ_b	Sum of laminar and turbulent viscosities	Pa.s
ψ	Slope correction factor	
ρ	Water density	kg/m³
ρ_f	Fluid density	kg/m³
ρ_s	Sediment density	kg/m³
σ	Standard deviation	
σ_g	Geometric standard deviation	
$\sigma(x)$	Factor to account for non-equilibrium streamwise flow evolution	
τ	Shear stress	N/m²
τ_c	Critical bed shear stress	N/m²
τ_{ij}	Shear stress in j direction with unit normal in i direction	N/m²
τ_k	Dissipation time	s
τ_l	Shear stress due to molecular viscosity	N/m²
τ_{meq}	Equilibrium shear stress	N/m²
τ_t	Shear stress due to turbulent fluctuations	N/m²
τ_w	Wall shear stress	N/m²
τ_{xy}	Shear stress in the longitudinal direction of flow	N/m²
τ_o	Bed shear stress	N/m²
θ	Bed inclination	°
ν	Kinematic viscosity	m²/s
ω	Settling velocity	m/s
ω_k	Rotation vector	
ω_{ke}	Specific rate of dissipation	s^{-1}
Ω	Scour potential	
$\Omega_{largest}$	Largest scour potential	
Ω_{limit}	User-specified scour potential limit	
$'$	Denotes fluctuating component	
$-$	Denotes mean flow quantity	

List of acronyms

Acronym	Meaning
A	Ahmed
ARSM	Algebraic Reynolds Stress model
CFD	Computational Fluid Dynamics
CPU	Central Processing Unit
DNS	Direct Numerical Simulation
FLOPS	Floating Point Operations Per Second
GPU	Graphics Processing Unit
HRIC	High Resolution Interface Capturing
LES	Large Eddy Simulation
MC	Melville & Chiew
MUSCL	Monotone Upstream-Centered Scheme of Conservation Laws
ODE	Ordinary Differential Equation
PDE	Partial Differential Equation
PISO	Pressure Implicit with Splitting of Operators
PRESTO	Pressure Staggering Option
PVC	Polyvinyl Chloride
QUICK	Quadratic Upstream Interpolation for Convective Kinetics
RAM	Random Access Memory
RANS	Reynolds Averaged Navier-Stokes
RNG	Renormalization group
RSM	Reynolds Stress model
SDOF	Six Degrees of Freedom
SGS	Subgrid-Scale
SIMPLE	Semi-Implicit Method for Pressure-Linked Equations
SIMPLEC	SIMPLE-Consistent
UDF	User-Defined Function
VOF	Volume of Fluid

Chapter 1
Introduction

Local scour is worldwide problem. It occurs at a considerable number of bridge sites and is a primary cause of failure. The protection of bridges against local scour is thus an essential part of design and construction. Many factors contribute to the development of local scour thereby making its estimation difficult. Consequently, a lot of research on local scour has been performed by different investigators to provide a better understanding of the scouring process and to suggest ways of estimating it. Despite the volume of research that has been performed, there is no universally accepted procedure for local scour prediction. At present, local scour is generally estimated using empirical formulae, physical models and/or computational models. Empirical formulae tend to give widely varying and inconsistent results whilst physical models are expensive to run and may give results distorted by scale effects. Computational models, on the other hand, are not bound by the same constraints and are likely to offer a better solution. Unfortunately, there is currently a lack of sufficient computing power for the accurate modelling of all the processes involved. Computing power is, however, growing rapidly and this is making the computational model alternative increasingly attractive. The promise that computational modelling holds has in fact made it the focus of research for the past couple of years e.g. Olsen & Melaaen (1993), Olsen & Kjellesvig (1998), Kothyari & Raju (2001), Yen *et al.* (2001), etc.

Most of the developed computational models for local scour prediction solve sediment transport equations in addition to the governing fluid flow equations. A problem with this approach is that the solution of the extra (sediment transport) equations imposes additional computational and memory loads on the machines. Incipient motion criteria may be used for the scour prediction instead of the sediment transport equations. They appear to be more attractive since no extra transport equations are solved and so memory requirements and computational time are significantly reduced. Incipient motion criteria alone can only be used for clear-water scour prediction and result in the maximum scour depth which is normally used in design. Armitage (2002) focused on this approach and developed a scour prediction model based on the Movability Number criterion (Liu, 1957). The viability of this model was assessed by McGahey (2001) and Cunninghame (2005) using the commercial CFD codes CFX 4.3 & FLUENT 6.2 respectively. The assessments involved the comparison of CFD predicted channel bed Movability Numbers with local scour data from physical experiments. Results from both investigations were encouraging enough to suggest that the Movability Number approach could be a viable option for scour prediction with the current crop of PCs.

Cunninghame (2005) went further to develop a scour prediction routine in which scour was estimated in stages. Based on the scour patterns suggested by predicted bed Movability Numbers at each stage, the domain mesh was manually modified in GAMBIT to reflect scour. The procedure was tedious and the routine was not continued until an equilibrium scour hole developed. The current research stems from the investigations performed by McGahey (2001), Armitage (2002) and Cunninghame (2005). The aim of the research was to develop an automated procedure for scour prediction based on the Movability Number approach. The commercial CFD code, FLUENT 6.2, was employed and adapted to achieve the aim. Physical experiments on local scour development were also performed in the laboratory to obtain data for the validation

of the numerical model. The outcomes of both the computational and physical studies are presented here.

Local scour results from interaction between the complex flow features that develop around a structure and the sediment which constitute the river bed. Knowledge of sediment transport is necessary in understanding the process of local scour. Sediment transport is dependent on the nature of the boundary layer, which is affected by the conditions of flow. The modelling approach adopted for all wall affected flows is also in turn dependent on the characteristics of the boundary layer. Chapter 2 thus begins with a discussion on the boundary layer and the shear stress and velocity distributions in open channel flow. It then goes on to introduce the concepts of sediment transport and local scour. Brief descriptions of some sediment properties are given. Incipient motion is introduced and the different approaches to incipient motion are touched on. This is followed by a discussion on the movability number approach. The different types of scour are then looked at briefly and the chapter is concluded with an explanation of local scour around bridge piers.

The use of computers to solve fluid flow problems is referred to as Computational Fluid Dynamics (CFD). Chapter 3 discusses the basic elements of CFD. It introduces the basic equations governing all CFD models, the various discretisation schemes, the different types of grids, and general numerical modelling issues related to CFD. The chapter concludes with a summary of previous attempts made at modelling local scour around bridge piers.

It is essential that every numerical model be assessed for its adequacy in producing results. Physical experiments were performed at the Civil Engineering Hydraulics laboratory of the University of Cape Town to obtain data for the verification of the numerical model. These experiments are described in Chapter 5. The laboratory equipment used is presented, and the approaches and criteria that were employed are explained.

The modelling approach used is very important as it determines the level of accuracy of the solution that is obtained. Chapter 6 elaborates on the numerical methodologies that were adopted for the scour prediction including, inter alia; the grid sizing, the free surface and turbulence models used, the near-wall treatment adopted, the boundary conditions that were applied, the user-defined functions that were developed, and the deformation models that were used.

The outcome and findings of the research are presented and discussed in Chapter 7. The conclusions drawn from the research are given in Chapter 8 and recommendations for future research are presented in Chapter 9.

Chapter 2
A review of local scour and associated phenomena

River flows are inherently two phase boundary layer affected flows in which sediment is continually being transported along the bed or in suspension by the moving water. The sediment particles interact with each other and the flowing fluid throughout the water column. These interactions are dependent on the physical and chemical properties of both the particles and the flowing fluid and may lead to scour. Scour, which is the removal of sediment particles from the river bed, around a pier is due to complex flow features which develop as a result of the presence of the pier. Understanding the boundary layer theory is essential in understanding sediment transport and the scouring phenomenon. The distributions of shear stress and velocity at the boundary dictate the nature of the sediment transport and the modelling approach that is used. This section starts with a description of the shear stress and velocity distributions in an open channel. It briefly describes the boundary layer and how it is formed. The sediment properties relevant to the research are then outlined. This is followed by an introduction to sediment transport. Various approaches have been used to predict whether or not there will be particle motion. These approaches are discussed briefly and the Movability Number approach is elaborated further. After this, the different types of scour are mentioned and the section is concluded with a discussion on the formation and evolution of the local scour hole.

2.1 Shear stress distribution

According to Massey & Smith (1998), real flow has two basic characteristics; i) there is no discontinuity of velocity within the flow, and ii) the velocity of the fluid relative to a solid surface is zero (no-slip condition). In open channel flow, the velocity increases with increasing distance away from the bed. As a result of the relative movement between the layers of fluid particles, shear stresses are present. Consider a steady uni-directional flow over a rough bed (Figure 2-1). The forces acting on the control volume *ABCD* are considered to be the hydrostatic pressure forces, P_1 & P_2, the weight of the fluid element, W, and the shear stress acting along BC, τ (Yalin, 1972)

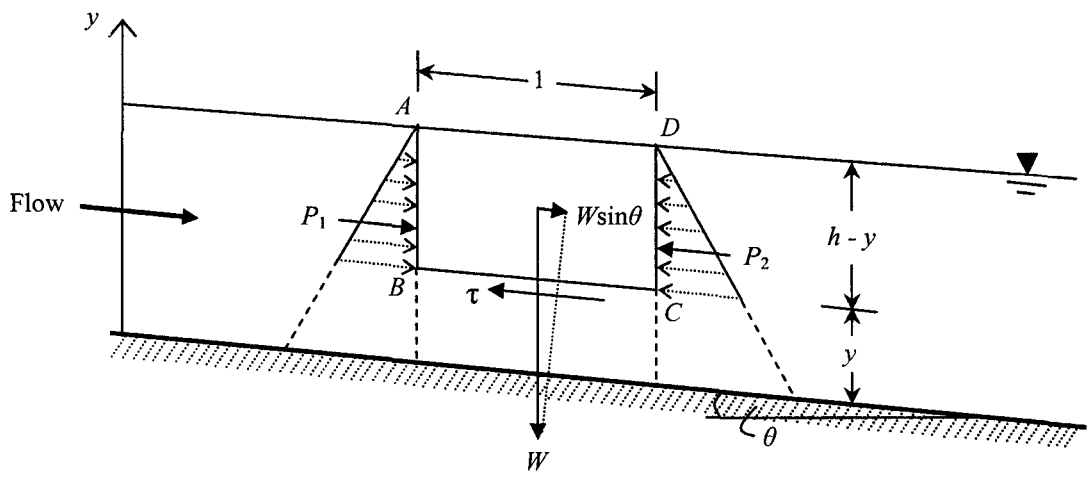

Figure 2-1: Uni-directional flow in an open channel

For uniform flow, the pressure forces are equal and so $P_2 - P_1 = 0$. Thus for equilibrium,

$$W \sin\theta - \tau = 0 \tag{2.1}$$

For small angles $\sin\theta \approx \tan\theta$. Letting $S = \tan\theta$ and considering that $W = \gamma_w(h - y)$ we get,

$$\gamma_w(h-y)S - \tau = 0 \tag{2.2}$$

Rearranging yields:

$$\tau = \gamma_w Sh\left(1 - \frac{y}{h}\right) \tag{2.3}$$

Hence the shear stress varies linearly with depth, increasing from 0 at the free surface to a maximum value, τ_0, at the bed. The maximum value is given as:

$$\tau_0 = \gamma_w Sh \tag{2.4}$$

The shear stress at a given point in the flow is considered to have two components; i) the laminar component, τ_l, which is due to molecular viscosity and ii) the turbulent component, τ_t which is due to turbulent fluctuations. The shear stress distribution through a fluid column is shown in Figure 2-2.

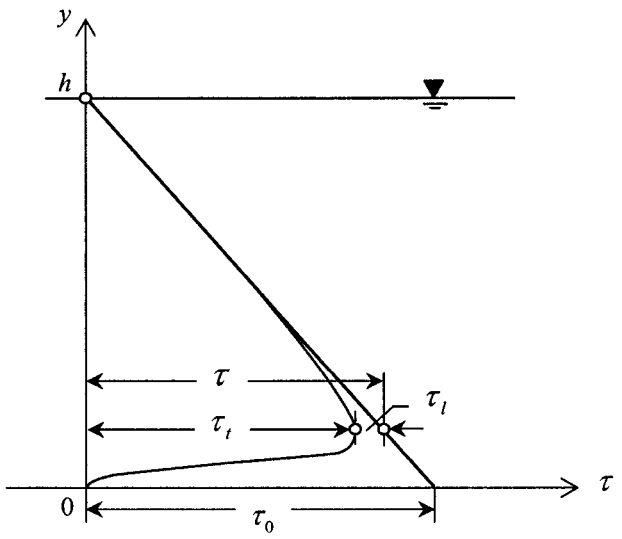

Figure 2-2: Shear stress distribution through a column of flowing fluid (adapted from Yang, 1996)

The laminar component is given by Newton's law of viscosity (Yalin, 1972; Massey & Smith, 1998; Nalluri & Featherstone, 2001; Chadwick *et al.*, 2004):

$$\tau_l = \mu \frac{\partial u}{\partial y} \tag{2.5}$$

where μ is the coefficient of dynamic viscosity and $\partial u/\partial y$ is the velocity gradient. The turbulent component is dependent on fluctuating flow velocities with components in both the horizontal and vertical directions. Several relationships have been used to represent the turbulent component. A simple and popular one is the mixing length model. In a bid to relate the rate of momentum transfer to the mean pattern of flow, Prandtl (1925) introduced the mixing length theory. In this theory, a characteristic linear dimension, l, called the mixing length is considered to represent the average distance a small mass of fluid (moving towards a region of lower velocity) will travel before it loses its extra momentum and take on the mean velocity of the region into which it flows. Based on this theory, Prandtl's mixing length model may be expressed as follows (Rouse, 1939; Massey & Smith, 1998):

$$\tau_t = \rho l^2 \left|\frac{\partial u}{\partial y}\right| \frac{\partial u}{\partial y} \tag{2.6}$$

where ρ is the density of the fluid. According to White (1991), Prandtl and von Karman developed three relationships for l. In the region of flow where viscous shear dominates, it was determined that $l \approx y^2$. The value of l for the region where turbulent shear dominated was found to be constant. In the region where both types of shear were important, the relationship was determined to be $l \approx \kappa y$, where κ is known as the von Karman constant.

Turbulent action in a flowing fluid reduces as the boundary is approached. Close to the bed, the velocity gradients are large and viscous effects are significant. Turbulent action here is small and the shear stress is mainly due to the laminar component (viscous effects). The significance of viscous effects reduces with increasing distance from the bed as turbulence increases and momentum transfer between small fluid elements become greater. The velocity gradients in the more turbulent regions are smaller as the velocity distributions are more uniform. In these zones, viscous effects are less significant and the shear stresses are mostly due to turbulent fluctuations. This is seen in Figure 2-2.

2.2 Boundary layer

Prandtl suggested in 1904 that flow could be considered in two parts; i) flow in the so-called *boundary layer* where shear stresses are of importance (inner layer), and ii) flow beyond the boundary layer (outer layer) where velocity gradients are normally small and so viscous effects are negligible (Liu, 1957; Massey & Smith, 1998).

The boundary layer is the region close to the bed where the velocity increases rapidly and approaches that of the main stream. The rapid change in velocity is due to the fact that the velocity of the fluid relative to the bed should be zero. The development of boundary layer is described in the following paragraph.

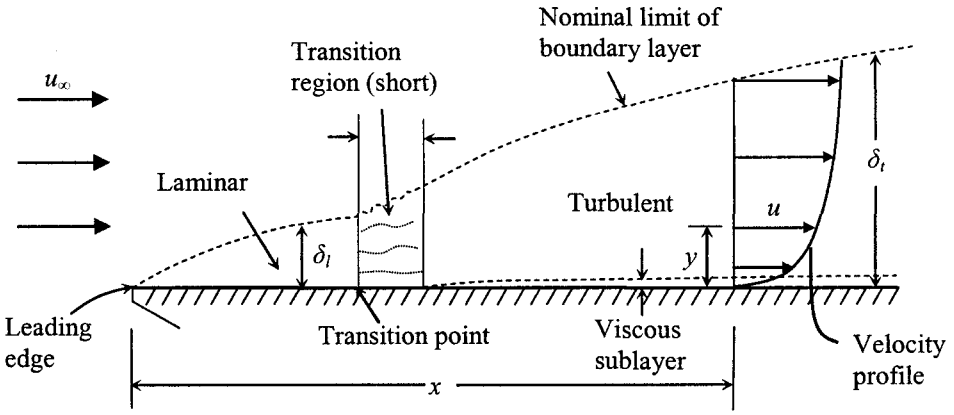

Figure 2-3: Boundary layer along a smooth flat plate (adapted from Liu, 1957, and Massey & Smith, 1998)

Consider flow over a thin, smooth flat plate. It is assumed that the plate is parallel to the oncoming fluid and there is a zero pressure gradient. As the fluid flows over the leading edge of the plate, the fluid close to the surface is retarded due to viscous friction giving rise to the boundary layer. With increasing distance from the leading edge, more of the fluid is retarded as a result of shearing action and the thickness of the boundary layer increases. Flow in the boundary layer is thus far laminar and the velocity gradients are large. The thickness of the wholly laminar boundary layer, δ_l, may be determined from (French, 1994):

$$\delta_l = \frac{5x}{\sqrt{Re_x}} \tag{2.7}$$

where x is the distance from the leading edge and Re_x is a Local Reynolds Number defined as:

$$Re_x = \frac{u_\infty x}{\nu} \tag{2.8}$$

where u_∞ is the undisturbed approach velocity and ν is the kinematic viscosity.

The laminar flow becomes increasingly unstable with the increasing thickness of the layer. It gets to the point where the flow becomes turbulent. Even under this condition, a thin layer of flow exists right next to the surface that is laminar (See Figure 2-3). This region is referred to as

the viscous sub-layer. According to Massey & Smith (1998), transition is difficult to prevent at $Re_x > 2 \times 10^6$. Nalluri & Featherstone (2001) state that turbulence generally occurs at $Re_x = 5 \times 10^5$. French (1994) suggests that the transition generally takes place between 5×10^5 and 10^6. The change from laminar flow to turbulent flow occurs over a very short distance and this region is referred to as the transition region. The velocity gradients in the boundary layer reduce with increasing distance from the surface and the velocity approaches that of the main stream at the boundary layer fringes. In reality, there is no definite limit of the boundary layer. It is generally assumed that the boundary layer extends to the point at which the velocity is 99% of the main stream velocity (Liu, 1957; Massey & Smith, 1998; Chadwick *et al.*, 2004). The velocity distribution through the turbulent layer is also shown in Figure 2-3. The approximate thickness of the turbulent boundary layer, δ_t, for $Re_x < 10^7$ may also be determined from (White, 1991):

$$\delta_t \approx \frac{0.37x}{Re_x^{0.2}} \tag{2.9}$$

The presence of roughness elements on the solid surface may have an effect on the boundary layer and flow in the main stream. If the main stream flow is laminar, roughness has no effect as the shearing action is solely due to viscosity throughout the fluid. In the case of turbulent flow, if the average height of roughness is smaller than the viscous sub-layer, the viscous sub-layer dampens the impact of the roughness and so there is little or no effect on the turbulent region. If the roughness elements protrude beyond the viscous sub-layer into the turbulent region, they will shed eddies and the turbulent component of shear stress will increase close to the surface (Nalluri & Featherstone, 2001; Chadwick *et al.*, 2004).

2.3 Velocity distribution for turbulent mean flows

Yalin (1972) illustrates the derivation of the velocity distribution in the turbulent region of flow by representing the mixing length, l, in Prandtl's model with κy and integrating Equation 2.6 from y_{min} to y, where y_{min} is the lower limit equal to the larger of the thickness of the viscous sublayer, δ, and the height of roughness, k_r. Considering the relative size of the viscous sub-layer thickness to the roughness height in the analysis, the following relationship for the velocity distribution is obtained:

$$\frac{u}{u_*} = \frac{1}{\kappa} \ln \frac{y}{k_r} + B_r \tag{2.10}$$

Where u is the velocity at a depth y and u_* is the shear velocity given by:

$$u_* = \sqrt{\frac{\tau_0}{\rho}} \tag{2.11}$$

The value of B_r is dependent on the value of the roughness Reynolds number, $Re_k = u_* k_r / \nu$. Nikuradse (1933) determined the relationship between B_r and Re_k for equal size sand grains tightly glued on the boundary. Figure 2-4 indicates the relationship that was observed. The variables B_r and k_r are substituted with B_s and k_s respectively for sand.

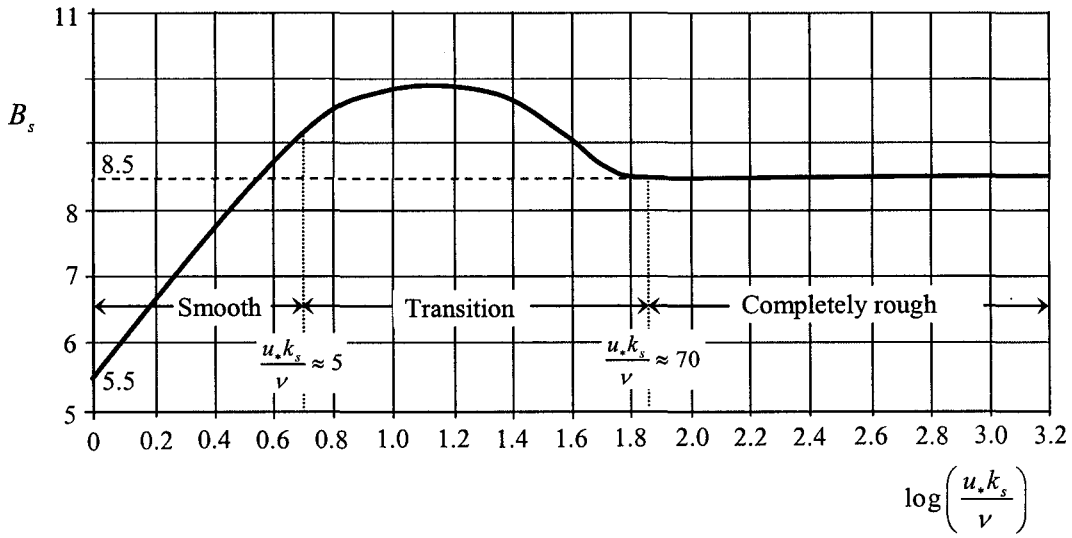

Figure 2-4: Relationship between B_r and k_r for uniform sand (after Nikuradse, 1933)

From Nikuradse's (1933) experiment it was noted that

For $Re_k < 5$:

$$B_s = 2.5 \ln \frac{u_* k_s}{\nu} + 5.5 \tag{2.12}$$

For $Re_k > 70$:

$$B_s = 8.5 \tag{2.13}$$

According to Van Rijn (1993), turbulent flows corresponding to $Re_k < 5$ are referred to as *hydraulically smooth flows*. These flows are characterised by the fact that the velocity distribution is independent on the size and nature of the roughness elements. This can be seen by substituting Equation 2.12 into Equation 2.10 and taking κ as 0.4. The result, Equation 2.14, is a relationship which is independent of roughness.

$$\frac{u}{u_*} = 2.5 \ln\left(\frac{u_* y}{\nu}\right) + 5.5 \tag{2.14}$$

Fully developed turbulent flows or *rough turbulent flows* are those flows in which $Re_k > 70$. The velocity in this type of flow is dependent on roughness and independent of molecular viscosity. The roughness elements are exposed to the turbulent region of flow, hence the term fully developed turbulent flow. Turbulent flow given by the condition $5 < Re_k < 70$ is considered to be in a *transitional regime.* The velocity distribution for a transitional regime is dependent on both the viscosity and roughness (Van Rijn, 1993).

For hydraulically smooth flows, the relationship between the dimensionless velocity and the dimensionless depth within the viscous sub-layer is linear (Yalin, 1972) i.e.

$$\frac{u}{u_*} = Re_* \frac{y}{h} = \frac{u_* y}{\nu} \tag{2.15}$$

where $Re_* = u_* h/\nu$. The equations for hydraulically smooth flows are also presented by Versteeg & Malalasekera (1995), Chanson (2004), Fluent (2005) etc. The velocity distribution for hydraulically smooth flows is shown in Figure 2-5. Both axes are represented in dimensionless quantities.

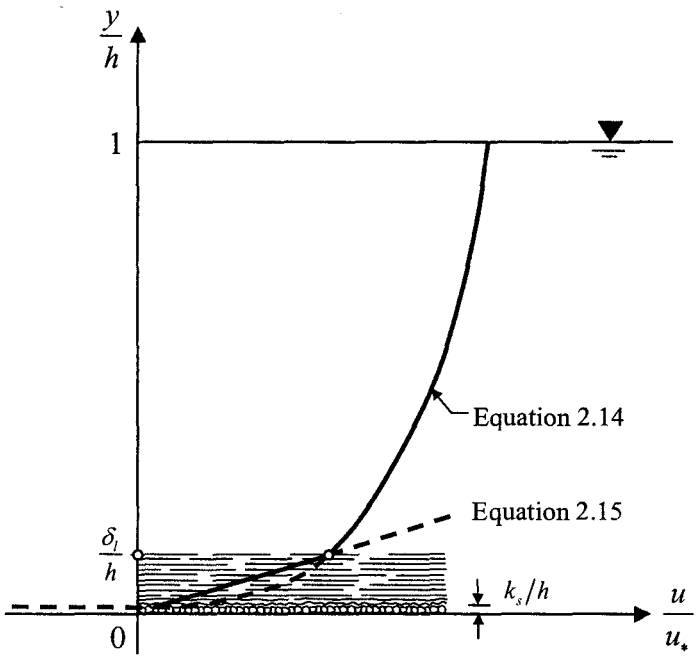

Figure 2-5: Velocity distribution – hydraulically smooth flows (after Yalin, 1972)

It can be deduced from Equations 2.10 & 2.13 that the velocity distribution for rough turbulent flow is dependent on the height of roughness. Substituting $B_r = 8.5$ into Equation 2.10 results in a velocity distribution equation that is different from that of a hydraulically smooth flow. The distribution is however still logarithmic as shown in Figure 2-6.

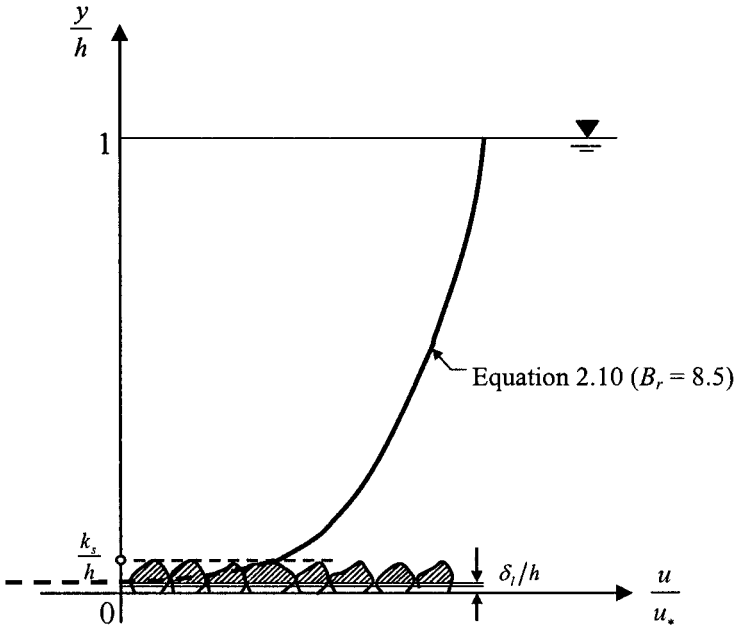

Figure 2-6: Velocity distribution – rough turbulent flows (after Yalin, 1972)

It can be noted in Figure 2-5 that Yalin (1972) ignored the fact that there is a transitional region between the viscous sub-layer and the turbulent layer. Figure 2-7 is adapted from Schlichting & Gersten (2000). It illustrates the velocity profiles within the different sub-layers of the boundary layer. At present, there is no obvious relationship for the velocity distribution within the transitional regime. Some investigators simply assume that the viscous sub-layer and the turbulent region coincide at a value of $u_* y / \nu$ between 11 and 13 (Yalin, 1972; Rooseboom, 1992). Fluent (2005) suggest that 11.8 is a generally accepted value. Curves are also sometimes used to smoothly link the viscous sub-layer to the transition layer (Reynolds, 1974).

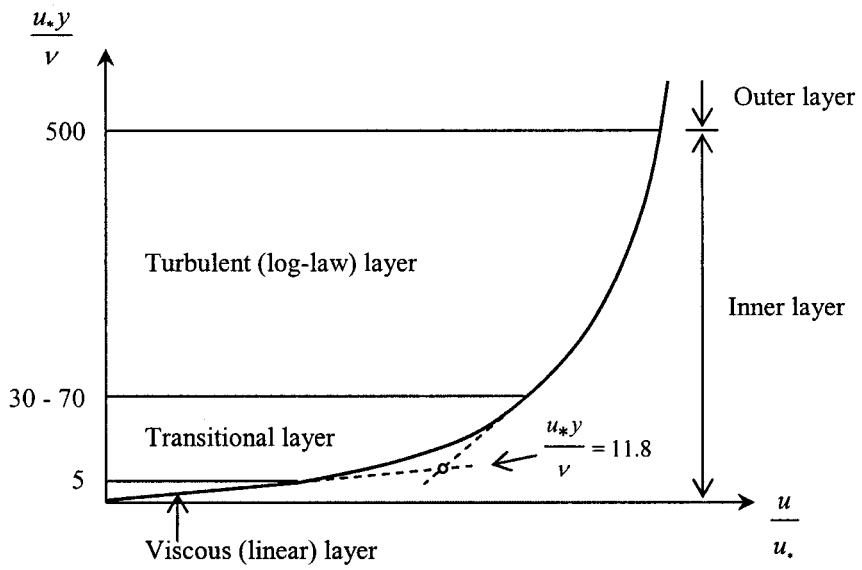

Figure 2-7: Velocity distribution – inner layer (after Schlichting & Gersten, 2000)

The outer region occurs at $u_* y/\nu > 500$. The velocity distribution within this region is more dependent on the bed slope, flow depth, maximum flow velocity and large scale eddies instead of molecular viscosity and boundary roughness (Graf, 1998).

2.4 Sediment properties

2.4.1 Sediment size

According to Julien (2002), the size of a sediment particle is its most important physical property. The size of a sediment particle, among others, dictates the ease with which it will be transported. Sediment size is easily defined and, depending on the definition being used, may be relatively easy to determine. Several definitions have been used to describe sediment size. These include (Yang, 1996; Raudkivi, 1998; Julien, 2002):

- Sieve diameter – this is the length of the side of a mesh square opening through which the sediment particle will just pass.
- Sedimentation diameter – this is the diameter of a sphere with the same density and fall velocity as the particle in the same fluid and at the same temperature.
- Nominal diameter – this is the diameter of a sphere with the same volume as the sediment particle and is usually determined by the volume the particle displaces.
- Standard fall diameter – is the diameter of a sphere of specific gravity of 2.65 with the same fall velocity as the particle in quiescent distilled water of infinite extent at a temperature of 24°C.
- Triaxial dimensions – these are lengths a, b and c along three mutually perpendicular axes through the particle such that a is the longest, b is intermediate and c is the shortest.

Generally, the definition used depends on the particle size e.g. the sieve diameter may be used for particles sizes ranging between cobbles and fine sand whereas the sedimentation or standard fall diameter may be used for sediment finer than fine sand (Chien & Wan, 1999).

2.4.2 Shape

The form which a particle takes is also important in the study of sediment transport. One common definition used to account for particle shape is given as follows (Yang, 1996; Raudkivi, 1998):

$$SF = \frac{a}{\sqrt{bc}} \tag{2.16}$$

where SF is the shape factor. Applying Equation 3.1, a perfectly spherical particle will yield a shape factor of 1. It has been determined that naturally worn quartz particles have an average shape factor of 0.7 (Yang, 1996). According to Armitage & McGahey (2003), the shape factor is used to take the deviation of a particle from the spherical into account as it is generally assumed that particles are reasonably spherical.

2.4.3 Fall velocity

This is the terminal velocity that a particle attains in a quiescent column of water that is unbound. The fall velocity is dependent on particle size, shape, surface roughness, density, and viscosity and density of the fluid. The fall velocity, ω, is also influenced by fluid boundaries, turbulence intensity levels and particle concentration (Yang, 1996; Raudkivi 1998). The expression for fall velocity is based on considerations of the balance between fluid drag and the submerged particle weight and is given as follows (Raudkivi, 1998; Chien & Wan, 1999):

$$\omega = \sqrt{\frac{4}{3}\frac{\rho_s - \rho}{\rho}\frac{gd}{C_d}} \tag{2.17}$$

where ρ_s is the sediment density, d is the sediment diameter, and C_d is the drag coefficient which is dependent on the particle fall Reynolds number defined as follows (Chien & Wan, 1999):

$$Re_f = \frac{\omega d}{\nu} \tag{2.18}$$

The change in C_d is small at Re_f values greater than 1000. The fall velocity is thus considered to be independent of viscosity when Re_f exceeds 1000 (Raudkivi, 1998; Chien & Wan, 1999).

The fall velocity may also be read off a chart drawn up by the Sedimentation Subcommittee of the US Inter-Agency Committee on Water Resources. The chart relates the particle fall velocity to shape factor, temperature and sieve diameter and may be found in standard references (e.g. Yang, 1996; Raudkivi, 1998). It is shown in Figure 2-8.

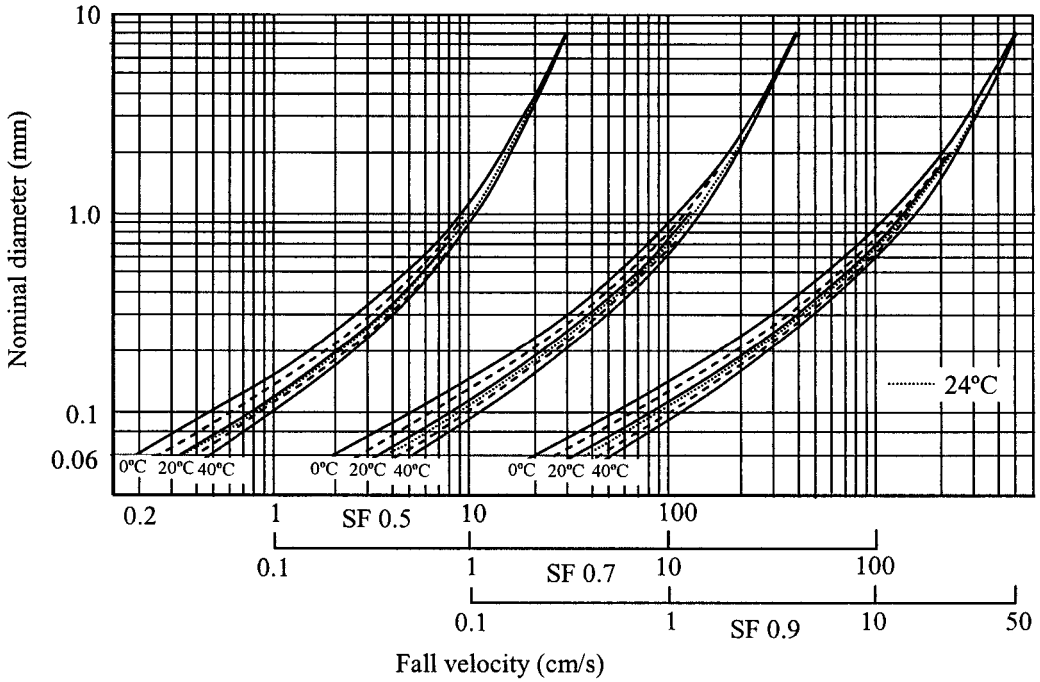

Figure 2-8: Chart for estimation of the fall velocity (after Yang, 1996)

2.4.4 Particle size distribution

The sizes of individual sediment particles in a group usually vary. As a result, sediment size is normally analysed using statistical methods. Parameters such as the mean size, standard deviation, skewness etc. are determined for a number of samples in order to obtain the characteristic properties of the group of particles. A common way of presenting sediment size is to plot a particle size-frequency distribution or a cumulative distribution curve as shown in Figure 2-9. In size-frequency distribution curves, particle size is divided into intervals and the percentage of the group falling within each interval is plotted as a function of size. Cumulative distribution plots typically show the percentage of particles finer than the individual sediment sizes (Raudkivi, 1998, Chien & Wan, 1999).

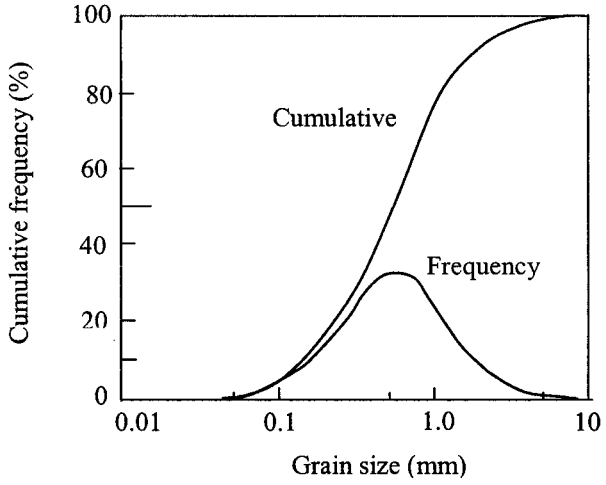

Figure 2-9: Cumulative and frequency distribution plots for particle size (after Chien & Wan, 1999)

The most common statistical definitions relating to size distribution are summarized by Armitage & McGahey (2003) as follows:

Median diameter (d_{50}): this is the particle diameter that is exceeded by exactly 50% of the material by mass. For a skewed size distribution, d_{50} is usually calculated as follows:

$$d_{50} = \frac{d_{15.9} + d_{84.1}}{2} \tag{2.19}$$

Where $d_{15.9}$ and $d_{84.1}$ are the sediment sizes for which 15.9% and 84.1% of the particles are finer by mass respectively.

Mean diameter ($\overline{d}$): this is the arithmetic mean of the particle sizes. If d_i is the median diameter of any particular size interval and p_i is the percentage by mass of that interval then:

$$\overline{d} = \frac{\Sigma p_i d_i}{100} \tag{2.20}$$

Standard deviation (σ): this generally defined as:

$$\sigma = \frac{\Sigma p_i \sqrt{d_i - \overline{d}^2}}{100} \tag{2.21}$$

d_{50} may be substituted for $\overline{d}$.

Geometric standard deviation (σ_g): According to Yang (1996), examination of a large number of sediment samples indicates that the size-frequency distribution curve approximates a normal probability curve. If the particle size distribution is assumed to be normally distributed, the geometric standard deviation may be determined as follows:

$$\sigma_g = \sqrt{\frac{d_{84.1}}{d_{15.9}}} = \frac{d_{84.1}}{d_{50}} = \frac{d_{50}}{d_{15.9}} = \frac{1}{2}\left(\frac{d_{50}}{d_{15.9}} + \frac{d_{84.1}}{d_{50}}\right) \tag{2.22}$$

Sediment is considered to be uniform if the geometric standard deviation is less than 1.3 (Melville, 1997).

2.4.5 Cohesiveness

Sediment particles are generally considered to be either cohesive or non-cohesive. Cohesive sediment, generally made up of particles smaller than $2\mu m$, have large specific surface areas (i.e. surface area per unit volume) and form a coherent mass. Sediment transport in this case is dominated by electro-chemical interactions between the particles and not the individual particle sizes and weights. Non-cohesive particles on the other hand are granular in nature and do not form a coherent mass. Sediment transport is affected mainly by particle size and weight. As stated before, sediment sizes in an assembly of sediment vary. The cohesiveness of a group of sediments increases with the percentage of very fine particles. According to Raudkivi (1998), cohesive effects become significant when this percentage is as small as 10%. (Raudkivi, 1998; Chien & Wan, 1999).

2.4.6 Angle of repose

The angle of repose is defined by Yang (1996) as the angle of slope formed by a given material under the condition of incipient sliding. This is the maximum angle the surface of a pile of particles can sustain before the particles begin to slide down. The angle of repose has been found to be dependent on the particle size and roundness. It tends to increase with increasing size and angularity. Migniot (1968) determined that the angle of repose was between 31° and 40° for submerged sand and small gravel. Values of the angle of repose for cohesionless sediment particles may be determined from the chart prepared by Lane (1953) which can be found in Chien & Wan (1999). This chart relates the angle of repose to particle size and roundness. Values for quartzitic sand suggested by Van Rijn (1993) are shown in Table 2-1.

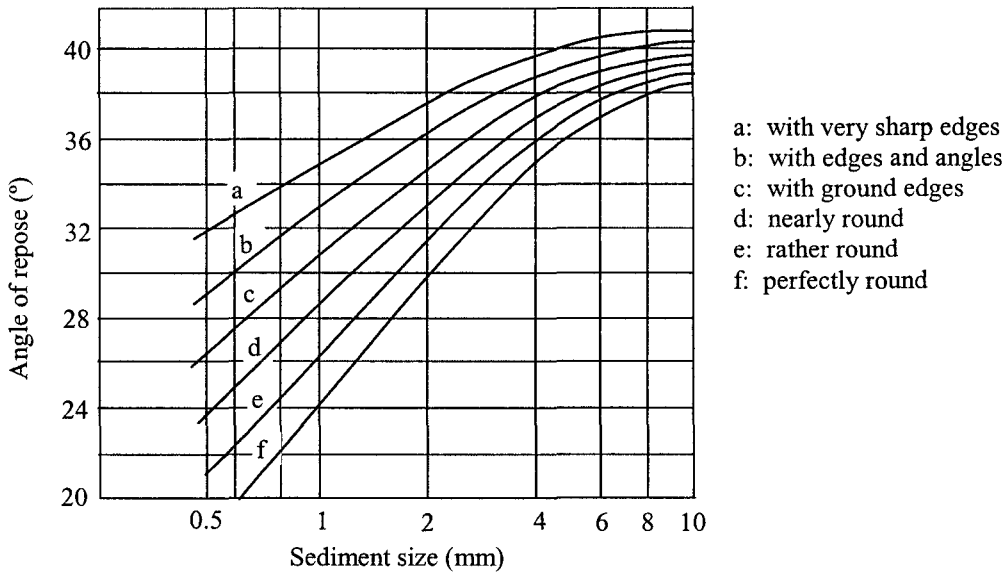

Figure 2-10: Angle of repose of cohesionless sediment particles (after Lane, 1953)

Table 2-1: Angle of repose of quartzitic sand (after Van Rijn, 1993)

Size (d_{50}) (mm)	Angle of repose (ϕ_r)	
	Rounded	Angular
≤1	30	35°
5	32	37°
10	35	40°
50	37	42°
≥100	40	45°

2.5 Incipient motion

A particle begins to move when the resultant force acting on it is strong enough to dislodge it from its position on the bed. The term incipient motion is generally used to describe the condition when sediment just begins to move as a result of the flowing fluid. Incipient motion depends on a number of factors. These include, inter alia, sediment size, shape, specific gravity, location, orientation and fluid turbulence. Typically, most of these factors vary with location and time. Incipient motion is thus stochastic in nature and the determination of flow conditions which bring about incipient motion is not straightforward. The forces acting on a particle and the probability of incipient motion are discussed here.

2.5.1 Forces on a cohesionless particle

Consider a particle lying at rest on a river bed as shown in Figure 2-11. The main forces acting on this particle are the lift and drag forces both of which are balanced by its submerged weight. The lift and drag forces come about as a result of fluid flow.

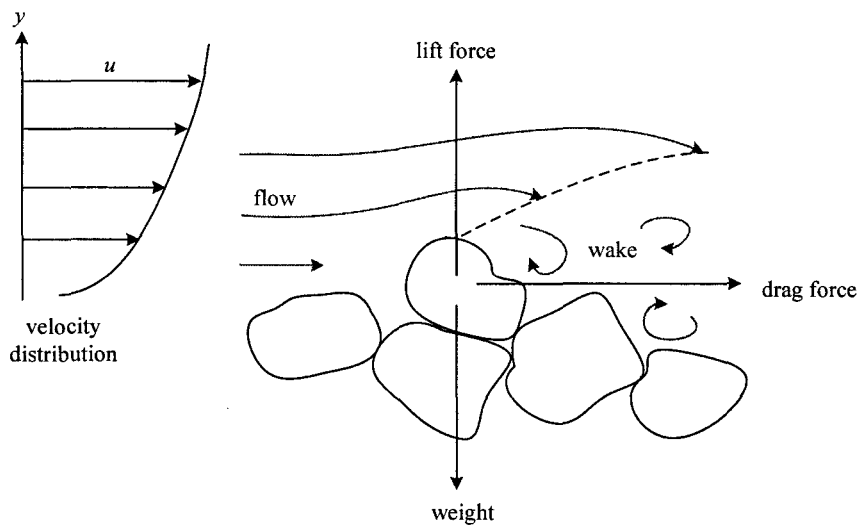

Figure 2-11: Forces acting on a river bed particle (after Chadwick *et al.*, 2004)

When there is no flow, only the submerged weight acts on the particle. As the fluid begins to move over the particle, shear stresses exist on the particle surface as a result of the flow. These shear stresses are directly proportional to the local velocity (velocity near bed) gradients and act tangential to the particle surface. The result of the sum of all the shear stresses is a drag on the particle known as the surface drag. In accordance with Bernoulli's principle, the magnitude of the pressure force acting on a particle is dependent on depth and local velocity. Only hydrostatic pressure forces act on the particle when the fluid is still. With increasing local flow velocity comes flow separation. The particle sheds eddies and a wake is formed in the lee of the particle. This results in pressure differences between the front and the back of the particle. The pressure differences give rise to what is known as the form drag. This form drag is a resultant of all the pressure forces acting on the particle. The total drag acting on the particle is then due to both surface drag and form drag. The vertical and horizontal components of the total drag give what are referred to as the lift and drag forces respectively. (Raudkivi, 1998; Chadwick *et al.*, 2004)

In addition, seepage of water into the bed gives rise to seepage (pressure) forces which will affect the resultant force on the particle. Resistance to the lift and drag forces may also be due to particle contact with other particles. As can be seen in Figure 2-12, some particles (i.e. the shaded particles) will be easier to remove than others as a result of their positioning (Chien & Wan, 1999).

Figure 2-12: Sediment particles on river bed (after Chien & Wan, 1999)

In the presence of turbulence, there are fluctuations in the lift and drag forces as a result of fluctuating local velocities and pressure. Entrainment of a particle may come about as a result of an instantaneous increase in the total drag, which causes the ejection of the particle from its position on the bed. An instantaneous drop in the local pressure may also result in the ejection of a particle due to hydrostatic pressure.

2.5.2 Approaches to incipient motion

There are various models used to predict when motion will take place. Most of them are related to a single flow parameter that is considered to play a dominant role in predicting whether or not motion would occur. The three primary parameters that are used often are velocity, bed shear stress and stream power (Chien & Wan, 1999). Approaches based on these parameters are described in the following subsections.

2.5.2.1 Velocity approaches

Velocity approaches generally express incipient motion in terms of either the local or the mean stream velocity. One of the early studies on the maximum permissible mean stream velocity for

canal design was by Fortier & Scobey (1926). Yang (1996) states that there is no theoretical support for the studies and recommends that the results be used only for preliminary designs.

Hjulstrom (1935) studied sediment transport in uniform material and presented a chart for erosion, transportation and sedimentation which related sediment size to mean velocity. Vanoni (1977) also presented a similar chart (Figure 2-13), which is recommended for stable channel design by the American Society of Civil Engineers Sedimentation Sub Committee.

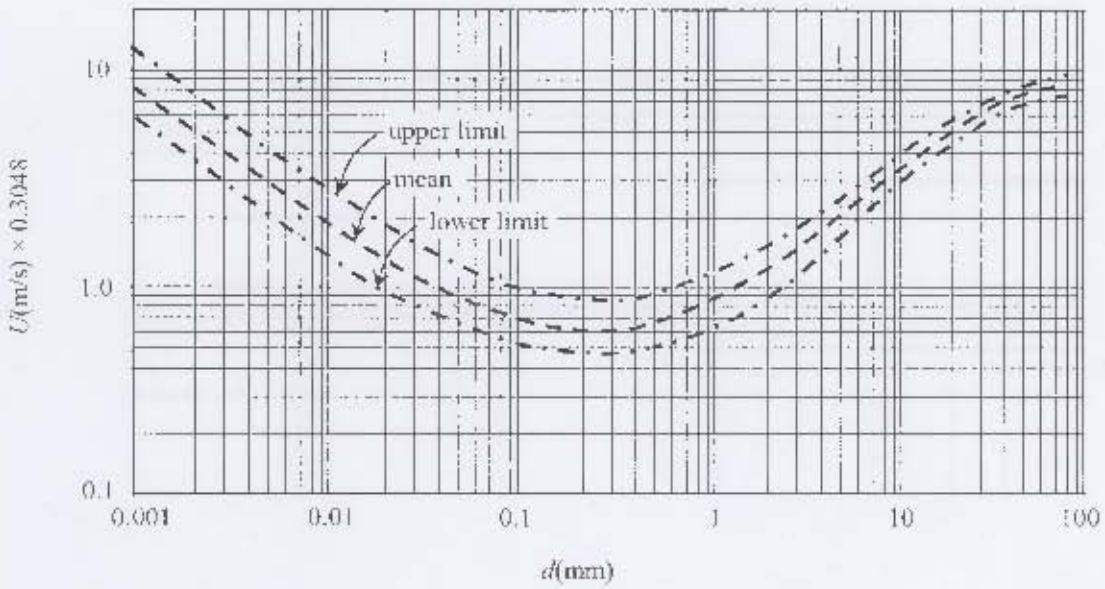

Figure 2-13: Chart for stable channel design (after Vanoni, 1977)

According to Chien & Wan (1999), most of the formulas for incipient motion in natural sediment based on critical mean velocity are generally of the form:

$$\frac{U_c}{\sqrt{gd}} = (1.28 - 1.79)\log 12.27\frac{\chi R}{k_s} \tag{2.23}$$

where R is the hydraulic radius of the channel and $\chi = f(u_*d/\nu)$. A summary of formulae by Knoros (1958), Li (1959), and Zeng *et al.* (1963) are presented by Chien & Wan (1999).

Melville (1997) studied flow around bridge piers and abutments and suggested the following formula for critical mean velocity when the sediment sizes are uniform:

$$\frac{U_c}{u_{*c}} = 5.75\log\left(5.53\frac{h}{d_{50}}\right) \tag{2.24}$$

where u_{*c} is the critical shear velocity based on d_{50}. It is given as follows:

For 0.1mm < d < 1mm:

$$u_{*c} = 0.0115 + 0.0125 d_{50}^{1.4} \tag{2.25a}$$

For 1mm < d < 100mm:

$$u_{*c} = 0.0305 d_{50}^{0.5} - 0.0065 d_{50}^{-1} \tag{2.25b}$$

Yang (1996) assumed a turbulent boundary and began his analysis with the local velocity. This local velocity was however integrated over the depth to obtain the average velocity. The final relationship therefore includes a dimensionless parameter based on the average velocity. Using Laboratory data from different investigators together with the theoretical considerations Yang (1996) presents the following formulae for incipient motion:

For $1.2 < u_* d/\nu < 70$:

$$\frac{U_c}{\omega} = \frac{2.5}{\log(u_* d/\nu) - 0.06} + 0.66 \tag{2.26a}$$

For $u_* d/\nu \geq 70$:

$$\frac{U_c}{\omega} = 2.05 \tag{2.26b}$$

According to Yang (1996), the relationships have been independently verified by Govers (1987), for laminar flow, and Talapatra & Gosh (1983), for turbulent flow.

The use of the mean flow velocity as a criterion for incipient motion has also come under some criticism. According to Armitage (2002), the lift and drag forces are dependent on the velocity distribution and not the mean velocity. Raudkivi (1998) explains that the bed shear stress for a given mean velocity decreases with increasing depth of flow. This means that incipient motion will occur at higher mean velocities for relatively deeper channels compared to shallow channels with similar boundary conditions. The use of near-bed local velocity is thus a better option compared with the mean velocity. The problem with its use, however, is the fact that it is difficult to determine. The high velocity gradients near the bed and the irregular roughness elements make it difficult to define an elevation at which the velocity should be determined. Determination of the effective boundary location is made further difficult by changes in the nature of the boundary layer (Raudkivi, 1998).

2.5.2.2 Shear stress approaches

Shear stress approaches express incipient motion in terms of the bed shear stress. White (1940) derived the following relationship to determine the critical bed shear stress at which incipient motion would take place.

$$\tau_c = C\left(\gamma_s - \gamma_f\right)d \tag{2.27}$$

where τ_c is the critical bed shear stress, d is the particle diameter, C is a constant dependent on the particle density and shape, and γ_f and γ_s are the specific weights of water and the particle respectively. The slope and the lift forces were considered to have an insignificant influence on incipient motion and so were neglected in its derivation (Equation 2.27).

The modified Shields relationship is perhaps the most popular shear stress approach to incipient motion. Shields in 1936 used dimensional analysis to derive a relationship which could be used to predict incipient motion. According to Shields (1936), the quantities important for incipient motion are the shear stress, τ, the difference in density between sediment and fluid, $\rho_s - \rho_f$, the particle diameter, d, the kinematic viscosity, ν and the acceleration due to gravity, g. Shields (1936) neglected the effects of the lift force and obtained the following relationship:

$$\frac{\tau_c}{d\left(\rho_s - \rho_f\right)g} = f\left(\frac{du_*}{\nu}\right) \tag{2.28}$$

Shields (1936) determined the relationship between the two quantities (LHS & RHS) experimentally using four different materials. These were amber (ρ_s = 1.06), brown coal (ρ_s = 1.27), granite (ρ_s = 2.7) and barite (ρ_s = 4.25). The product of the experiments was the well known Shields diagram, which indicates the threshold of movement. The modified Shields diagram is shown in Figure 2-14. It is based on work carried out by Shields (1936) and several other investigators. Shields (1936) originally did not fit a line to the experimental data. Extra data points and the line were added later based on experiments performed by other investigators.

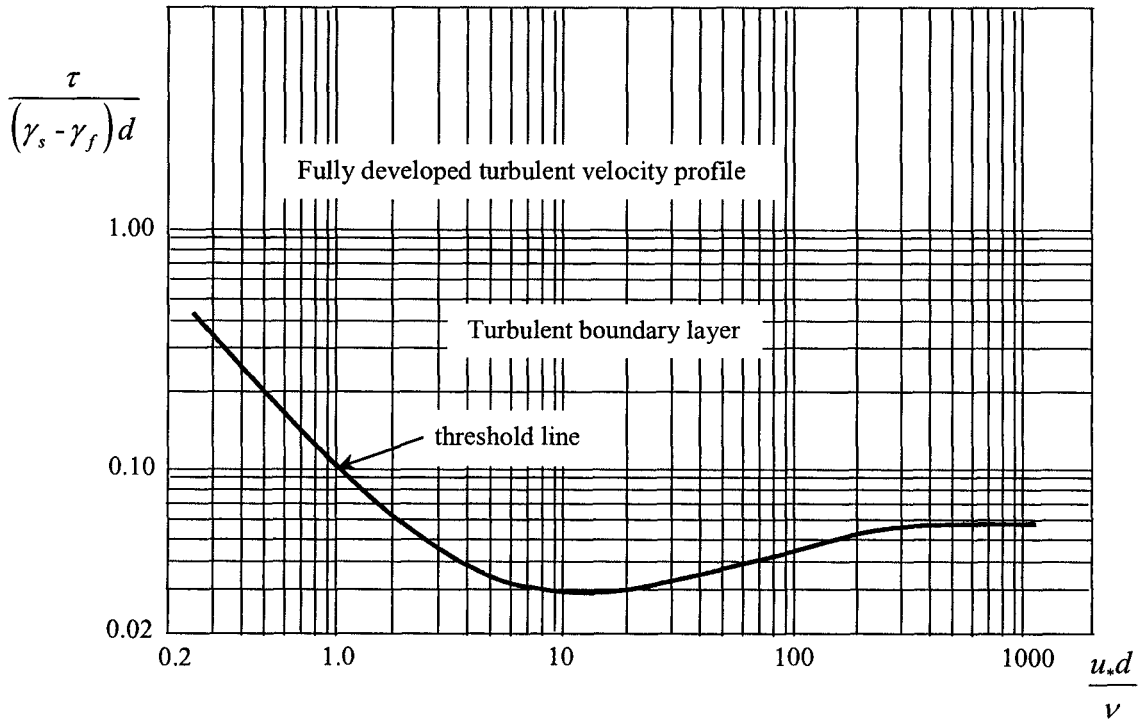

Figure 2-14: Modified Shields diagram (adapted from Yang, 1996, and Chien & Wan (1999)

Shields diagram has come under a lot of criticism by several researchers e.g. Yang (1996), Raudkivi (1998), Chien & Wan (1999) etc. In order to avoid the difficulty of determining the exact condition at which particles move, Shields (1936) measured values of $\tau / d(\gamma_s - \gamma_f)$ at least twice as large as the critical value and extrapolated to zero to obtain the values corresponding to no sediment discharge (Yang, 1999). According to Raudkivi (1998), the extrapolation introduces errors as transport rates at low values of shear stress excess, $\tau - \tau_c$, plotted on logarithmic paper do not have the same slope as those at high values of shear stress excess. A common criticism is that the axes are not independent of each other as the critical shear velocity appears on each. Trial and error is thus required to obtain a solution. According to Yang (1996), the rate of sediment transport cannot be uniquely determined by shear stress and so the use of shear stress as a criterion for incipient motion is questionable.

2.5.2.3 Probability of pickup

Figure 2-15 illustrates the influence of the type of boundary flow on particle movement (in the context of shear stress). As can be seen, the critical stress required for individual particle movements differ. When the near-bed flow is laminar, a steady shear stress is present. If this stress is larger than a particle's critical shear stress, it will move. A large shear stress will remove a greater number of particles.

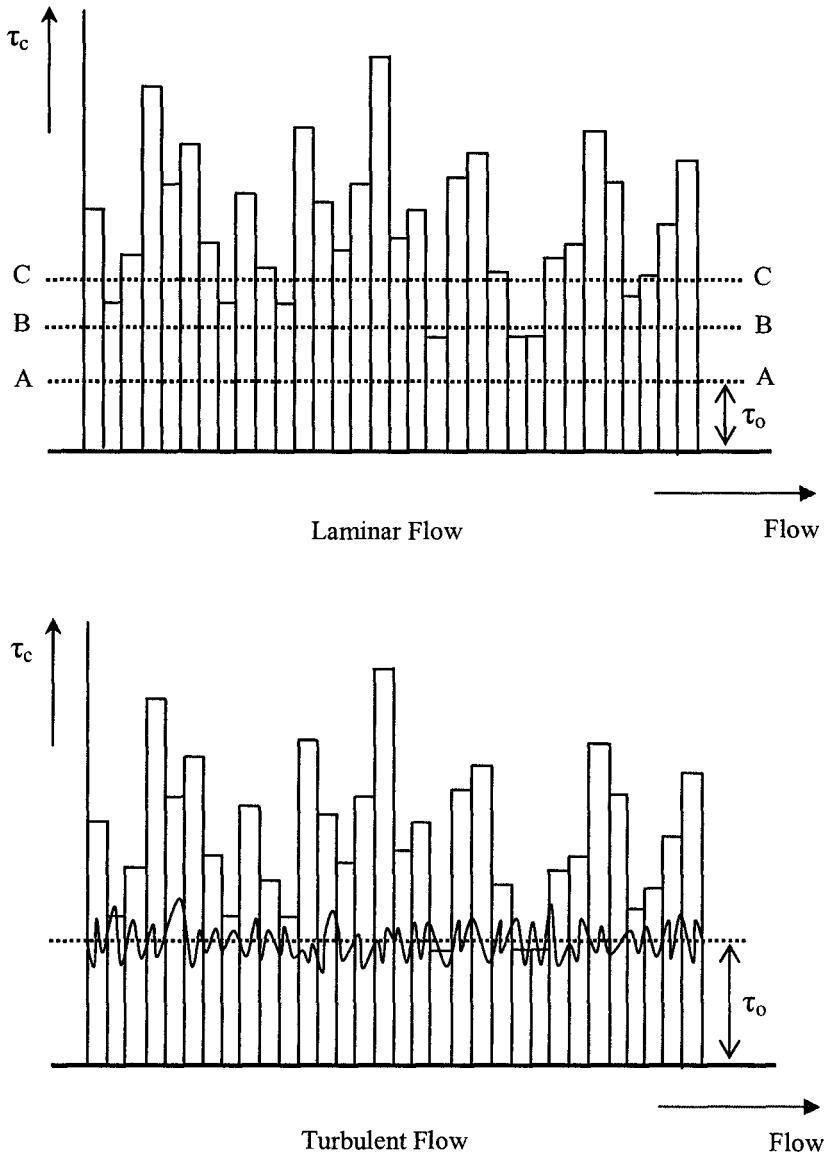

Figure 2-15: Influence of laminar and turbulent boundary flows on particle movement (Chien & Wan, 1999)

When the near-bed flow is turbulent, there are fluctuations in the applied shear stress and it is not clear which conditions will cause a particle to move. According to Chien & Wan (1999), even if a laminar sub-layer exists, strong eddies enter the layer from time to time generating fluctuations. It is clear that turbulent fluctuations and the differences in the force required for individual particle movement make it difficult to define a threshold above which there is particle movement. Many researchers have thus defined a 'pickup probability' (Armitage, 2002). This is based on the assumption of a normal distribution of the fluid forces applied to a particle. The distribution of the force required to move the particle is also considered to be normally distributed about some mean.

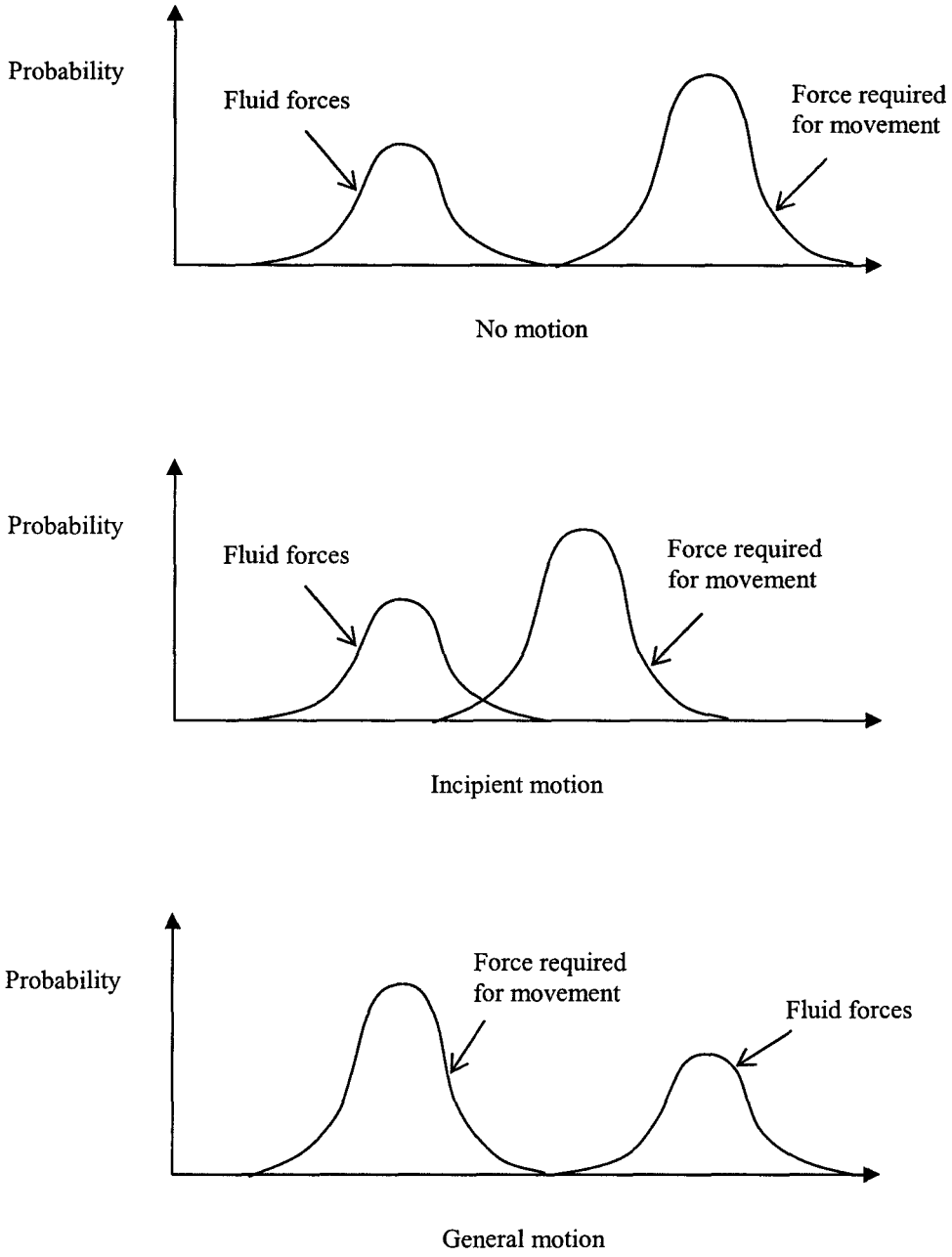

Figure 2-16: Probability of motion (adapted from Van Rijn, 1993)

Figure 2-16 shows the probability density functions of the applied fluid forces and the force required for particle movement. Movement occurs only when there is an overlap of the two curves. The scale of movement will depend on the degree of overlap. A small overlap corresponds to the likelihood of a few particle movements on the bed. When the curve for the applied fluid forces completely exceeds the force required for movement, there is general particle movement over the entire bed surface.

Several definitions have been given for the intensity of particle motion (e.g. Kramer, 1935; Shields, 1936 etc.). Shvidchenko & Pender (2000a & 2000b) define the intensity of motion as follows:

$$I = \frac{m}{N_a t} \tag{2.29}$$

where I is the intensity of motion, m is the number of particle displacements during the time interval, t, and N_a is the total number of surface particles over the sample area. In their definition, an I value of 10^{-4}s-1 is considered as weak movement whereas $I = 10^{-2}$ s-1 corresponds to general movement. These movements may be respectively described as occasional particle movement at some locations and frequent particle movement at many locations.

2.5.2.4 Stream power approach

This approach is based on the fact that a flowing fluid expends energy in moving a particle. Stream power is considered to be the rate of dissipation of fluid energy. Several investigators have applied stream power as a criterion for incipient motion. Armitage (2002) cites Bagnold (1960), Ackers & White (1973) and Yang (1972, 1973, 1976 & 1996) as examples. According to Armitage (2002), the problem with the approaches employed by these researchers is the fact that the stream power is expressed in terms of the mean velocity. The stream power is however proportional to the velocity gradient and thus varies across the channel depth. In order to be able to accurately describe incipient motion, the analysis must be carried out using local (near-bed) conditions.

Figure 2-17 shows the variation of the stream power input and the stream power dissipation for unidirectional flow through a channel.

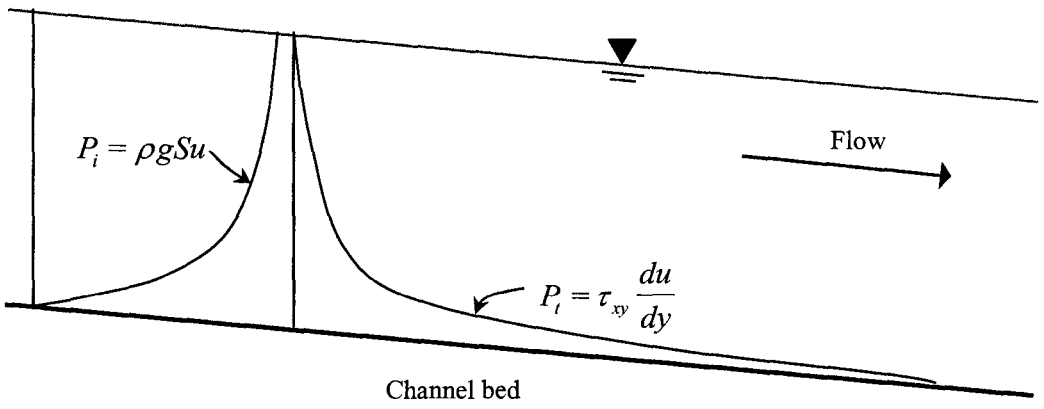

Figure 2-17: Distributions of stream power input and dissipation for open channel flow (after Rooseboom, 1992)

For unidirectional flow, the point stream power input, P_i, is given by:

$$P_i = \rho g S u \tag{2.30}$$

The stream power dissipated, P_t, at a point is given by:

$$P_t = \tau_{xy} \frac{du}{dy} \tag{2.31}$$

The distribution of stream power input is logarithmic as the point velocity profile is logarithmic (Section 2.3). As can be seen, the stream power input increases as one approaches the surface. This is in accordance with the velocity profile. The stream power dissipation, on the other hand, is greatest near the bed. This is because the shear stress and the velocity gradients are greatest near the bed (Armitage, 2002).

It has been shown by White (1991) that the energy dissipated by a moving fluid (both in flowing and transporting sediment) is as a result of shearing on the particle surfaces. The energy dissipated per unit volume, Φ, referred to by Armitage & McGahey (2003) as the applied unit stream power, is thus expressed in indicial notation as follows (White, 1991):

$$P_t = \Phi = \tau_{ij} \frac{\partial u_i}{\partial x_j} \tag{2.32}$$

The viscous stresses of an incompressible Newtonian fluid are proportional to the rates of deformation. They are therefore given by (White, 1991; Versteeg & Malalasekera, 1995):

$$\tau_{ij} = \mu \left(\frac{\partial u_i}{\partial x_j} + \frac{\partial u_j}{\partial x_i} \right) \tag{2.33}$$

Hence, if the velocity gradients are known, the applied unit stream power may be determined as follows:

$$P_t = \mu_b \left(\frac{\partial u_i}{\partial x_j} + \frac{\partial u_j}{\partial x_i} \right) \frac{\partial u_i}{\partial x_j} \tag{2.34}$$

where μ_b is the sum of both the laminar and turbulent viscosities.

Armitage (2002) analysed near-bed data from experiments carried out by several investigators and suggested the following criteria for incipient motion on a turbulent boundary:

$$P_t \geq \frac{P_r}{67}, \qquad Re_* > 6.23 \tag{2.35}$$

where P_r is the power per unit volume required to keep a particle in suspension and is given by:

$$P_r = (\rho_s - \rho) g \omega \tag{2.36}$$

2.5.2.5 The Movability Number approach

Liu (1957) noted that a requirement for ripple formation on a sediment-laden bed was that the flow had to be able to transport the sediment and, based on dimensional analysis and considerations of the scouring force of flow and sediment resistance, obtained the following criterion for sediment-ripple formation:

$$\frac{u_*}{\omega} = f\left(\frac{u_* d}{\nu}, particle\,shape\,factor\right) \tag{2.37}$$

The term u_* / ω was defined by Liu (1957) as the Movability Number (*Mn*). It has been shown by Rooseboom (1992) & Armitage (2002) that for incipient motion on a turbulent boundary, the value of *Mn* may be regarded as a constant. An expression for *Mn* on turbulent boundaries may be obtained as follows (Armitage, 2002):

Consider a rough turbulent flow. $\tau_t \approx \tau_0$ in the vicinity of the boundary. For a steady unidirectional flow in an open channel, τ_0 is given by:

$$\tau_0 = \rho u_*^2 \tag{2.38}$$

Substituting $l = \kappa y$ into Equation 2.6, Prandtl's mixing length model may also be expressed as:

$$\tau_t = \rho \kappa^2 y^2 \left|\frac{\partial u}{\partial y}\right| \frac{\partial u}{\partial y} \tag{2.39}$$

For rough turbulent flows, therefore, we have:

$$\rho u_*^2 \approx \rho \kappa^2 y^2 \left|\frac{\partial u}{\partial y}\right| \frac{\partial u}{\partial y} \tag{2.40}$$

Simplifying Equation 2.40 leads to the following expression for the velocity gradient:

$$\frac{\partial u}{\partial y} \approx \frac{u_*}{\kappa y} \tag{2.41}$$

For unidirectional flow, the applied unit stream power may be obtained from Equation 2.32 as follows:

$$P_t = \tau_{xy} \frac{\partial u}{\partial y} \tag{2.42}$$

Since $\tau_{xy} = \tau_t \approx \tau_0$, substituting Equations 2.38 and 2.41 into Equation 2.42 yields:

$$P_t \approx \frac{\rho u_*^3}{\kappa y} \tag{2.43}$$

The power per unit volume required to keep a particle in motion is given by Armitage & McGahey (2003) as follows:

$$P_r = (\rho_s - \rho) g \omega \tag{2.36}$$

This is obtained from the fact that the power required to keep a particle in suspension is similar to the power dissipated if the particle falls through the fluid at terminal velocity. Particles moving along the bed are also considered to be in suspension but very close to the bed. The settling velocity of a sediment particle has been presented in Section 2.4.3 as:

$$\omega = \sqrt{\frac{4}{3} \frac{(\rho_s - \rho)}{\rho} \frac{gd}{C_d}} \tag{2.17}$$

According to Chien & Wan (1999), a typical value of C_d for turbulent boundaries is 1.1. Substituting this value into Equation 2.17 and squaring both sides gives:

$$\omega^2 = \frac{4}{3.3} \frac{(\rho_s - \rho)}{\rho} gd \tag{2.44}$$

According to Armitage & McGahey (2003), the power required to lift a particle from the bed should be greater than or equal to the power required to keep it in suspension. If the applied stream power required to dislodge a particle is considered to be directly proportional to the

power required to keep the particle in motion, then Equations 2.36 and 2.43 (Armitage & McGahey, 2003) give:

$$\frac{\rho u_*^3}{\kappa y} \propto (\rho_s - \rho) g \omega \tag{2.45}$$

Dividing both sides by ω^3 and applying Equation 2.44 yields:

$$\frac{u_*^3}{\omega^3} \propto \frac{3.3\kappa y}{4d} \tag{2.46}$$

As seen from Equation 2.46, the Movability Number varies with depth. If the critical value of the Movability Number required for incipient motion is determined at the distance $y = d$ then Equation 2.46 becomes:

$$\frac{u_*}{\omega} \propto \left(\frac{3.3\kappa}{4}\right)^{\frac{1}{3}} \tag{2.47}$$

This implies that for turbulent boundaries, the Movability Number required for incipient motion is a constant. This constant was estimated by Armitage (2002) to be 0.17 after analysing data from several investigators i.e.

$$Mn_c = \left.\frac{u_*}{\omega}\right|_{critical} = 0.17, \qquad \frac{u_* d}{\nu} > 6.23 \tag{2.48}$$

During the study, Armitage (2002) also estimated the relationship between the intensity of motion and the Movability Number to be:

$$Mn = 0.0066 \ln(I) + 0.2405 \tag{2.49}$$

2.5.3 Incipient motion on sloping beds

The discussion on incipient motion has thus far concentrated on particle motion on a flat bed. It is to be expected that if the bed slopes downward in the direction of flow, a component of the particle's weight adds to the force that attempts to dislodge the particle. The result is that the particle is dislodged easier by a particular flow condition than it would have had it been on a flat bed. In terms of incipient motion criteria, the critical value would have to be multiplied by a certain factor, which is dependent on the slope, to reflect the relative ease in moving the particle (i.e. a smaller critical value is required for incipient motion). Similarly, if the slope is upwards it

becomes more difficult to dislodge a particle and a higher critical value is required for incipient motion. Two types of slope have been defined by Armitage & McGahey (2003) as follows:

Longitudinal or Streamwise slope – this is the fall or rise of the bed in the direction of flow. A fall in the direction of flow is regarded as a positive slope and a rise as negative.

Transverse slope – this is the fall of the bed in either direction normal to the direction of flow.

Van Rijn (1993) derived incipient motion criteria for both longitudinal and transverse slopes in terms of the drag force. If F_{Dcr} is the critical drag force for a given longitudinal slope β, F_{Dcr0} is the critical drag force for a horizontal bed and ϕ_r is the angle of repose, then for a longitudinal slope:

$$\frac{F_{Dcr}}{F_{Dcr0}} = \cos\beta\left(1-\frac{\tan\beta}{\tan\phi_r}\right) \tag{2.50}$$

Similarly, if F_{Dcr} is the critical drag force for a given transverse slope γ then:

$$\frac{F_{Dcr}}{F_{Dcr0}} = \cos\gamma\sqrt{\left(1-\frac{\tan^2\gamma}{\tan^2\phi_r}\right)} \tag{2.51}$$

Based on Equations 2.50 & 2.51, Armitage & McGahey (2003) present the following 'slope correction' factor for incipient motion criteria:

$$\psi = \sqrt{\cos\beta\left(1-\frac{\tan\beta}{\tan\phi_r}\right)\cos\gamma\left(1-\frac{\tan^2\gamma}{\tan^2\phi_r}\right)}^{1/2} \tag{2.52}$$

The slope correction factor may be applied to the Movability Number criterion for incipient motion as follows (Armitage & McGahey, 2003):

$$\left.\frac{u}{\omega}\right|_{cr\beta,\gamma} = \psi\left.\frac{u}{\omega}\right|_{cr0} \tag{2.53}$$

Equation 2.49 was adjusted for the slope and relative roughness. The final equation for the intensity of motion was thus:

$$\frac{u_*}{\omega} = \psi\left[0.0066\ln I - 0.204\frac{d}{h} + 0.2405\right] \tag{2.54}$$

2.6 Types of scour

Classification of the types of scour varies with literature. Raudkivi (1998), Breusers & Raudkivi (1991) and Melville & Coleman (2000) classify scour into 3 main categories, namely General, Constriction and Local scour. Hoffmans & Verhiej (1997) add Constriction scour to General scour and so have 2 main categories; General and Local scour. Richardson & Davis (2001) break the total scour at a highway crossing into Long Term Aggradation & Degradation, General and Local scour. May *et al.* (2002) classify scour into Natural, Constriction and Local scour and Graf (1998) also considers constriction scour under Local scour.

It is therefore necessary to state clearly which classification is used in order to avoid any ambiguities in meaning. The classification used by Breusers & Raudkivi (1991), Raudkivi (1998) and Melville & Coleman (2000) will be used herein. Scour will be classified into General, Constriction and Local scour. Also, depending on the conditions under which scour develops, it may be considered to be either Clear-Water scour or Live-Bed scour (Breusers & Raudkivi, 1991; Hoffmans & Verhiej, 1997; Graf, 1998; Raudkivi, 1998; Melville & Coleman, 2000; Richardson & Davis, 2001; May *et al.*, 2002).

2.6.1 General scour

The various types of scour which are considered by Breusers & Raudkivi (1991), Raudkivi (1998) and Melville & Coleman (2000) as general may be categorized into the following:

a. Degradation, aggradation and regime conditions
b. Lateral channel migration
c. Bend scour
d. Confluence scour

These types of scour are related to the river in general and depend mainly on the characteristics of the river and the catchment. They are not directly influenced by hydraulic structures and occur whether or not they are present.

2.6.1.1 Degradation, aggradation and regime conditions

Degradation and aggradation take place along the longitudinal direction of a river. They occur over a long period of time and result in changes in bed elevations along the longitudinal profile. They come about as a result of varying flow conditions and sediment supply (Richardson & Davis, 2001; May *et al.*, 2002). When the rate at which scouring occurs exceeds the rate of deposition (long term basis), degradation is said to take place i.e. there is a deficit in sediment supply from upstream and this results in the lowering of the channel bed. On the other hand, if the deposition exceeds scouring, there will be a rise in the elevation of the channel bed and aggradation is said to take place.

Regime conditions refer to the dynamic equilibrium conditions (flow and slope) to which a river has adjusted itself (May *et al.*, 2002). Under such conditions, scouring and deposition occur at the same pace and hence aggradation or degradation does not take place. If the equilibrium conditions are disturbed by changes in water or sediment flows, net scouring or deposition is

likely to occur. Changes in flows may be due to human interference or natural changes such as urbanization, creation or removal of hydraulic structures, braiding of river channels, etc.

2.6.1.2 Lateral channel migration

This may be in the form of shifting bank lines, meander progression, movement of deep-water channels within channel banks or continuously changing channel positions in braided channels (Melville & Coleman, 2000; May *et al.*, 2002). The channel migration may be gradual or rapid. Rapid migration usually occurs in response to flood events. A river is said to meander when it deviates from its straight course into a winding path. The meander progresses when, in the bends, there is continual scouring at the outer banks and deposition on the inner banks. This results in the movement of the entire channel.

2.6.1.3 Bend scour

This is scour that occurs in river bends as a result of the centrifugal force that acts on the water. According to Raudkivi (1998), this centrifugal force drives the water radially outward and results in the water surface possessing a super elevation. The super elevation of the water surface creates a lateral pressure gradient between the outer bank and the inner bank. Also, the magnitude of the centrifugal force decreases with depth due to decreasing velocity and results in a downward pressure gradient, which drives the water downward at the outer bank. The lateral pressure in turn drives the water inward toward the inner bank producing a kind of circulation in the cross-section. Flow goes outward at the top, downward at the outer bank, inward at the bed and upward at the inner bank. This circulation, together with the channel flow, produces a helical flow as the water moves along the bend. The helical flow decays a distance after the bend.

2.6.1.4 Confluence scour

A confluence is the place where two or more channels meet. Here, flows from the channels meet at different angles and their water levels, flow rates and slopes may also differ (Hoffmans & Verhiejj, 1997; Armitage & McGahey, 2003). When the streams of flow converge, secondary currents are induced i.e. lateral flows are produced resulting in helical flow patterns similar to the flow patterns obtained when two river bends are placed back to back. These helical flows usually result in the formation of deep scour holes with steep sides in the region of the confluence (Melville & Coleman, 2000).

2.6.2 Constriction scour

This type of scour occurs in cross-sections of a river where the width is reduced. The contraction in width may be natural or as a result of the construction of a hydraulic structure such as a bridge (Melville & Coleman, 2000). Contraction of a channel leads to increased velocity of flow and shear stresses within the restricted section (May *et al.*, 2002). The consequence of these increases being the scouring of most or all of the bed at the section.

2.6.3 Local scour

An obstruction placed in a flowing river changes the pattern of flow of the river in its neighbouring regions. Flow directions and pressure gradients are altered and often results in complex flow patterns. According to May *et al.* (2002), flow velocities and turbulence within the locality of the obstruction are increased. Depending on the nature of the obstruction, vortices may also develop. These increase the scouring potential of the stream in the locality of the obstruction. The result is the lowering of the bed in the immediate surroundings of the obstruction relative to the channel bed. This type of scour is referred to as local scour. Obstructions may be in the form of bridge piers, abutments, spur dikes, etc. Only flows around bridge piers are discussed here as they are the focus of the research. Figure 2.18 illustrates the complex flow features that develop around a bridge pier. The flow field has been described by several investigators. Armitage (2002) provides the following summary of the flow patterns:

There is a rise in height of water at the leading face of the pier. This rise corresponds to the velocity head of the oncoming flow which is maximum at the surface. The flow is forced up and back onto itself to form a bow wave or "roller".

There is a rise in pressure on the leading face of the pier (termed the "stagnation pressure") and this increase decreases with the square of the velocity of the oncoming flow i.e. it decreases from top to bottom. This results in a partial reversal of the normal pressure gradient that provides the driving mechanism for a vertical "downflow". The maximum velocity of the downflow in vertical section, according to experimental data by Ettema (1980) and Raudkivi (1986), is situated between 0.05 and 0.02 times the pier breath, b_p, upstream of the pier, being closer to the pier near the bed than at the surface. The velocity of the downflow also increases in magnitude towards the bed in the vertical section. If no scour is present, the maximum velocity is approximately 40% of the average oncoming velocity, U. This velocity increases to approximately 0.8U as the scour depth increases past $2b_p$ (Breusers & Raudkivi, 1991; Raudkivi, 1998). This relatively high velocity flow directed at the base of the pier acts as a sort of water jet that helps to initiate and maintain the scouring process (Graf, 1998). The increase pressure on the leading face of the pier also helps to provide the necessary force for the acceleration of the flow around the sides.

Once a scour hole begins to form, flow separation at the upstream rim results in the formation of a lee eddy that rotates in the opposite direction to the bow roller. This lee eddy is called the "horseshoe vortex" owing to its distinctive shape: it wraps itself around the front half of the pier and extends a few pier diameters downstream on either side before losing its identity and becoming part of the general turbulence. According to Raudkivi (1998), the vorticity of the horseshoe vortex is quite small and its main role in the scouring process comes about through its interaction with other flow structures. For example, it pushes the maximum downflow velocity within the scour hole closer to the pier.

Flow separation around the sides of the pier results in the formation of "wake vortices" that alternately separate from the two sides to form a Von Karman vortex street. Near the bed, these vortices interact with the horseshoe vortex and, with their vertical low-pressure centres, lift the sediment from the bed like miniature tornadoes (Raudkivi, 1998).

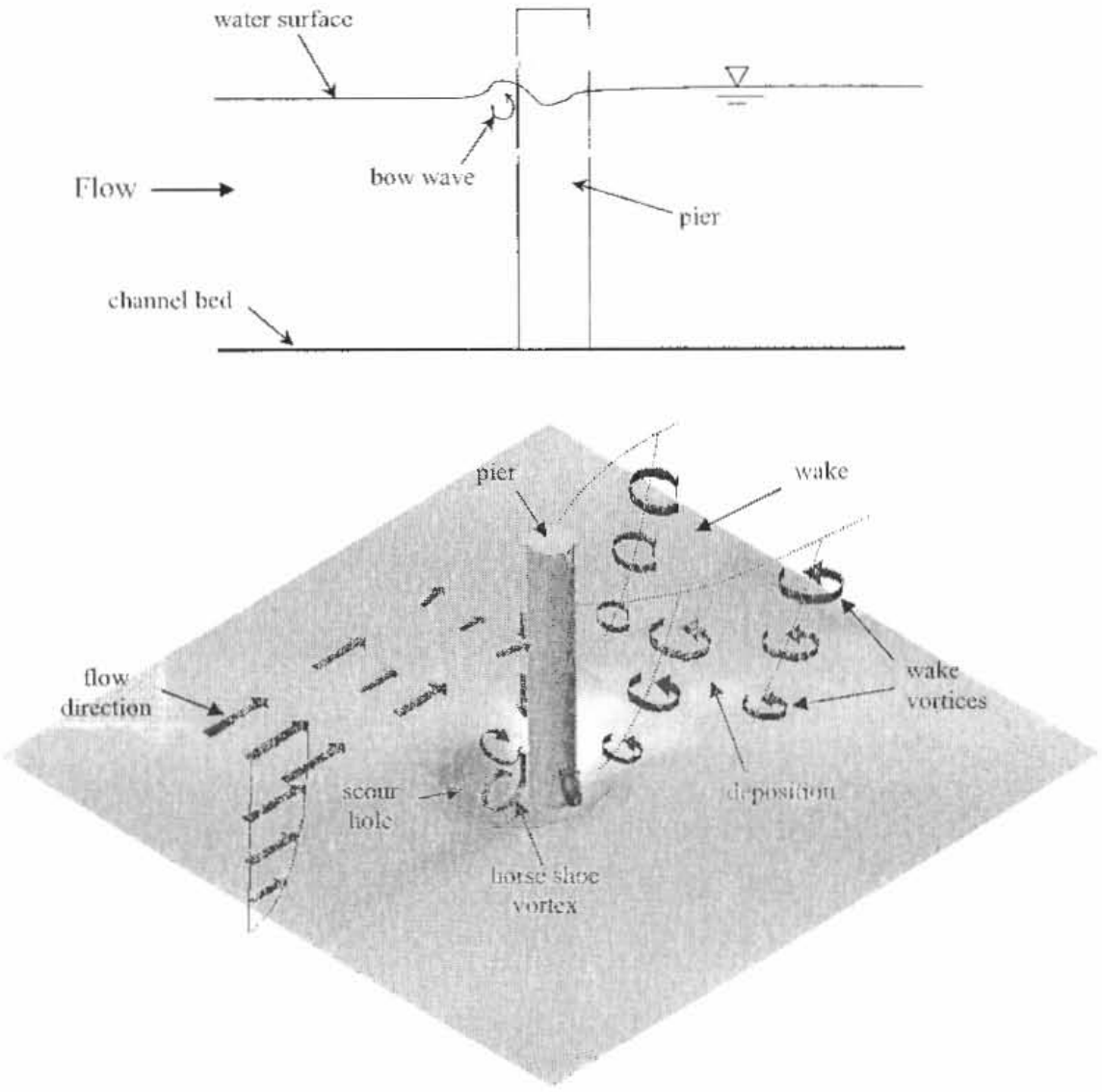

Figure 2-18: Flow pattern around a bridge pier (after Raudkivi, 1998, and Melville & Coleman, 2000)

2.6.3.1 Bed Features

Local and constriction scour are usually referred to as localized scour (Melville & Coleman, 2000). Depending on the conditions under which localized scour takes place, it may be considered to be either clear-water scour or live-bed scour. In order to understand live-bed scour, it is necessary to first understand bed features and how they come about.

Bed features are relief features initiated by the fluid oscillations generated downstream of small local obstacles over a bottom consisting of movable sediment materials (Van Rijn, 1993). There are generally four different criteria used in literature for classifying bed features. They are classified using either a particle-related Reynolds number (Liu, 1957), the Froude number (Engelund & Hansen, 1967), the stream power (Simons & Richardson, 1966) or the bed shear stress (Van Rijn, 1984).

According to the bed shear stress criterion, as presented by Yang (1996) and Raudkivi (1998) criterion, bed features come about in an alluvial channel when the bed shear stress is greater than the critical shear stress and there is general movement of the bed material. Initially, as the shear stress increases, ripples form. These grow in size and eventually form what are known as dunes. The flow is sub critical at this stage and the dune profiles are out of phase with the water surface profile. Further increase in the shear stress results in the washing out of the dunes until the bed is eventually basically flat with the bed material moving in sheets. The bed is then said to be in transition. Subsequent interaction of the bed with the water surface waves may lead to the formation of anti-dunes. Here, the flow is super critical and the bed profile is in phase with the water surface profile. Further increase in the flow velocity results in the formation of chutes and pools. Here, both sub and super critical flow exist. Super critical flow develops over the lee side forming a chute. The flow breaks into sub critical via a hydraulic jump near the crest forming a pool. Figure 2-19 shows various types of bed features (after Simons & Richardson, 1966).

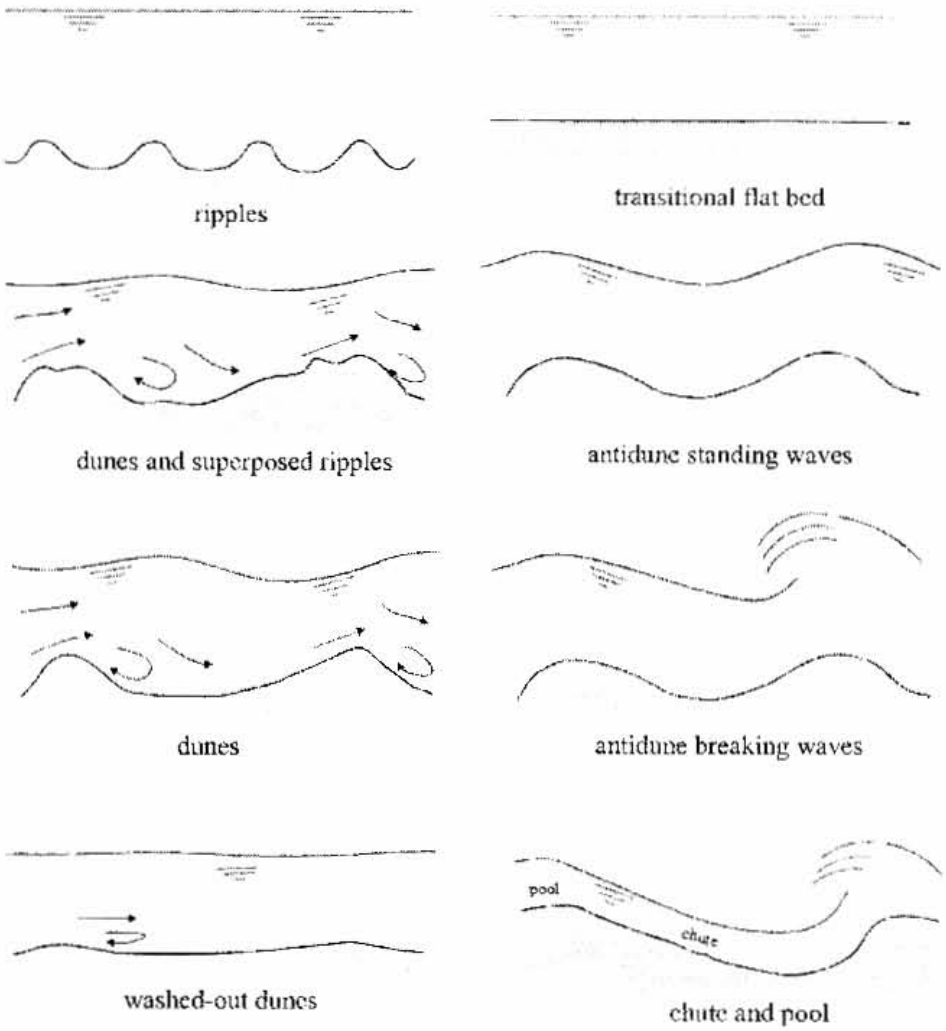

Figure 2.19: Various types of bed features (after Simons & Richardson, 1966)

The different bed features migrate either upstream or down stream. The migration of dunes and anti-dunes are shown in Figure 2-20. As can be seen, dunes migrate downstream whereas anti-dunes migrate upstream. In dunes, erosion occurs on the luff side (side facing direction of flow) as the flow accelerates and deposition subsequently occurs on the lee side where there is recirculation resulting in the movement of the dune in the direction of flow. In anti-dunes, erosion occurs on the lee side and there is subsequent deposition on the luff side resulting in movement upstream (Van Rijn, 1993).

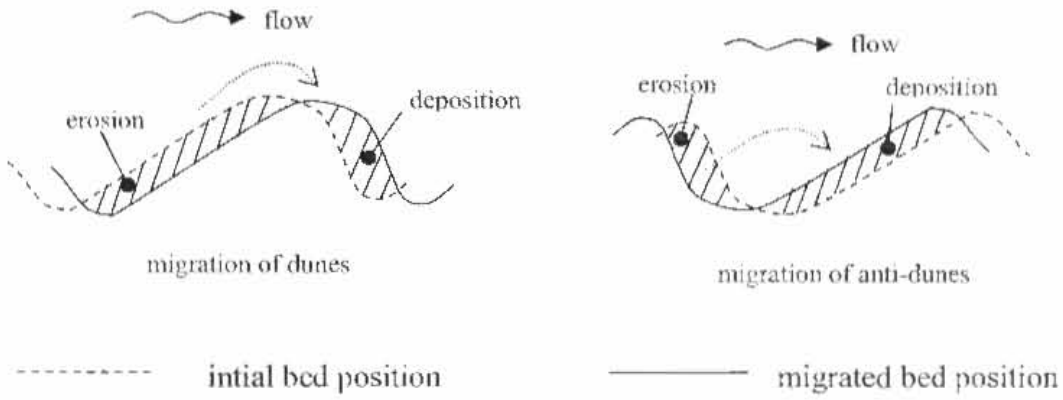

Figure 2-20: Migration of dunes and anti-dunes (after Van Rijn, 1993)

2.6.3.2 Clear-water and live-bed scour

When localized scour occurs in the absence of sediment supply from upstream, it is termed as clear-water scour. According to Hoffmans & Verhiejj (1997), the lack of sediment supply is either as a result of a non-erodible bed upstream or the bed material upstream being at rest. Raudkivi (1998) explains that when the upstream bed material is at rest, the upstream bed shear stresses are at or below the critical or threshold shear stress for initiation of bed material movement. May *et al.* (2002) also point out that in clear-water scour, the water may not be literally clear but may contain fine sediments which remain wholly in suspension such that they do not affect scouring at the bed.

If there is a supply of sediment from upstream, the localized scour is referred to as live-bed scour. In this case, the threshold shear stress for initiation of bed material movement upstream is exceeded and there is general movement of particles downstream. For live-bed scour, both scouring and deposition take place. Live-bed scour is sometimes referred to as sediment-transport scour (Graf, 1998).

May *et al.* (2002) explain the scouring process from clear-water conditions to live-bed conditions (increasing velocity). Initially, when there are relatively low flow velocities, clear-water scour exists. As the flow velocities increase so does the clear-water scour. It eventually gets to the point where threshold conditions are met and general bed material movement is about to occur. Here, scour depth is maximum and is known as the threshold peak (Melville & Chiew, 1999). When threshold conditions are exceeded, live-bed conditions exist i.e. there is general movement

of bed material and deposition occurs in the scour hole inhibiting its growth. Figure 2-21 shows the variation of scour depth with velocity as described by Chabert & Engeldinger (1956). The dashed lines indicate a second peak forecast by Raudkivi (1982). The second peak, known as the live-bed peak, occurs at about the transition flat bed stage of sediment transport on the channel bed (Melville & Chiew, 1999). At this stage, the net scour is greater than the net deposition.

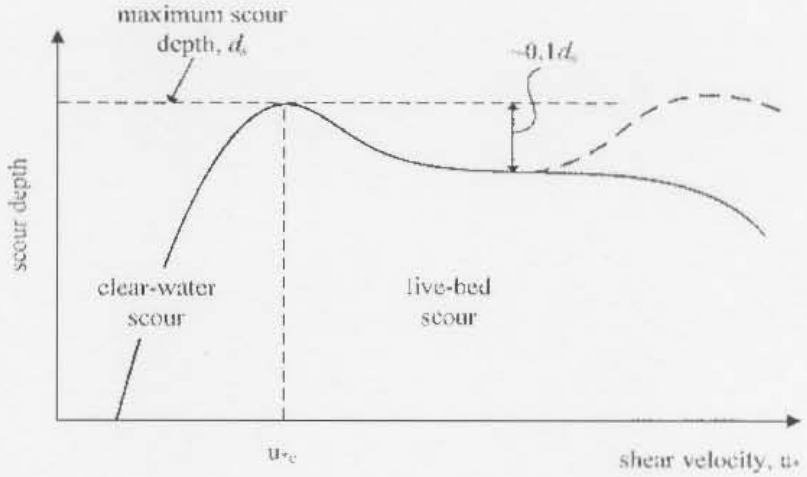

Figure 2-21: Variation of scour depth with velocity (after Chabert & Engeldinger, 1956)

The temporal evolution of clear-water and live-bed scour is shown in various literature on scour (e.g. Breusers & Raudkivi, 1991; Hoffmans & Verhiejj, 1997; Graf, 1998; Raudkivi, 1998; Melville & Coleman, 2000; Richardson & Davis, 2001; May *et al.*, 2002). Figure 2-22 (also after Chabert & Engeldinger, 1956) shows the variation of scour depth with time for both types of localized scour.

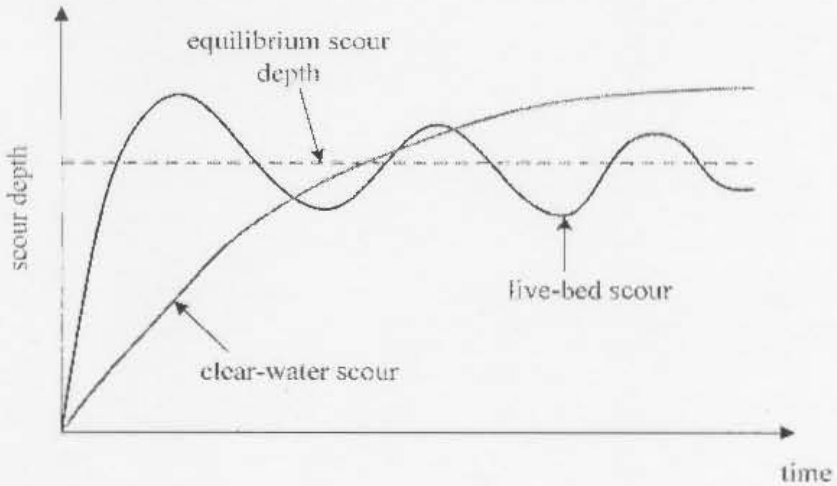

Figure 2-22: Variation of scour depth with time (after Chabert & Engeldinger, 1956)

Under clear-water scour conditions, the scour depth approaches equilibrium asymptotically over a period of days. Under live-bed scour, however, the scour depth increases rapidly and then fluctuates about an average value. The fluctuation in scour depth is attributed to the passage of

bed features (Hoffmans & Verhiejj, 1998; Raudkivi, 1998; Melville & Coleman, 2000; May *et al.*, 2002). May *et al.* (2002) infer from Richardson & Davis (2001) that the maximum clear-water scour and the maximum live-bed scour are about the same.

2.6.4 Temporal evolution of the scour hole

2.6.4.1 Controlling mechanism of scour

Dargahi (1990) studied the controlling mechanism and used Figure 2-23 to explain the general pattern of scour.

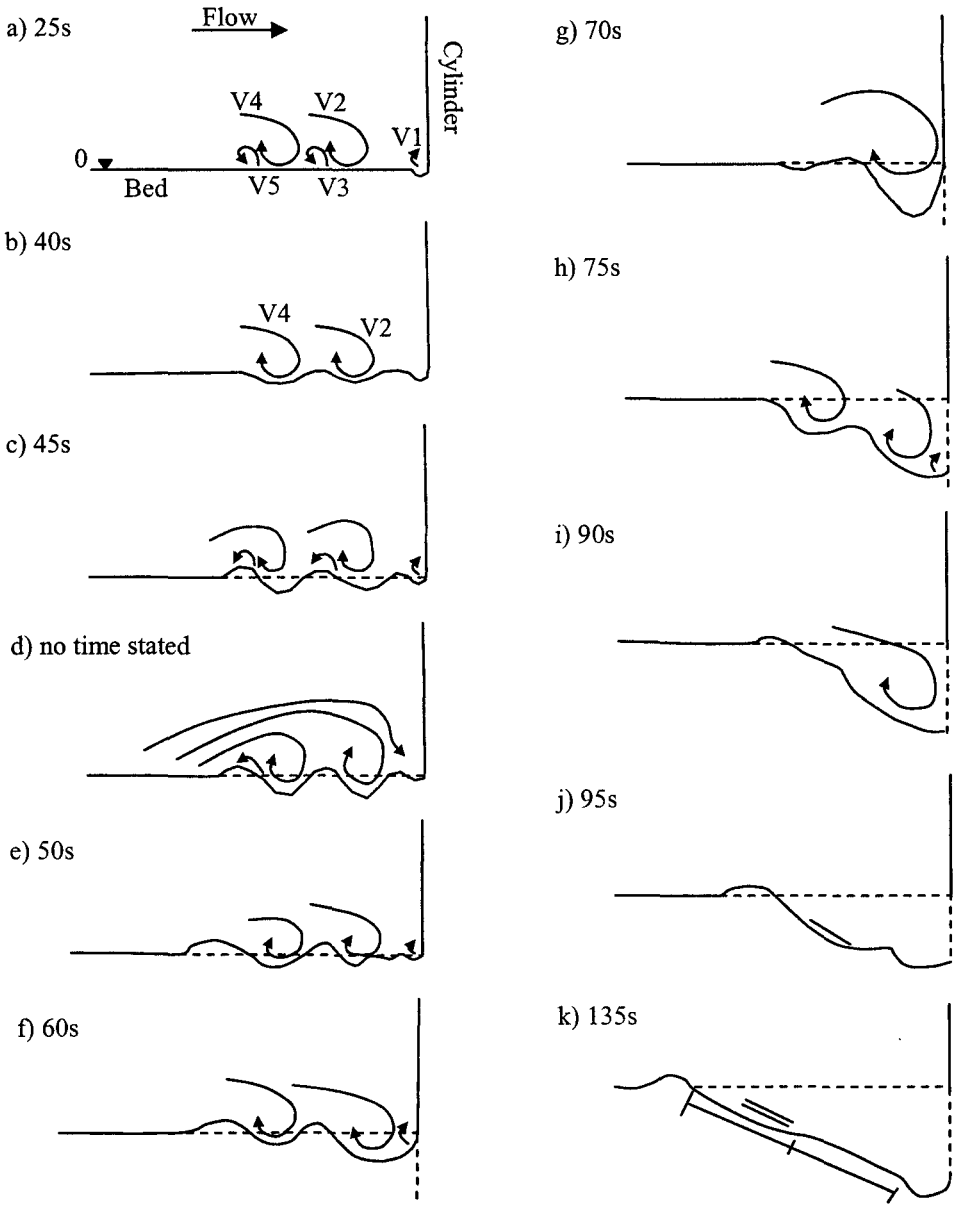

Figure 2-23: General scour patterns upstream of cylinder (after Darghi, 1990)

The studies indicated that the system of horse shoe vortices was dependent on the pier Reynolds number, Re_d. According to Dargahi (1990), scour on the upstream side began under V1 and at

either sides of the cylinder at $\pm 45°$. Scouring due to V2, V3, V4, and V5 then occurred simultaneously about 2s later, giving rise to two small depressions. The depressions extended rapidly towards the face of the cylinder. Sediment picked up by V2 and V4 were fed into V3 and V5 which deposited them to form two sediment humps. V1 continued its scouring action whilst V2-V5 moved back and forth changing the positions of the two depressions. Sediment trapped in the vortices were transported downstream. As the scour depressions at the sides of the cylinder deepened, the side slope steepened and the sediment became unstable causing an increase in the rate of sediment transport. Eventually, the depressions by V1 and V2 merged to take the shape of a concave curve. Two slopes were formed as a result of V2 and V4. After a while, the slopes became roughly of the same length. At this stage, the maximum scour was at $0.2b_p$ and still at an angle of $\pm 45°$. From here on, changes in the scour profile was periodic with sediment bursts taking place at irregular intervals. The main scouring agents appeared to be V2 and V4 and the downflow. Both V4 and V5 had reduced in strength in comparison with the initial stages. As the scour hole progressed with time, the size of the vortices increased in diameter and the rate of scouring decreased. When the scouring rate had decreased significantly, it was noted that the slope of the lower scour profile was larger (30°) than that of the upper profile (20°).

2.6.4.2 Phases of scour hole development

Figure 2-24 was presented by Hoffman & Verhiejj (1997) to describe the evolution of the maximum scour depth with time. The gradient at any point represents the rate of increase of the maximum scour depth, d_s, with time, t. The figure also shows the four phases in scour hole development that were distinguished by Zanke (1978) based on clear-water scour experiments (Hoffmans & Verhiejj, 1997; May *et al.*, 2002). These are the initial, development, stabilization and equilibrium phases respectively.

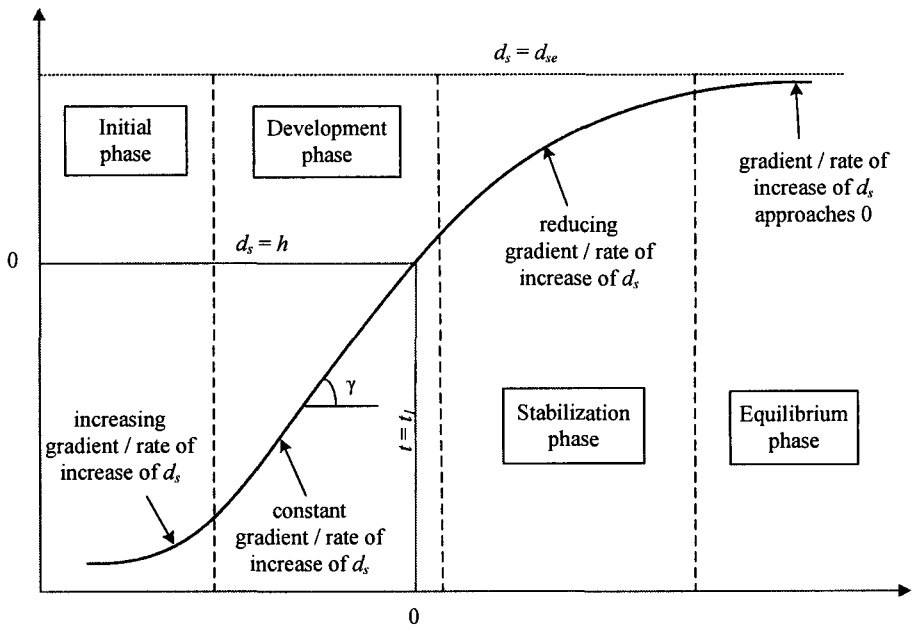

Figure 2-24: Evolution of scour hole (after Hoffmans & Verhiejj, 1997)

In Figure 2-24, h is the depth of flow, d_{se} is the equilibrium scour depth and t_1 is the time at which the depth of the scour hole is equal to the depth of flow.

In the initial phase, the erosion capacity is most severe. Particles near the upstream slope of the scour hole that is just developing are transported as either suspended or bed load i.e. either in suspension or along the bed. The rate of increase of scour depth with time increases significantly. This can be seen in Figure 2-24 where in the initial phase, the gradient of the line, which indicates the rate of change of scour depth with time, increases as time progresses.

In the development phase, the scour hole progresses significantly. The ratio between the maximum scour depth and its distance from the upstream point where the scour hole starts remains constant. It can be noted from Figure 2-24 that the gradient of the line is fairly constant throughout the development phase indicating that the rate of increase of the scour depth with time remains constant. The shape of the hole does not change and equilibrium conditions exist at the upstream slope.

During the stabilization phase, the rate of increase of the maximum scour depth reduces. This is seen in Figure 2-24 where the gradient of the line begins to reduce. Scouring at the downstream slope near the general bed level occurs at a faster rate than at the bottom of the hole. Hence, the scour hole progresses more in the longitudinal direction than the vertical direction.

In the equilibrium phase, the dimensions of the scour hole do not change significantly. Equilibrium conditions exist throughout the hole (Hoffmans & Verhiejj, 1997; May *et al.*, 2002). Again, this is shown in Figure 2-24 which indicates that the rate of increase in scour depth with time in the equilibrium phase approaches zero.

2.6.4.3 Scour hole evolution

Melville & Chiew (1999) studied the evolution of scour holes in four different flumes. The research was performed under clear water conditions and with uniform sands. The experimental data obtained from the experiments were supplemented with Ettema's (1980) and Graf's (1995) data to obtain a data set consisting of results from about 84 experiments. The following relationship for the temporal evolution of local scour around circular piers was fitted to the data set:

$$\frac{d_s}{d_{se}} = \exp\left[-0.03\left|\frac{U_c}{U}\ln\left(\frac{t}{t_e}\right)\right|^{1.6}\right] \tag{2.55}$$

where d_s is the maximum scour depth at time t, d_{se} is the maximum scour depth at equilibrium, t_e is the time taken to achieve equilibrium, U is the mean approach velocity, and U_c is the critical velocity. A couple of other formulas have been presented for scour hole evolution e.g. Hoffman & Verheijj (1997) and Oliveto & Hager (2002). Equation 2.55 is presented here because of its simplicity. Figure 2-25 shows the variation of the dimensionless scour depth and the dimensionless time for different values of the dimensionless velocity.

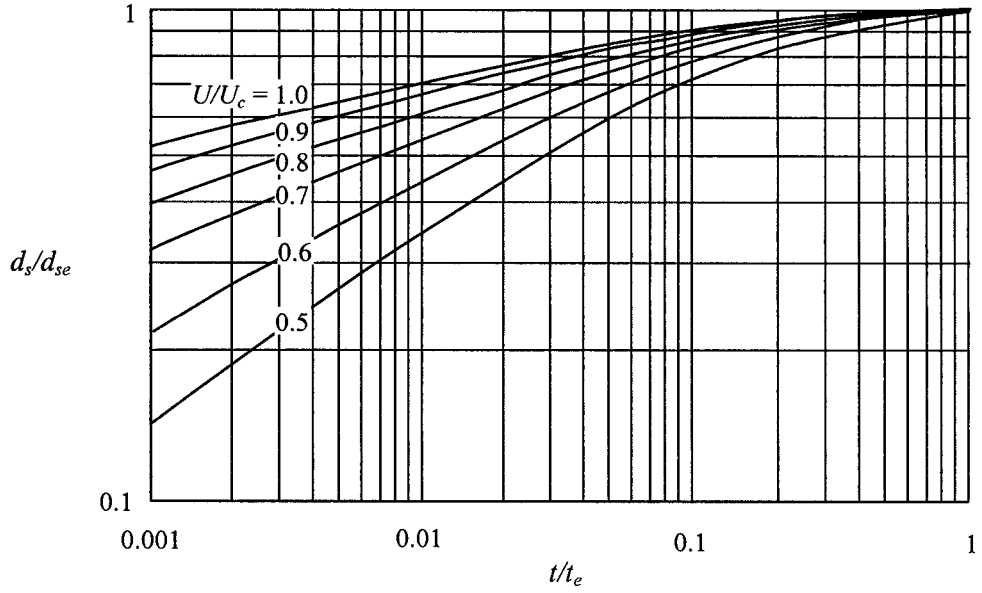

Figure 2-25: Temporal evolution of scour depth for different flow intensities (after Melville & Chiew, 1999)

Ahmed (1995) studied flow past cylindrical piers on mobile beds in a flume at the University of Alberta and fitted the following equation to data from some of the different experiments that were run:

$$\frac{d_s}{d_{se}} = 1 - \exp\left[(\ln 0.05) \times \left(\frac{t}{t_e} \right)^{0.65} \right] \tag{2.56}$$

This relationship does not account for the influence of flow intensity. It is illustrated in Figure 2-26.

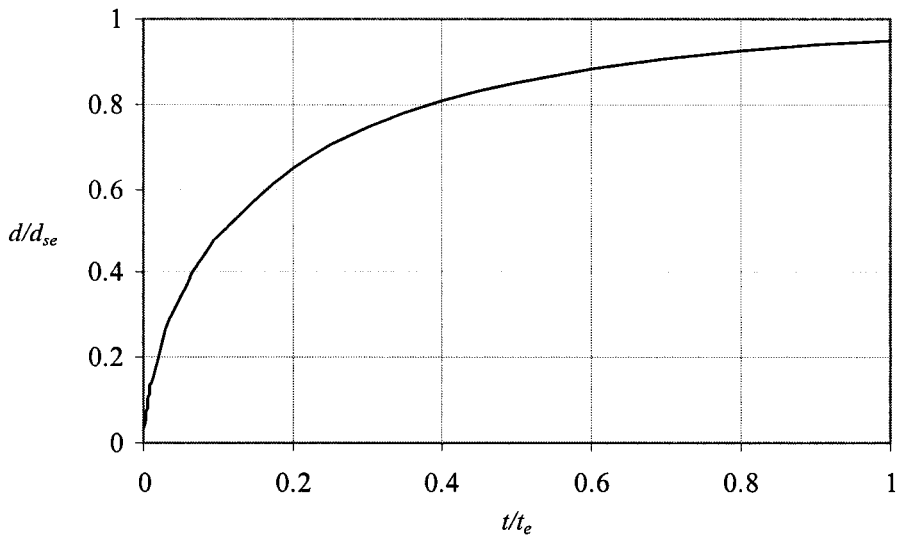

Figure 2-26: Temporal evolution of scour depth (after Ahmed, 1995)

2.7 Summary

This section has looked at the physical aspects of local scour around bridge piers. The boundary layer theory was introduced and the flow distributions about circular piers were described. The different approaches to incipient motion were mentioned and the movability number approach was explained. The section was concluded with a description of the development and evolution of the local scour hole. The estimation of local scour is important in the design of bridge piers. Empirical relationships that have so far been developed for this purpose are based on simplifying assumptions that place a limit on their use. Computational models offer an alternative solution to the estimation of local scour. They are not subject to the same limitations as empirical relationships but may be restricted in their use due to limited computational capacity. Nevertheless, they appear to offer a better solution to the problem of scour estimation. The key to the correct prediction of local scour is the accurate determination of the flow field within the vicinity of the pier. The next chapter thus deals with the solution of fluid flow problems using computers. It also summarizes previous computational modelling attempts that been made at predicting local scour.

Chapter 3
Computational fluid dynamics in the modelling of local scour

Many phenomena in fluid dynamics can be accurately or well-described using ordinary or partial differential equations. Most equations describing fluid motion and behaviour and key ideas on how they could be solved using numerical methods were established more than a century ago. However, these ideas were of little use before the advent of computers. In the past, fluid dynamics problems were solved using only theoretical (analytical) and experimental approaches. Analytical solutions were only possible for very simple equations. Advances in computing technology have subsequently made it possible to employ numerical methods to solve most fluid dynamics problems. According to Ferziger & Perić (1999), the first electronic computers built in the 1950s performed only a few hundred operations per second. The performance of computers has increased dramatically since then. The Japanese research institution, RIKEN, announced the completion of their supercomputer, MDGRAPE-3, in June 2006. MDGRAPE-3 is a special purpose computer for simulating molecular dynamics and can perform up to one petaFLOPS (10^{15} floating point operations per second). Current high end PCs typically perform between 12-15 gigaFLOPS (10^{9} floating point operations per second). According to Wikipidea (2006a), a relatively cheap but modern desktop computer (e.g. a Pentium 4 or Athlon 64 CPU) running at a clock frequency in excess of 2 GHz generally provides computational performance in the range of a few gigaFLOPS. These figures are likely to increase dramatically over the next few years. The new gaming system by Sony, called the PS3, runs on a 3.2 GHz cell processor manufactured jointly by Sony, Toshiba and IBM, and can perform 204 gigaFLOPS. The cost of computers has also gone down drastically over the past few years. Figure 3-1 illustrates the drop in the relative cost of computing (cost required per operation) from the early 1950s up to 2006.

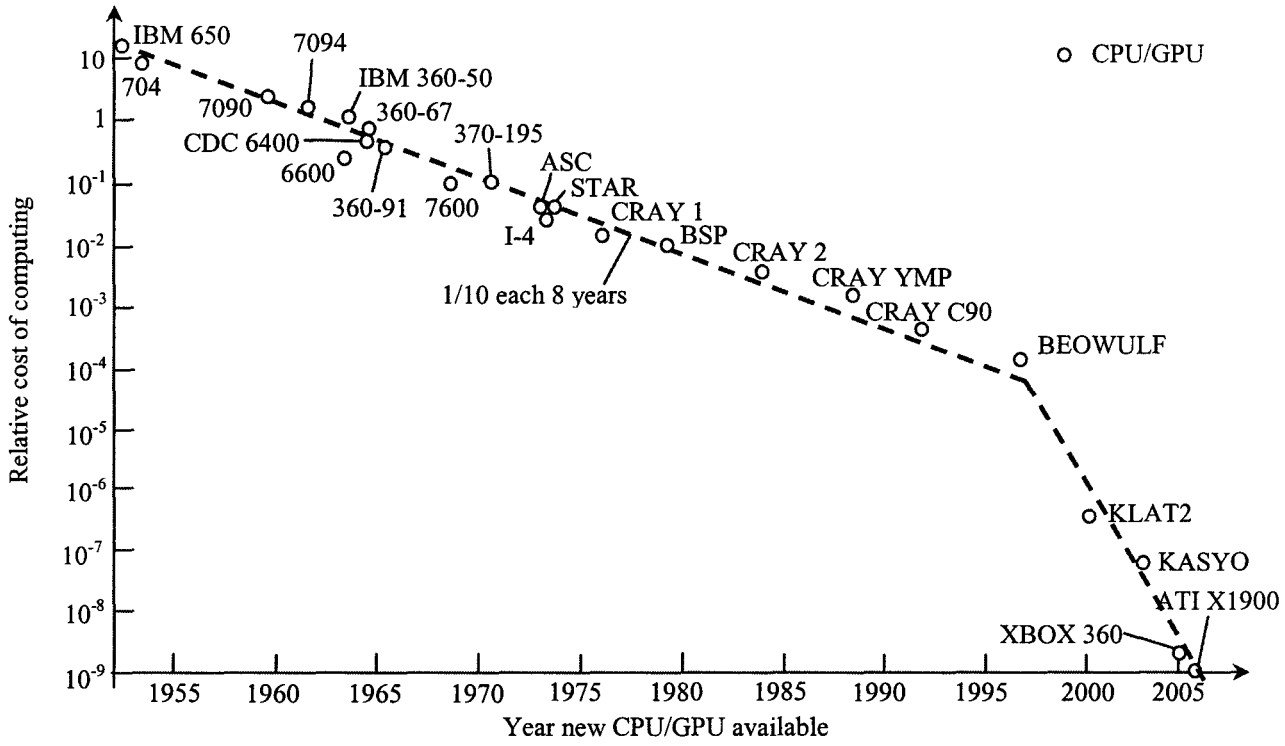

Figure 3-1: Relative cost of computing (adapted from Tannehill *et al.*, 1997, and Wikipedia, 2006a)

The use of computers to perform numerical simulations of fluid dynamics problems is referred to as Computational Fluid Dynamics (CFD). The popularity of CFD has increased with the reduction in the relative cost of computing. CFD is largely based on theoretical analysis and has been successfully employed in studying various flow phenomena and fluid behaviour. In CFD, approximate solutions to the governing partial differential equations are determined by solving a system of algebraic equations which approximately represent reality. Approximations of the partial differential equations are realized through the use of 'discretisation methods'. The flow domain is divided into smaller discrete domains and the approximate equations are applied to these domains in space and time. The results of a CFD simulation are thus obtained at distinct locations in space and time. CFD has several advantages over experimental approaches to fluid systems. An obvious one is that it can be easily employed to study systems that are difficult or impossible to model physically e.g. the experimental simulation of flow around a moving car in a wind tunnel requires that air is blown at a fixed car with the road moving at the same speed as the air; this will be very difficult to model experimentally (Ferziger & Perić, 1999). Other advantages are (Roache, 1982; Fletcher, 1991; Versteeg & Malalasekera, 1995):

i) there is substantial reduction in lead times and costs of new designs.
ii) control over fluid properties such as density, viscosity, etc.
iii) flexibility in the choice of flow parameters.
iv) ability to perform true two dimensional experiments.
v) ability to study systems under hazardous conditions at and beyond their normal performance limits.
vi) provides more detailed and comprehensive information

From the advantages, it appears that CFD is much better than experimental based approaches. The advantages of CFD are however dependent on the accuracy of the solution obtained. Roache (1982) points out that the numerical modeller does not work with continuum equations even though the constitutive equations represent a continuum. This implies that there will invariably be errors. Adequate technical knowledge and extreme care is required to perform computational simulations. The modeller must be fully aware of kind of assumptions and approximations made to arise at a solution in order have an idea about the accuracy of the solution obtained. Perhaps, one of the greatest advantages of numerical modelling is the ability of the modeller to test the sensitivity of the solution to the approximations made and also to estimate the inherent errors. Errors in numerical methods arise as a result of (Ferziger & Perić, 1999):

i) approximations or idealizations made in deriving the governing differential equations.
ii) approximations made in the discretisation process.
iii) methods used in solving the discretised equations e.g. the level of accuracy of a solution obtained using an iterative procedure is dependent on the length of time or the number of iterations that are carried out.

According to Ferziger & Perić (1999), if the governing equations are accurately known (e.g. the Navier-Stokes equations for incompressible fluids), a solution of any desired accuracy can be obtained in principle. However, current knowledge and technology does not make the exact numerical solution of some of the phenomena possible e.g. turbulence, combustion, etc. Due to the approximations made, solutions obtained from numerical simulations need to be validated with experimental data to ascertain whether or not they are a correct representation of reality.

3.1 Components of a CFD model

3.1.1 Mathematical model

The mathematical model is the backbone of every CFD model. This is the collection of equations and boundary conditions that describe or represent the system being modelled. Mathematical models are generally derived analytically or obtained experimentally. They may or may not be exact depending on the assumptions made (if any) in their derivation. The models may be one-, two- or three-dimensional. The basic equations governing fluid flow are the equations for mass, momentum and energy conservation. These equations are presented in the following section.

3.1.1.1 Governing flow equations

In general, there are three laws governing fluid flow. These are:

1. the law of conservation of mass
2. Newton's 2nd law of motion i.e. the rate of change of momentum is equal to the sum of forces on a fluid particle.
3. the 1st law of thermodynamics (the law of conservation of energy). This states that the change in energy is equal to the sum of the rate of heat addition to and the rate of work done on a fluid particle.

The equations describing fluid flow are obtained from these laws. Derivations of the equations are presented in standard texts on fluid dynamics e.g. Rouse (1938), Le Méhauté (1976), White (1991), Versteeg & Malalasekera (1995), etc. The law of conservation of mass yields the equation of mass continuity, which is given as follows (White, 1991):

$$\frac{\partial \rho}{\partial t} + div(\rho \mathbf{v}) = 0 \tag{3.1}$$

where ρ is the fluid density, $\mathbf{v}$ is the velocity vector and t is time. For river flows, which are effectively incompressible, it becomes $div\mathbf{v} = 0$ or in long hand notation (Cartesian coordinates):

$$\frac{\partial u}{\partial x} + \frac{\partial v}{\partial y} + \frac{\partial w}{\partial z} = 0 \tag{3.2}$$

where u, v, w are the fluid velocities in the x, y, and z directions respectively. Considerations of Newton's 2nd law of motion on a fluid particle results in the equations of momentum conservation, which are known as the Navier-Stokes equations. The equations can be written as single equation in vector form using indicial notation as follows (White, 1991):

$$\rho \frac{D\mathbf{v}}{Dt} = \rho \mathbf{g} - \nabla p + \frac{\partial}{\partial x_j}\left[\mu \left(\frac{\partial u_i}{\partial x_j} + \frac{\partial u_j}{\partial x_i} \right) + \delta_{ij} \lambda div\mathbf{v} \right] \tag{3.3}$$

where **g** is the acceleration due to gravity vector, p is the pressure, δ_{ij} is the kronecker delta and λ is the coefficient of bulk viscosity. For a given property, ϕ, the *substantial derivative* is given as:

$$\frac{D\phi}{Dt} = \frac{\partial \phi}{\partial t} + \mathbf{v} \bullet (\nabla \phi) \tag{3.4}$$

Since for river flows $div\mathbf{v} = 0$, Equation 3.3 may be written in long hand form as:

Inertia Forces | *Applied Forces*

Local Inertia | *Convective Inertia* | *Pressure & Gravity* | *Friction Forces*

$$\rho\left(\frac{\partial u}{\partial t} + u\frac{\partial u}{\partial x} + v\frac{\partial u}{\partial y} + w\frac{\partial u}{\partial z}\right) = -\frac{\partial p}{\partial x} + \frac{\partial}{\partial x}\left(2\mu\frac{\partial u}{\partial x}\right) + \frac{\partial}{\partial y}\left[\mu\left(\frac{\partial u}{\partial y} + \frac{\partial v}{\partial x}\right)\right] + \frac{\partial}{\partial z}\left[\mu\left(\frac{\partial u}{\partial z} + \frac{\partial w}{\partial x}\right)\right] \tag{3.5a}$$

$$\rho\left(\frac{\partial v}{\partial t} + u\frac{\partial v}{\partial x} + v\frac{\partial v}{\partial y} + w\frac{\partial v}{\partial z}\right) = -\frac{\partial p}{\partial y} + \frac{\partial}{\partial x}\left[\mu\left(\frac{\partial v}{\partial x} + \frac{\partial u}{\partial y}\right)\right] + \frac{\partial}{\partial y}\left(2\mu\frac{\partial v}{\partial y}\right) + \frac{\partial}{\partial z}\left[\mu\left(\frac{\partial v}{\partial z} + \frac{\partial w}{\partial y}\right)\right] \tag{3.5b}$$

$$\rho\left(\frac{\partial w}{\partial t} + u\frac{\partial w}{\partial x} + v\frac{\partial w}{\partial y} + w\frac{\partial w}{\partial z}\right) = -\rho g - \frac{\partial p}{\partial z} + \frac{\partial}{\partial x}\left[\mu\left(\frac{\partial w}{\partial x} + \frac{\partial u}{\partial z}\right)\right] + \frac{\partial}{\partial y}\left[\mu\left(\frac{\partial w}{\partial y} + \frac{\partial v}{\partial z}\right)\right] + \frac{\partial}{\partial x}\left(2\mu\frac{\partial w}{\partial z}\right) \tag{3.5c}$$

Claude-Louis Navier was the first to derive the momentum conservation equations in 1842. The derivation, however, did not account for shear stresses. Saint Venant is believed to be the first person to correctly derive the equations, accounting for shear stresses, and published the derivation in 1843. George Gabriel Stokes also correctly derived the equations independently but only published the results in 1845 (O'Conner & Robertson, 2000; Girvan, 2003).

The first law of thermodynamics also results in the equation for energy conservation, which is given as:

$$\rho\frac{Dh_t}{Dt} = \frac{Dp}{Dt} + div(k_t \nabla T) + \Phi \tag{3.6}$$

where h_t is the fluid enthalpy, T is the temperature, k_t is the coefficient of thermal conductivity and Φ is the dissipation function. The term $div(k_t \nabla T)$ represents the rate of heat addition to a fluid particle due to heat conduction. The dissipation function, Φ, has already been presented in Section 2.5.2.4. It represents the energy dissipated as a result of shearing action on the particle surfaces and is given as:

$$\Phi = \tau_{ij} \frac{\partial u_i}{\partial x_j} \tag{3.7}$$

For incompressible flows, Equation 4.8 becomes (White, 1991):

$$\rho c_p \frac{DT}{Dt} = div(k_t \nabla T) + \Phi \tag{3.8}$$

where c_p is the specific heat of the fluid. Equation 3.8 is obtained from Equation 3.6 using the thermodynamic relationship:

$$dh_t = c_p dT + (1 - \beta_t T)\frac{dp}{\rho} \tag{3.9}$$

where β_t is the coefficient of thermal expansion.

3.1.1.2 Turbulence modelling

Most fluid flows of engineering concern are turbulent. Turbulent flows are characterised by fluctuations in flow parameters about a mean value. Fluid particles move in a random manner and diffusion rates of scalar parameters are generally greater than the rates in laminar flow. Turbulent flows are unsteady, non-uniform and rotational. However, dividing turbulent flow parameters into mean and fluctuating components allows the average motion to be considered as steady, uniform or irrotational. Figure 3-2 shows the variation of velocity at a point in a flowing fluid for turbulent steady and unsteady mean flows.

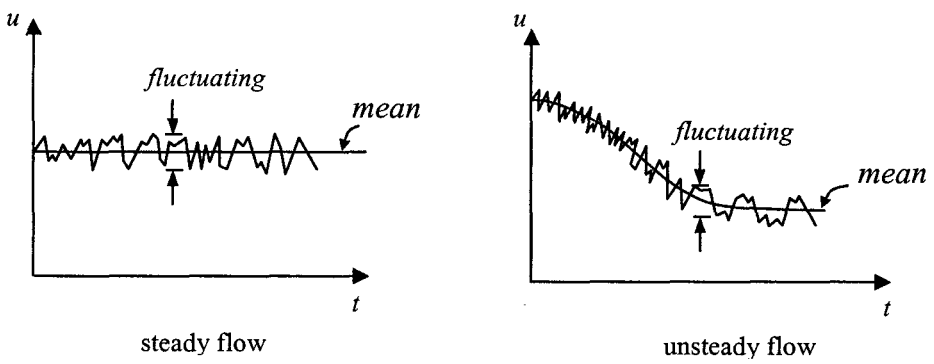

Figure 3-2: Velocity variation at a point in turbulent flow (Tannehill *et al.*, 1997)

Turbulence is a key aspect of flow as it affects the distribution of flow parameters throughout the domain. The Navier-Stokes equations are valid for turbulent fluid flows and so it is technically possible to model turbulent flows using direct numerical simulation (DNS). The truth, however, is that the computational demand for direct numerical simulation is enormous. DNS of turbulent flows requires the resolution of all the length scales involved, including the smallest eddies. Discretisation of the time scale should also be such that small-scale motion is resolved accurately. According to Tannehil *et al.* (1997), the computational demand of DNS is so large that only very simple flows at low Reynolds numbers can be computed with present day machines. Wilcox (1993) presents the following formula for estimating the number of grid points, N_{DNS} required for flow in a channel:

$$N_{DNS} = \left(0.088 Re_h\right)^{9/4} \tag{4.10}$$

where Re_h is a Reynolds number dependent on the channel height and average flow velocity. Examples of turbulent flows that have been simulated using DNS include flow over a plate, flow over a rearward facing step, and planar and square channel flows (Tannehil *et al.*, 1997). Although computational power continues to increase, it is uncertain if this trend will persist or whether or not DNS will soon be a viable option for the simulation of most turbulent flows.

Current methods of simulating most turbulent flows involve modification of the Navier-Stokes equations. The flow parameters are spatially or temporally averaged to yield equations which can be solved using less computational resources when appropriate assumptions are made. Simulation of turbulent flows using the so-called Large Eddy Simulation (LES) requires that flow parameters be spatially averaged over regions which are about the size of a cell. This method is the next in line after DNS in terms of computational demands. LES is based on two presumptions; i) the global features of turbulent flows are mainly governed by the larger eddies and ii) the smaller eddies are somewhat isotropic (especially at high Reynolds numbers). Only the large turbulent eddies are thus simulated directly. The effects of the small eddies are modelled using what are known as subgrid-scale (SGS) models. In LES, the Navier-Stokes equations are "filtered" by decomposing the flow variables into filtered (large) and residual (subgrid) scales. The resulting filtered equations describe the evolution of the large eddies but contain stress terms which represent the small scale motions. These stress terms are evaluated using SGS models. As already stated, the computational demands for LES are also quite large. Chapman (1979) estimated the number of grid cells required for LES of flow around a large aircraft (with a Re of 10^7) to be 8×10^8. LES is becoming more popular with the increasing number of FLOPS that can be carried out on present day computers. (Peyret, 1996; Tannehill *et al.*, 1997; Wesseling, 2001).

Time averaging of the flow parameters in the Navier-Stokes Equations results in the set of equations known as the Reynolds Averaged Navier-Stokes (RANS) equations (after Reynolds, 1894). Here, the flow variables are decomposed into time-mean and fluctuating components and averaged over a considerable period of time. The RANS equations for incompressible flow are given in Cartesian coordinates as follows:

$$\rho\left(\frac{\partial \bar{u}}{\partial t}+\frac{\partial \bar{u}^2}{\partial x}+\frac{\partial \overline{uv}}{\partial y}+\frac{\partial \overline{uw}}{\partial z}\right)=-\frac{\partial \bar{p}}{\partial x}+\frac{\partial}{\partial x}\left(2\mu\frac{\partial \bar{u}}{\partial x}\right)+\frac{\partial}{\partial y}\left[\mu\left(\frac{\partial \bar{u}}{\partial y}+\frac{\partial \bar{v}}{\partial x}\right)\right]+\frac{\partial}{\partial z}\left[\mu\left(\frac{\partial \bar{u}}{\partial z}+\frac{\partial \bar{w}}{\partial x}\right)\right]$$
$$-\left(\frac{\partial \rho\overline{u'^2}}{\partial x}+\frac{\partial(\rho\overline{u'v'})}{\partial y}+\frac{\partial(\rho\overline{u'w'})}{\partial z}\right) \tag{3.11a}$$

$$\rho\left(\frac{\partial \bar{v}}{\partial t}+\frac{\partial \overline{uv}}{\partial x}+\frac{\partial \bar{v}^2}{\partial y}+\frac{\partial \overline{vw}}{\partial z}\right)=-\frac{\partial \bar{p}}{\partial y}+\frac{\partial}{\partial x}\left[\mu\left(\frac{\partial \bar{v}}{\partial x}+\frac{\partial \bar{u}}{\partial y}\right)\right]+\frac{\partial}{\partial y}\left(2\mu\frac{\partial \bar{v}}{\partial y}\right)+\frac{\partial}{\partial z}\left[\mu\left(\frac{\partial \bar{v}}{\partial z}+\frac{\partial \bar{w}}{\partial y}\right)\right]$$
$$-\left(\frac{\partial(\rho\overline{u'v'})}{\partial y}+\frac{\partial \rho\overline{v'^2}}{\partial x}+\frac{\partial(\rho\overline{v'w'})}{\partial z}\right) \tag{3.11b}$$

$$\rho\left(\frac{\partial \bar{w}}{\partial t}+\frac{\partial \overline{uw}}{\partial x}+\frac{\partial \overline{vw}}{\partial y}+\frac{\partial \bar{w}^2}{\partial z}\right)=-\rho g-\frac{\partial \bar{p}}{\partial z}+\frac{\partial}{\partial x}\left[\mu\left(\frac{\partial \bar{w}}{\partial x}+\frac{\partial \bar{u}}{\partial z}\right)\right]+\frac{\partial}{\partial y}\left[\mu\left(\frac{\partial \bar{w}}{\partial y}+\frac{\partial \bar{v}}{\partial z}\right)\right]+\frac{\partial}{\partial x}\left(2\mu\frac{\partial \bar{w}}{\partial z}\right)$$
$$-\left(\frac{\partial(\rho\overline{u'w'})}{\partial y}+\frac{\partial(\rho\overline{v'w'})}{\partial z}+\frac{\partial \rho\overline{w'^2}}{\partial x}\right) \tag{3.11c}$$

where the over bar ($\bar{}$) is used to represent the mean flow quantities and the prime (') is used to represent the fluctuating components. The quantities $-\rho\overline{u'^2}$, $-\rho\overline{v'^2}$, $-\rho\overline{w'^2}$, $-\rho\overline{u'v'}$, $-\rho\overline{u'w'}$ and $-\rho\overline{v'w'}$ are known as Reynolds stresses (or apparent turbulent stresses) and are responsible for momentum exchange in the turbulent mixing process. The Reynolds stresses are also unknown. This poses a problem as the number of unknowns become more than the number of equations. This is known as the 'closure' problem. Closure can be achieved by making assumptions to derive extra equations involving the Reynolds stresses or to relate the Reynolds stresses to the mean flow parameters.

Boussinesq (1877) hypothesised that the Reynolds stresses may be expressed in terms of the mean velocity gradients by the introduction of a coefficient of molar viscosity (eddy viscosity concept). This coefficient, ν_t, known as the eddy viscosity, has the same dimensions as the dynamic viscosity (Rouse, 1939). From this concept, the Reynolds stresses may be expressed as follows:

$$-\rho\overline{u'^2} = \overline{\tau_{xx}} = 2\nu_t\left(\frac{\partial\bar{u}}{\partial x}\right); \quad -\rho\overline{v'^2} = \overline{\tau_{yy}} = 2\nu_t\left(\frac{\partial\bar{v}}{\partial y}\right); \quad -\rho\overline{u'v'} = \overline{\tau_{xy}} = \nu_t\left(\frac{\partial\bar{u}}{\partial y}+\frac{\partial\bar{v}}{\partial x}\right)$$

$$-\rho\overline{w'^2} = \overline{\tau_{zz}} = 2\nu_t\left(\frac{\partial\bar{w}}{\partial z}\right); \quad -\rho\overline{u'w'} = \overline{\tau_{xz}} = \nu_t\left(\frac{\partial\bar{u}}{\partial z}+\frac{\partial\bar{w}}{\partial x}\right); \quad -\rho\overline{v'w'} = \overline{\tau_{yz}} = \nu_t\left(\frac{\partial\bar{v}}{\partial z}+\frac{\partial\bar{w}}{\partial y}\right) \tag{3.12}$$

The majority of the current turbulence models are based on the eddy viscosity concept. These models are also known as first-order models. First-order models may be categorized into zero equation (simple algebraic) models, one-half equation models, one equation models, one-and-one-half equation models and two equation models. This classification is based on the type and number of additional equations that are used to determine the eddy viscosity or any of its dependent variables e.g. the turbulence length scale.

In zero equation models, simple algebraic equations are used to estimate ν_t. Prandtl's mixing length model is an example. From Equations 2.6 and 3.12, the eddy viscosity may be represented using (Peyret, 1996; Tannehil *et al.*, 1999):

$$\nu_t = \rho l^2\left|\frac{\partial\bar{u}}{\partial y}\right| \tag{3.13}$$

The relationships used to evaluate the length scale, l, are simple algebraic expressions which are dependent on the type of flow being modelled e.g. for zero pressure gradient flows along a solid surface l may be determined as follows

inner layer:

$$l_i = \kappa y\left(1-e^{-y^+/A^+}\right) \tag{3.14}$$

outer layer:

$$l_o = C\delta \tag{3.15}$$

where A^+ is a damping constant, $y^+ = \bar{u}y/\nu$, C is a constant which is usually assigned a value of 0.089, and δ is the boundary layer thickness.

In one-half equation models, ordinary differential equations are used to describe the variation of the eddy viscosity (or any of its dependent variables) with flow. It is usually assumed that the parameter used varies in one direction. These models are similar to algebraic models. Johnson & Coakley (1990) presented the following one-half equation model, which was used in solving transonic flow problems:

inner layer:

$$\nu_t = l^2 \left. \frac{\sqrt{\tau_{xy}}}{\kappa y} \right|_m \tag{3.16}$$

outer layer:

$$\nu_t = 0.0168 u_e \delta^* \sigma(x) \left[1 + 5.5 \left(y/\delta \right)^6 \right]^{-1} \tag{3.17}$$

where u_e is the edge velocity, δ^* is the displacement thickness, y is the distance from the wall, δ is the thickness of the boundary layer, the subscript m denotes the maximum value, and $\sigma(x)$ is a factor that accounts for non-equilibrium streamwise evolution of flow. $\sigma(x)$ is adjusted at each location so that the following equation is satisfied:

$$\nu_t|_m = \frac{-\tau_{xy}|_m}{\partial u/\partial y|_m} \tag{3.18}$$

The shear stress, τ_{xy}, is unknown and its value is determined using an ordinary differential equation. This equation was derived based on the turbulent kinetic energy and by ignoring viscous diffusion effects. It is given as follows:

$$u_m \frac{d\tau_m}{dx} = 0.25 \left(\sqrt{\tau_{meq}} - \sqrt{\tau_m} \right) \frac{\tau_m}{L_m} - C_{diff} \frac{\tau_m^{3/2}}{\left(0.7\delta - y_m \right)} \left[1 - \sigma^{1/2}(x) \right] \tag{3.19}$$

where τ_{meq} is the equilibrium value ($\sigma(x) = 1$) for shear stress, C_{diff} = 0.5 for $\sigma(x) \geq 1$ or 0 otherwise, and L_m is the dissipation length scale given by:

$$L_m = \kappa y, \qquad y_m/\delta \leq 0.09/\kappa$$

$$L_m = 0.09\delta, \qquad y_m/\delta > 0.09/\kappa \tag{3.20}$$

In one equation models, an extra partial differential equation is solved. An example is presented by Tannehil *et al.* (1997). In this instance the eddy viscosity is determined as follows:

$$\nu_t = C_k \rho l k^{1/2} \tag{3.21}$$

where k is the turbulent kinetic energy and C_k is a constant. The turbulent kinetic energy is determined using the turbulent kinetic energy equation, which may be written in indicial notation as follows:

$$\rho \frac{Dk}{Dt} = \frac{\partial}{\partial x_j}\left[\left(\mu + \nu_t / Pr_k\right)\frac{\partial k}{\partial x_j}\right] + \left[\nu_t\left(\frac{\partial \overline{u}_i}{\partial x_j} + \frac{\partial \overline{u}_j}{\partial x_i}\right) - \frac{2}{3}\rho k \delta_{ij}\right]\frac{\partial \overline{u}_i}{\partial x_j} - \rho\varepsilon \tag{3.22}$$

where $Pr_k \approx 1$. The rate of dissipation, ε, is related to the turbulent kinetic energy as follows:

$$\varepsilon = C_D k^{3/2} / l \tag{3.23}$$

Again, l is specified algebraically. $C_D \simeq 0.164$ if l is take as the ordinary mixing length.

One-and-one-half-equation models use two additional equations for modelling turbulence. One equation is a PDE and the other is an ODE e.g. the one-equation model described above may be modified into a one-and-one-half-equation model by describing the variation of l with flow using an ODE instead of the simple algebraic expression. Two-equation models involve the use of two additional PDEs. Two-equation models typically have the turbulent kinetic energy equation as one of the additional equations. The remaining PDE usually models the variation of one of k's dependent factors e.g. the dissipation rate, ε, the specific dissipation rate, $\omega_{ke} = \varepsilon / k$, and the dissipation time, $\tau_k = 1/\omega_{ke}$. One of the most popular two-equation models is the standard k-ε model, where the additional PDEs are for k and ε respectively. According to Olsen (2000), this method is versatile since its empirical constants are relatively universal. All turbulence models need to be verified by comparing the results they produce with experimental data. The k-ε model has successfully been applied to large number of different flow situations. The PDEs for k and ε in a standard k-ε model are given as follows:

turbulent kinetic energy:

$$\rho \frac{Dk}{Dt} = \frac{\partial}{\partial x_j}\left[\left(\mu + \nu_t / Pr_k\right)\frac{\partial k}{\partial x_j}\right] + \left[\nu_t\left(\frac{\partial \overline{u}_i}{\partial x_j} + \frac{\partial \overline{u}_j}{\partial x_i}\right) - \frac{2}{3}\rho k \delta_{ij}\right]\frac{\partial \overline{u}_i}{\partial x_j} - \rho\varepsilon \tag{3.22}$$

dissipation rate:

$$\rho\frac{D\varepsilon}{Dt}=\frac{\partial}{\partial x_j}\left[\left(\mu+\nu_t/Pr_\varepsilon\right)\frac{\partial\varepsilon}{\partial x_j}\right]+C_{\varepsilon 1}\frac{\varepsilon}{k}\left[\nu_t\left(\frac{\partial\overline{u}_i}{\partial x_j}+\frac{\partial\overline{u}_j}{\partial x_i}\right)-\frac{2}{3}\rho k\delta_{ij}\right]\frac{\partial\overline{u}_i}{\partial x_j}-C_{\varepsilon 2}\rho\frac{\varepsilon^2}{k} \tag{3.24}$$

The turbulent viscosity is determined as follows:

$$\nu_t=C_\mu\rho\frac{k^2}{\varepsilon} \tag{3.25}$$

The standard model constants are:

$C_\mu=0.09$, $Pr_k=1.0$, $Pr_\varepsilon=1.3$, $C_{\varepsilon 1}=1.44$, and $C_{\varepsilon 2}=1.92$

Various variations of the standard k-ε model have been developed. Two of these are the Renormalization group (RNG) and the realizable k-ε models. The equations for these models are similar but they differ in the way the turbulent viscosity, turbulent Prandtl numbers (Pr_k & Pr_ε), and the generation and dissipation terms of ε are computed. In the RNG k-ε model, analytically-derived formulas are used to represent the Prandtl numbers. For the realizable k-ε model, different formulations are used for the turbulent viscosity and the dissipation rate. The formulations are based on exact equations of vorticity fluctuations (Launder & Spalding, 1972; Yakhot & Orszag, 1986; Shih *et al.*, 1995).

Second-order or second-moment models are not based on the eddy viscosity concept. Reynolds stress models (also known as stress-equation models) are second-order models. In these models, additional PDEs are derived for all the Reynolds stresses. These equations are usually solved along with the equation for ε. Second-order models are thus considered to be more general than first order models. However, they are computationally more demanding since more equations are involved. Versteeg & Malalasekera (1995) present the following transport equation for Reynold stress:

$$\frac{D\overline{u_i'u_j'}}{Dt}=P_{ij}+div\left[\frac{\nu_t}{Pr_k}\nabla\left(\overline{u_i'u_j'}\right)\right]-\frac{2}{3}\varepsilon\delta_{ij}-C_1\frac{\varepsilon}{k}\left(\overline{u_i'u_j'}-\frac{2}{3}k\delta_{ij}\right)-C_2\left(P_{ij}-\frac{2}{3}p\delta_{ij}\right)+\Omega_{ij} \tag{3.26}$$

where

$$P_{ij}=-\left(\overline{u_i'u_m'}\frac{\partial u_j}{\partial x_m}+\overline{u_j'u_m'}\frac{\partial u_i}{\partial x_m}\right) \quad \text{and} \quad \Omega_{ij}=-2\omega_k\left(\overline{u_j'u_m'}\varepsilon_{ikm}+\overline{u_i'u_m'}\varepsilon_{jkm}\right)$$

ω_k is a rotation vector, ε_{ijk} is the permutation operator, C_1 = 1.8 and C_2 = 0.6. The turbulent kinetic energy is determined by adding the three normal apparent stresses i.e.

$$k = \frac{1}{2}\left(u_1'^2 + u_2'^2 + u_3'^2\right) \tag{3.27}$$

Again, the eddy viscosity is determined from Equation 3.25 above.

Sometimes, modelling assumptions are made which make it possible to develop a non-linear relationship between the Reynolds stresses and the velocity gradients. This makes it possible to determine a solution without solving the actual Reynolds stress PDEs. The relationships are usually solved together with the PDEs for k and ε. Such a model is known as an Algebraic Reynolds Stress Model (ARSM). ARSMs take on the form of two-equation models. The difference, however, is that the eddy viscosity is replaced with a function. ARSMs normally require more computational power than two-equation models but are computational less demanding than normal Reynold Stress models (RSM).

3.1.2 Discretisation method

Another key component of every CFD model is the method used to approximate the governing differential equations. Several methods or approaches are used in CFD. These include Finite Difference methods, Finite Volume Methods, Finite Element Methods, Spectral Schemes, Boundary Element Methods and Cellular Automata (Versteeg & Malalasekera,1995; Ferziger & Perić, 1999; Tannehill *et al.*, 1997; Massey & Smith, 1998 ; Chadwick *et al.*, 2004). Some of the methods i.e. Spectral Schemes, Boundary Element Methods and Cellular Automata are generally used for, or limited to, specific problems. The main ones that are normally applied in CFD are the Finite Difference, the Finite Volume and the Finite Element Methods.

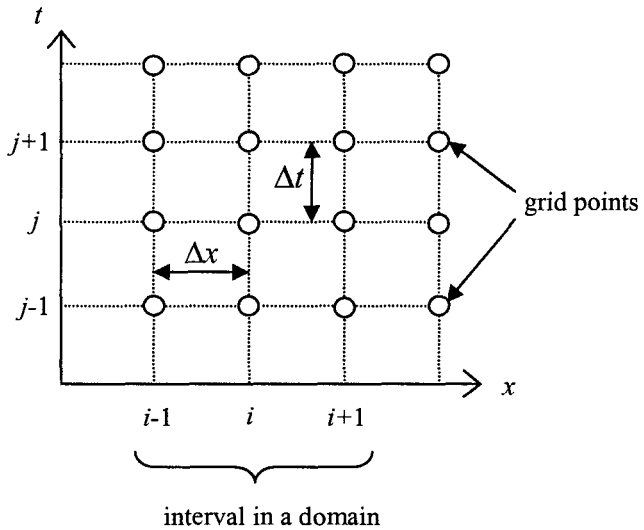

$$\left(\frac{\partial u}{\partial t}\right)_{i,j} = \frac{u_{i,j} - u_{i,j-1}}{\Delta t}$$

$$\left(\frac{\partial^2 u}{\partial x^2}\right)_{i,j} = \frac{u_{i+1,j} - 2u_{i,j} + u_{i-1,j}}{\Delta x^2}$$

Figure 3-3: Finite Difference approximations for a given interval (after Smith, 1985)

According to Ferziger & Perić (1999), the Finite Difference Method is the oldest and simplest method of discretisation used for the numerical solution of partial differential equations and is

believed to have been introduced by Euler in the 18th century. Finite Difference Methods involve the transformation of the derivatives in the partial differential equations over small intervals in the domain. The domain is covered by a grid and the partial derivatives are replaced with algebraic equations representing the functional values at the individual grid nodes and their neighbouring nodes i.e. an algebraic equation approximating the partial derivatives exists at each node. The result is a collection of algebraic equations which are solved iteratively or by matrix inversion. The approximating algebraic equations are obtained using polynomial fitting or truncated Taylor series expansions. Examples of derivative approximations for a given interval are shown in Figure 3-3 for the function $\partial u/\partial t + \partial^2 u/\partial x^2 = 0$ (Smith, 1985; Ferziger & Perić, 1999).

The integral form of the governing equations is the focal point of Finite Volume Methods. The domain is divided into finite "control volumes". The governing equations are integrated over all the control volumes. This is followed by the discretisation of the resulting equations in each control volume using a variety of Finite Difference type approximations. The algebraic equations formed are then solved numerically. The unknowns in Finite Volume Methods are determined within the control volumes (usually at the centroid) and not at their nodes (vertices) or surfaces. The equations resulting from the integration of the governing equations express the conservation of the flow variables for each control volume i.e. there is a clear relationship between the numerical algorithm and the underlying physical conservation principle. (Versteeg & Malalasekera, 1995; Ferziger & Perić, 1999; Weisstein, 2005).

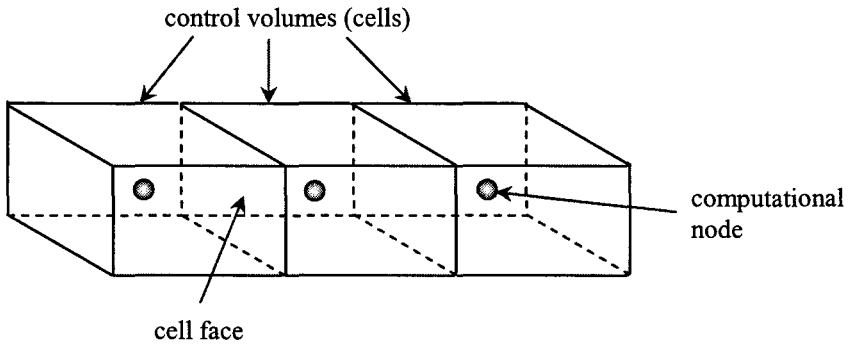

Figure 3-4: Control volumes – Finite Volume approach

Finite Elements Methods use simple piecewise functions valid on 'elements' to describe the local variations of unknown flow variables. The domain is subdivided into discrete volumes or "finite elements". (In 2D the elements may be triangles or quadrilaterals. In 3D they are usually tetrahedral or hexahedra). The points referring to these elements are called nodes. A system of algebraic equations with unknown nodal values is derived for each element using interpolation functions (usually piecewise polynomials), which approximately describe the local variation of the unknown variables. The equations for all the elements are then gathered together to form a global system of equations that are solved numerically (Ninomiya & Onishi, 1991; Ferziger & Perić, 1999).

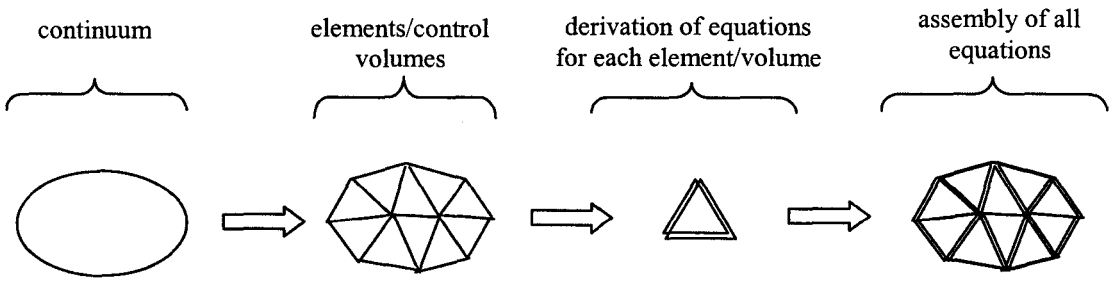

Figure 3-5: Finite Element and Finite Volume approaches (adapted from Ninomiya & Onishi, 1991)

Unlike the aforementioned methods, the approximating equations in Spectral Schemes are valid throughout the entire the domain and not at local points. The equations in this case are obtained using truncated Fourier series or series of Chebyshev polynomials which are accurate for smooth functions (Versteeg & Malalasekera, 1995).

Cellular Automata are discrete dynamical systems. The domain consists of a grid of cells. Each cellular automaton can take on any one of a certain finite number of states. The state of a cell is time-dependent and is updated depending on a 'local' rule i.e. the state of a cell at a given time step is dependent on the states of its neighbouring cells in the previous time step. Time advances are also discrete i.e. all the Cellular Automata are updated in sync (Weisstein, 2006; Wikipedia, 2006b).

The Boundary Element Method is used to solve the partial differential equations of systems with well defined boundary conditions. The governing equations, which represent the entire domain, are transformed into surface integral equations over the enclosing domain boundaries. The boundary surfaces are discretised into 'boundary' elements and the surface integral equations are solved for only boundary values. In terms of computer resources, this method is more efficient for problems with small surface to volume ratios (Lam, 2006; Wikipidia, 2006c).

3.1.3 Coordinate system

The basic governing equations presented in section 3.1.1.1 were derived in Cartesian coordinates. The form of these equations can change depending on the coordinate system within which the modelling is being carried out. In tensor form, the equations are coordinate free. The coordinate systems may be orthogonal or non-orthogonal. Also, they may be fixed (inertial) or moving (non-inertial). The system used is dependent on the flow being modelled e.g. it may be necessary to use a moving coordinate system when modelling flow over rotating turbine blades or it may be necessary to use a non-orthogonal curvilinear coordinate system when modelling flow in a very complex domain (White, 1995; Ferziger & Perić, 1999).

3.1.4 Computational grid

Grids or meshes are used to divide the computational domain into sub-domains (cells, control volumes, elements, etc.). A grid is described by Malvriplis (1996) as an artificial construction which facilitates the spatial discretisation of the governing equations to be solved. The grid determines the locations at which the flow variables will be evaluated. The nature and density distribution of a grid affects the efficiency and accuracy of the numerical method that is employed. The grid used should be such that the governing equations are accurately represented. The simplest and least popular kind of grid is the Cartesian grid. The cells in a Cartesian grid are rectangular i.e. the grid points are spaced at equal intervals throughout the entire domain. This type of grid is ideal for flows with non-localized gradients and simple geometries. The grid is easy to generate and grid points need not be stored (Wesseling, 2001).

In general, grids may be broadly categorised into two types; structured grids and unstructured grids. The interiors vertices of all structured grids are linked to the same number of cells. Ferziger & Perić (1999) describe structured grids as consisting of families of grid lines with the property that members of a single family do not cross each other and cross each member of the other families only once. Cartesian grids are thus structured. The difference between Cartesian grids and other structured grids is the fact that boundary complexities are avoided in the latter by ensuring that the grid lines conform to the boundaries, resulting in a warped Cartesian-type grid. In Cartesian grids, grid points may fall outside the flow domain (see Figure 3-6) and accurate implementation of boundary conditions is not simple. Cartesian grids may be modified to cater for complex domains using the cut-cell approach. In this approach, points falling outside the flow domain are discarded. This results in a collection of cells intersecting with the flow boundaries. In regions of large gradients, cells may be subdivided to obtain smaller cells that will be able to resolve the gradients.

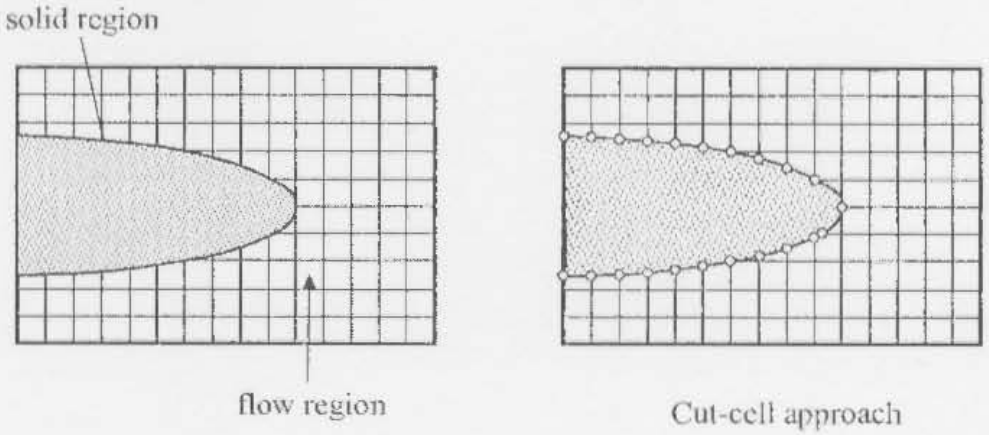

Figure 3-6: Cartesian grid

Normally, structured grids are used for relatively simple but non-trivial domains. Their data structure is simple. The locations of the grid points need to be stored but the nature of the grid connectivity is such that it is unnecessary to store the identity of neighbouring grid points as these are implicitly known. As the complexity of the domain geometry increases, it becomes more difficult to fit the grid in such a manner that it conforms to all the boundaries. Two types of structured grids may be used under such circumstances; i) block-structured grids and ii) overset

grids (also called composite or chimera grids). In block-structured grids, the complex flow domain is split up into simpler sub-domains and a structured grid is applied to each sub domain. Special treatment is required at the interfaces between the sub-domains as the grids may or may not match at the interface (see Figure 3-7). In overset grids, the domain is discretized using two or more overlapping structured grids. It is thus necessary to interpolate values between the various grids in the region of overlap during the solution process. Elements in structured grids are typically quadrilateral (2D) and hexahedral (3D).

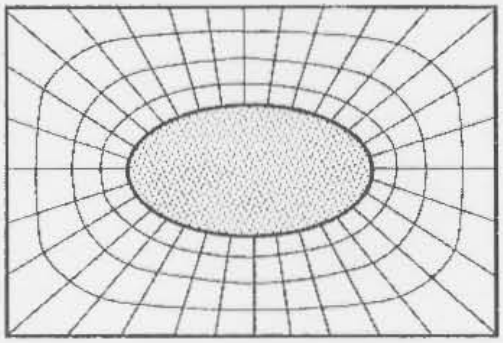

Structured grid

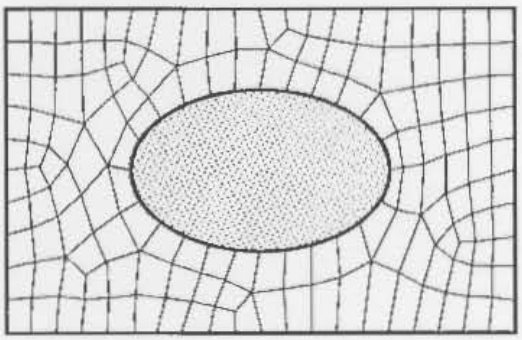

Unstructured grid

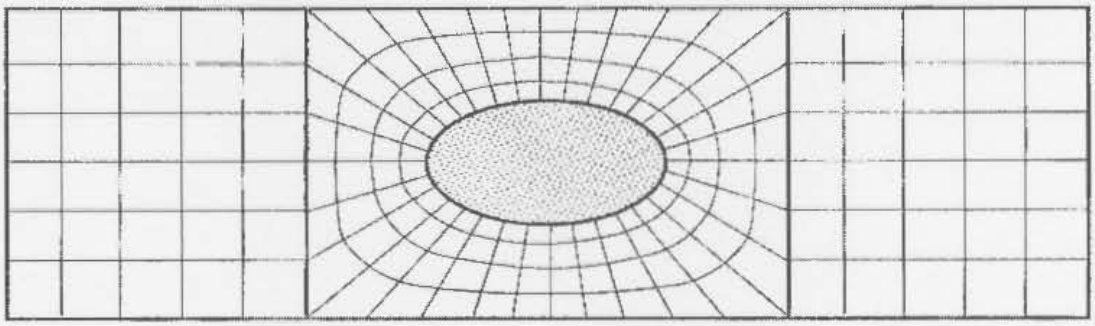

Block-structured grid

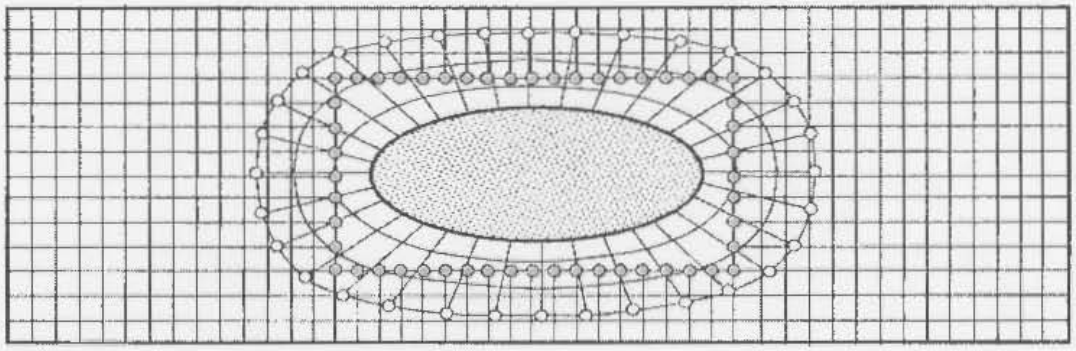

overset grid

Figure 3-7: Different types of grids

Unlike structured grids, unstructured grids consist of elements which are not ordered in any particular manner. They, however, still conform to the boundaries of the domain. The number of neighbouring elements or nodes is unrestricted. Unstructured grids are flexible for discretising domains with complex geometries and are easier to create than structured grids, especially in 3D. The irregular nature of the connectivity of these types of grids makes it necessary to store the location of the grid points as well as the identities of the neighbouring points for each vertex. This means that unstructured grids require more computational resources. Elements in unstructured grids may be triangles or quadrilaterals (2D) and tetrahedral or hexahedral (3D). Owing to the regular nature of structured grids, manipulation of the resulting algebraic equations is much simpler than that for unstructured grids. The outcome is that solutions are obtained much easier and quicker on a structured grid than on an unstructured one.

Grids may further be divided into orthogonal or non-orthogonal grids depending on the nature of the grid lines. Orthogonal grids are generally used for regular geometries. The grid lines follow the coordinate directions which are orthogonal. Non-orthogonal grids are normally employed in most CFD packages to compute flows in complex geometries. These grids are easily adapted to fit any geometry and may be structured or unstructured. Boundary conditions are easy to implement on non-orthogonal grids as the grid lines conform to the boundaries. Also, accuracy may be enhanced by adapting the grid to the flow. The main disadvantage of non-orthogonal grids, however, is the fact that co-ordinate transformations result in equations with an increased number of terms making them computationally more expensive.

3.1.5 Solution method and convergence criteria

The method employed to solve the discretised governing equations is dependent on the nature of the equations, the type of grid and the number of unknowns. Matrices or iterative procedures are normally employed. Non-linear equations in particular are usually solved using iterative procedures. When iterative methods are used, it is necessary to define convergence criteria i.e. limits at which iterations will be halted. The points at which iterations are halted are crucial as they affect the efficiency and accuracy of a method of solution. Convergence criteria are thus important and have to be selected with caution (Ferziger & Perić, 1999). Figure 3-8 illustrates the iterative method employed in the segregated solver of FLUENT.

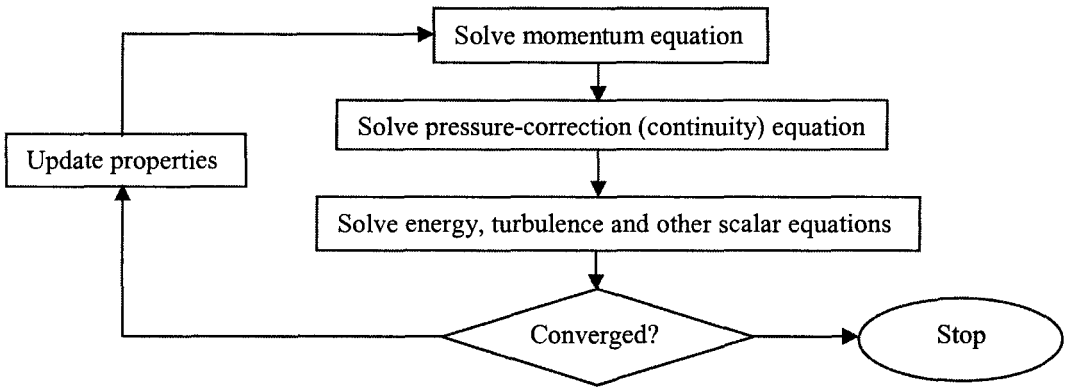

Figure 3-8: Iterative solution procedure used in FLUENTs segregated solver (after Fluent, 2005)

Unlike structured grids, unstructured grids consist of elements which are not ordered in any particular manner. They, however, still conform to the boundaries of the domain. The number of neighbouring elements or nodes is unrestricted. Unstructured grids are flexible for discretising domains with complex geometries and are easier to create than structured grids, especially in 3D. The irregular nature of the connectivity of these types of grids makes it necessary to store the location of the grid points as well as the identities of the neighbouring points for each vertex. This means that unstructured grids require more computational resources. Elements in unstructured grids may be triangles or quadrilaterals (2D) and tetrahedral or hexahedral (3D). Owing to the regular nature of structured grids, manipulation of the resulting algebraic equations is much simpler than that for unstructured grids. The outcome is that solutions are obtained much easier and quicker on a structured grid than on an unstructured one.

Grids may further be divided into orthogonal or non-orthogonal grids depending on the nature of the grid lines. Orthogonal grids are generally used for regular geometries. The grid lines follow the coordinate directions which are orthogonal. Non-orthogonal grids are normally employed in most CFD packages to compute flows in complex geometries. These grids are easily adapted to fit any geometry and may be structured or unstructured. Boundary conditions are easy to implement on non-orthogonal grids as the grid lines conform to the boundaries. Also, accuracy may be enhanced by adapting the grid to the flow. The main disadvantage of non-orthogonal grids, however, is the fact that co-ordinate transformations result in equations with an increased number of terms making them computationally more expensive.

3.1.5 Solution method and convergence criteria

The method employed to solve the discretised governing equations is dependent on the nature of the equations, the type of grid and the number of unknowns. Matrices or iterative procedures are normally employed. Non-linear equations in particular are usually solved using iterative procedures. When iterative methods are used, it is necessary to define convergence criteria i.e. limits at which iterations will be halted. The points at which iterations are halted are crucial as they affect the efficiency and accuracy of a method of solution. Convergence criteria are thus important and have to be selected with caution (Ferziger & Perić, 1999). Figure 3-8 illustrates the iterative method employed in the segregated solver of FLUENT.

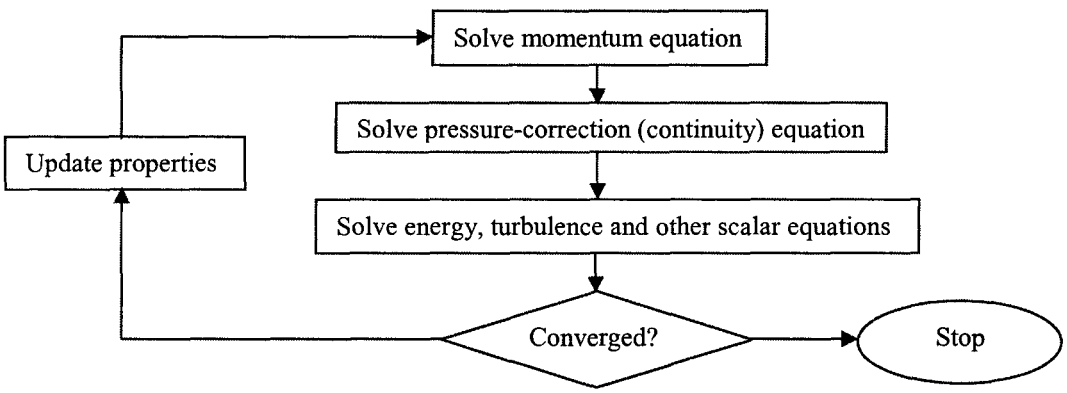

Figure 3-8: Iterative solution procedure used in FLUENTs segregated solver (after Fluent, 2005)

3.2 CFD software

According to Versteeg & Malalasekera (1995), all CFD software packages consist of three main elements. These are;

i) the pre-processor
ii) the solver and
iii) the post-processor.

The flow problem is defined in the pre-processor. The first activity is the definition of the flow domain. Once this is done, the domain is spatially discretised using an appropriate grid. The next step is to select the flow phenomena that will be modelled. This is followed by the definition of the fluid properties. Specification of the boundary conditions concludes the pre-processing phase (Versteeg & Malalasekera, 1995).

Once the pre-processing phase is over, the solver is employed to carry out the actual solution of the governing equations. In the solver, variations in the unknown flow variables are approximated using simple functions. The governing equations are then discretized by substituting the partial differentials with the approximations. The algebraic equations that result from the discretisation are then solved numerically (Versteeg & Malalasekera, 1995).

The different approaches that are employed in solvers have already been discussed in the section on discretization methods (Section 3.2.1). The next step after a solution has been obtained is to analyse the results. This is carried out in the post-processor. Tools in post-processors include (Versteeg & Malalasekera, 1995); domain geometry and grid display, vector plots, line and shaded contour plots, 2D and 3D surface plots, particle tracking, etc. These tools are very important in understanding and interpreting the results produced by the solver.

3.3 Model calibration and validation

Calibration is the process of varying the parameters or coefficients of a computational model so that it produces results that are consistent with observed data. This is usually applicable for models with empirical or semi-empirical relationships, which invariably contain parameters that account for unknown variables. Relationships are usually developed for a certain set of conditions. If these relationships are not calibrated when used under different conditions, they are likely to produce unreasonable results. It is therefore important that numerical models are calibrated where necessary against reliable observed data.

According to Schlesinger *et al.* (1979), model validation is the substantiation that a computer model, within its domain of applicability, possesses a satisfactory range of accuracy consistent with the intended application of the model. A model may be valid for one set of conditions and invalid for another (Sargent, 1998). All hydraulic models, therefore, need to be validated to ensure that results obtained are acceptable and consistent. This is achieved by comparing the output variables (variables of interest) from the models with field or experimental data.

3.4 Previous research on modelling of local scour at piers

Olsen & Melaaen (1993) appear to have been amongst the first to carry out computational modelling of local scour around a pier. In their study, a non-orthogonal grid was employed to solve the Navier-Stokes equations for the three dimensional flow domain. The transient terms of the governing equations were ignored, as it was assumed that the flow was steady, and closure was achieved using the k-ε turbulence model. It was assumed that flow was symmetrical about the pier and so only half of the flume was simulated. The flow profile near the bed was represented using Schlichting's (1979) wall laws for rough boundaries. For the sediment transport, a convection-diffusion PDE was used to track the suspended load whilst Van Rijn's (1987) formula was used to obtain the concentration of bed load and the interaction between the bed load and the suspended load. The domain was modified in stages to reflect both erosion and deposition. Once a flow solution had been obtained for a particular stage, erosion and deposition were computed based on sediment continuity. The computed values were then used to modify the bed ensuring that the maximum change in bed elevation was restricted to 10% of the water depth. A new grid was then generated for the domain and the solution process repeated. Since the process was computationally demanding in terms of time, the bed was modified only 10 times. The resulting scour hole was thus not at equilibrium. Even though results from the numerical model compared well with physical model data, the study was inconclusive as to whether or not the procedure would be able to compute the maximum scour depth correctly since the equilibrium scour hole did not develop.

Inspired by Olsen & Malaaen's study, Richardson & Panchang (1998) simulated flow around a bridge pier using the CFD model FLOW-3D on a SUN UNIX workstation with a 32MB RAM. The aim of the study was to assess the reliability of the predicted flow fields in estimating scour and to determine any significant difficulties associated with the process. The 3D Navier-Stokes equations for unsteady flow were solved using both the Prandtl mixing length model and the RNG k-ε model for turbulence modelling. For all the simulations, a non-uniform relatively coarse grid generated within a rectangular coordinate system was employed. The cell sizes were made relatively smaller in the vicinity of the pier and the free surface was tracked using the volume of fluid method. Temporal evolution of the scour hole was not simulated. Rather, three scenarios investigated by Melville & Raudkivi (1977) in the laboratory were modelled; namely the flat bed stage, an intermediate hole stage, and the equilibrium hole stage. Cones were used in the numerical model to represent the shape of the scour holes and sand particles were tracked within the holes using a Langrangian approach. Results from the numerical simulations were compared to the laboratory results and observations. Discrepancies in some of the results were attributed to a number of factors including the level of refinement of the mesh, laboratory difficulties in measuring and computing values, differences in the scour geometries, and differences in the techniques used in constructing the contours of the estimated values. In general, the study indicated a good quantitative and qualitative agreement between the predicted numerical and experimental flow fields. It was also noted that the particles behaved as expected in both holes and was concluded that it would be possible to perform detailed simulations of flow fields near bridge piers for different flow conditions. Thus, it was inferred that the maximum scour depth could be estimated through repeated simulations of scour holes of different sizes.

The study of Olsen & Kjellesvig (1998) also stemmed from Olsen & Malaaen's (1993) work. The research was performed because the cost of computational time had decreased, allowing transient conditions to be modelled and the scour hole to develop to equilibrium. An IBM-370 workstation was used to solve the unsteady RANS equations employing the k-ε model for turbulence closure. The study involved the modelling of a hypothetical case using a relatively coarse adaptive structured non-orthogonal grid. Symmetry boundary conditions were applied and the location of the water surface was calculated by extrapolating the pressure from the inner cells; with the reference pressure level being specified at the downstream boundary where the water level was fixed. For the sediment transport, the bed and suspended loads were determined using Van Rijn's (1987) shear stress formula and a convection-diffusion equation respectively. In computing the critical shear stress, Brook's (1963) formula for slope correction was applied. Realistic patterns in the bed movement were observed when the numerical results were compared with results from physical model tests. It took approximately 9 weeks to calculate 1.5million seconds of computational time. The resulting maximum scour depth was compared to estimates from four empirical formula presented by Chitale (1962), Shen *et al.* (1969), Jain (1981) and Garde *et al.* (1993). It was concluded that the numerically estimated scour depth corresponded well with the estimates from the empirical formula. The numerical model predicted a scour depth of 1.5m whilst the empirical formula estimated 2.2m, 1.9m, 2.2m, and 1.4m respectively.

Yen *et al.* (2001) combined a 3D hydrodynamic model and a scour model to simulate the flow field and bed evolution around a pier. Large eddy simulation of the Navier-Stokes equations was employed for predicting the flow and bed shear stress fields for the flat bed conditions. In order to save simulation time, the flow field was not recomputed as the bed deformed. Instead, the bed shear stress field computed for the flat bed was modified progressively as the bed deformed. It was assumed that the velocity profile near the pier was logarithmic and a Taylor series expansion was applied to the profile to obtain a relationship between the shear and mean velocities before deformation and the shear and mean velocities after the bed had deformed through a given distance. This allowed a relationship between the bed shear stresses before and after deformations to be developed. It was also assumed that scouring took place in the form of bed load and so Van Rijn's (1986) bed load transport formula was used in conjunction with a 2D sediment continuity equation to simulate the evolution of the scour hole. The effects of bed-slope on the critical and effective bed shear stresses were accounted for and scour due of the downflow in front of the pier was estimated using modified submerged vertical jet flow scour equations. At each time step, the increase in scour depth was computed as the sum of the scour depths estimated from the jet flow equations and the bed-load transport formulae. The final scouring equations had constants that needed to be calibrated and this was done using experimental data from Ettema (1980). Lin's (1993) physical model experiments were simulated and there was good agreement between the physical model results and the numerically predicted scour depths.

Ali & Karim (2002) used the general CFD code, FLUENT 4.3, to predict the flow fields around a circular cylinder for rigid beds and scour holes of various sizes. The flow and domain parameters were based on physical experiments performed by Yanmaz & Atinbilek (1990). Evolution of the scour hole was not modelled. A non-uniform structured grid was employed for all the cases and, in each case, the resolution of the grid was refined in the vicinity of the cylinder. The symmetry condition was applied and grid sizes were kept small to avoid grid-

dependent solutions. The flow fields were predicted by solving the RANS equations for unsteady flow. For closure, two variations of the k-ε turbulence model were examined; namely the standard k-ε model and the RNG k-ε model. FLUENT 4.3 did not have a routine to model the free surface and so a rigid-lid approach, in which the water surface was approximated as a frictionless wall, was employed. Results from the two turbulence models were similar. The various stages of the experiments were also physically modelled by Ali & Karim (2002) using plastic moulds coated with sand. Results from these physical models were compared with results produced by FLUENT and it was observed that the numerical model was able to predict some of the essential flow features like the downflow in front of the cylinder, flow separation along the sides of the cylinder, and the horseshoe vortex. It was concluded that the predicted flow fields corresponded well quantitatively with the experimental data. The agreement between the bed shear stress field predicted by FLUENT 4.3 and those computed from the experimental near-bed velocities was however only fair. It was noted that boundary shear stress alone did not account for sediment transport but also, turbulence played a significant role in the scouring process. It was further concluded that perfect results would be difficult to achieve as there were factors that could not be modelled directly using the numerical simulation e.g. the turbulent bursts and the fluctuating water level. Based on the bed shear-stress distributions predicted by FLUENT, Ali & Karim (2002) used the sediment continuity equation to derive an expression for the variation of the scour depth with time. This expression was calibrated and verified against various laboratory and field results.

Armitage & McGahey (2004) simulated open channel flow about a vertical weir, an abutment and two piers using the commercial CFD solver CFX 4.3. The aim of the study was to investigate into the use of the Movability Number criterion for scour prediction. The RANS equations were solved for each case using a relatively coarse grid. Since there was no free surface routine in CFX 4.3, a moving wall approach was used i.e. the free surface was represented by a wall whose velocity was set equal to the expected surface velocity. It was believed that the moving wall boundary condition suppressed the formation of some of the vortices and also raised some local pressures. Of the turbulence models offered by CFX 4.3, it was found that the Low Reynolds Number k-ε and the Standard k-ε models gave the best predictions of the turbulent shear stresses for the two- and three-dimensional flow-fields respectively. FORTRAN subroutines had to be written in order to estimate the bed Movability Numbers. Equation 2.52 was used for slope correction and the scour potential at any point was defined as the difference between the Movability Number at the point and the critical Movability Number. A positive scour potential was considered to indicate the likelihood of scour. Results from the simulations correlated reasonably well with laboratory results on incipient motion and scouring. It was thus concluded that there was potential in the use of the Movability Number approach in CFD for scour prediction.

Salaheldin *et al.* (2004) employed the commercial CFD code FLUENT 5 to simulate turbulent flow around circular piers in clear water. The study evaluated the performance of different turbulence models; namely the standard k-ε model, the RNG k-ε model, the realizable k-ε model and the Reynolds stress models. For each scenario, the RANS equations for unsteady flow were solved using an unstructured grid. The grids were generated in GAMBIT 1.3 and each domain was split into two phases; the first phase representing the water flowing in the channel and the second the region of air on top of the water. It was determined that the initial ratio of the air

depth to the water depth should be one-third or larger to prevent the top boundary from having any effects on the flow. The bed adjacent cells were sized such that the laws of the wall were applicable but computation in the laminar sub-layer was avoided. The volume-of-fluid model was used for the free surface and the cell sizes were made smaller in the region where the surface was expected to improve solution accuracy. Both flat-bed and equilibrium scour conditions were simulated. Upon comparing the predicted velocity and bed-shear stress fields with experimental results, it was judged that the standard and RNG k-ε models could be used to predict the flow field around a pier even though they overestimated the near-bed velocities and the area of scour initiation. The use of the Realizable k-ε model was discouraged as it performed poorly i.e. it resulted in large overestimations of the near-bed velocities and the area of scour initiation. The Reynolds Stress Model performed better than the k-ε models (it gave satisfactory results for the velocity and bed shear stress fields) and was regarded as a better option for scour estimation at piers.

Stemming from the research performed by Armitage & McGahey (2004), Cunninghame (2005) investigated the use of the Unit Stream Power for predicting incipient motion and simulating scour hole development. In the study, the commercial CFD code FLUENT 6.2 was employed to solve the RANS equations for steady flow. The standard k-ε model was used for turbulence closure and the symmetry boundary condition was applied for the pier simulations. The grids used for these simulations were structured in the vertical plane but unstructured in the horizontal plane. Each grid's resolution was refined close to the pier and in the region of the expected free surface. The free surface was modelled using the Volume-of-Fluid method and Armitage's (2002) slope correction factor was applied to the critical unit stream power values for scour estimation. The model predicted all the relevant flow features such as the downflow and bow wave at the upstream face of the pier, flow separation about the sides of the pier, eddying in the lee of the pier, and the initial development of the horse shoe vortex. It was concluded that the estimated region of scour initiation was consistent with theory. Flow in a developed scour hole at a semi-circular abutment (experimental work by Unger & Hager, 2005a) was also simulated. The computed flow patterns appeared realistic but it was noted that the Unit Stream Power model did not give a good estimation of scour at the abutment. Simulation of the bed development for clear-water scour hole evolution at a pier was performed manually and in stages. For a particular stage, the flow field was computed and the scour and deposition calculated manually according to the applied stream power at the bed. The nodes on the mesh representing the bed were then moved vertically (in accordance with the computed scour and deposition) to create a deformed boundary, which was thereupon used to generate a new grid. Once the new grid had been generated, a new flow field was computed and the bed development procedure repeated. Even though the initial movement of the hole was as expected, the procedure was discontinued before an equilibrium scour hole could develop because it was tedious. It was concluded therefore that the procedure had to be automated.

Nagata *et al.* (2005) described the various numerical models for scour prediction developed prior to the year 2000 and commented that although the models were able to predict the general flow features, the results were not entirely satisfactory because of three reasons. The first reason was that some of the models assumed a hydrostatic pressure distribution which was unrealistic within the vicinity of the hydraulic structures where strong downflows and vortex systems were present. Secondly, most of the models assumed that there was local isotropic turbulence (e.g. the standard

k-ε model where the coefficients are supplied as constants). According to Nagata *et al.* (2005), this assumption is not suitable for flow simulations where three dimensional flows are dominant. The last reason was that most bed deformations were modelled using a sediment continuity equation coupled with a bed load transport formula based on shear stress. This approach included the assumption of a local equilibrium of sediment transport over a one-step length scale of particle movement. It was stated that a non-equilibrium condition of sediment transport was dominant around the structures since influencing factors such as the near-bed flow and the local bed slope changed rapidly. A three dimensional model that addressed these issues was hence developed by Nagata *et al.* (2005). For flow prediction, the RANS equations were solved using a non-linear k-ε turbulence model, equivalent to the RNG model, for turbulence closure. A moving grid system was used to ensure that the numerical grids conformed to the bed and water surfaces. The bed deformation model incorporated the effect of non-equilibrium sediment transport by calculating the volume of sediment pickup, the trajectory of sediment motion, and the volume of sediment deposition. A stochastic model was used to predict sediment pickup and deposition, and sediment movement was calculated using a momentum equation for sediment particles. The equations were used to predict the time required for a group of sediment particles to be deposited once they were picked up and the location of deposition. The temporal changes in the bed elevation were obtained from the computed volumes of sediment pickup and deposition. The water surface level was computed using updated pressures for a time step; with the reference level located at the downstream boundary. The grid intervals were varied in the vertical plane in response to the estimated water surface profiles. Due to limitations in computer memory, particle pickup rates were only computed after a number of time steps whereas the momentum and sediment deposition rates were computed for each time step. The ideal procedure would be to track particles being picked up at every time step. Physical model experiments were simulated using the numerical model and, comparing results, it was found that the numerical model reproduced the flow fields and the scour geometries with sufficient accuracy.

3.5 Summary

This section has looked at CFD and the various components of a CFD model. The equations governing fluid flow were presented and the problem of turbulence closure was explained. The different types of grids and turbulence models were described. Concepts behind model calibration and verification were explained and the chapter was concluded with a summary of previous attempts made at modelling local scour around bridge piers.

Chapter 4
Generation of physical data for model validation

It was stated in Chapter 4 that all numerical models have to be validated using reliable physical data. Physical experiments were therefore performed at the hydraulics laboratory of the Civil Engineering department of the University of Cape Town. Results for the experiments were used to assess the performance of the numerical model that was developed in FLUENT. The setup used for the experiments are shown in Figure 4.1. The experiments were carried out in a flume. A false floor was created in the flume using plywood to facilitate the placement of sand only in the test region. A small scale model of a pier was created using a perspex tube. Water was pumped from a sump into a stilling basin from where it flowed into the flume to the test region. From the test region, the water exited the flume over a tail gate and into a drainage structure which led it back into the sump. The pathway of water is illustrated in Section 4.2. The experiments were performed for varying flow conditions. Due to lack of time, only four experiments were performed. Each experiment was run until an equilibrium scour hole developed. The apparatus used and the procedures adopted are described in greater detail in Sections 4.3, 4.4 and 4.5. A summary of the experiments and the results that were obtained are presented in Section 4.6.

4.1 Setup

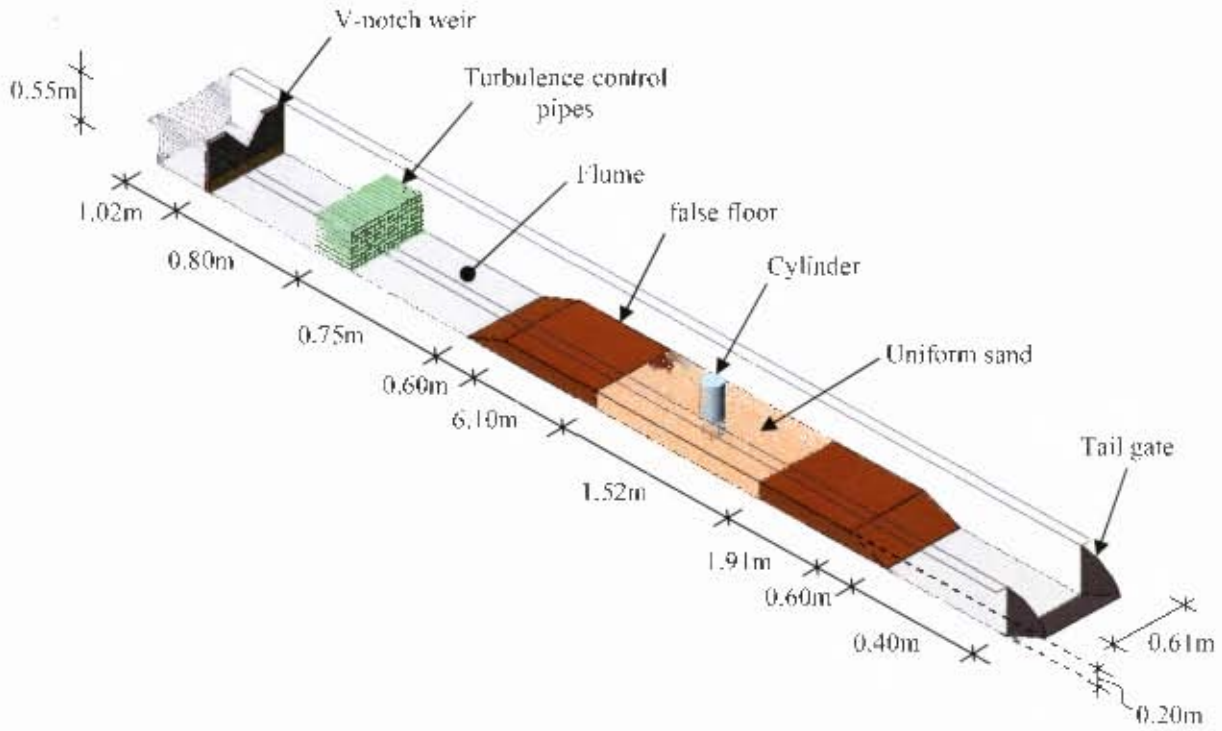

Figure 4-1: Experimental setup (not drawn to scale)

4.2 Pathway of water

The pathway that the water took during the experiments is outlined in steps as follows:

Step 1: The water was pumped from a sump to a stilling tank through transmission pipes.

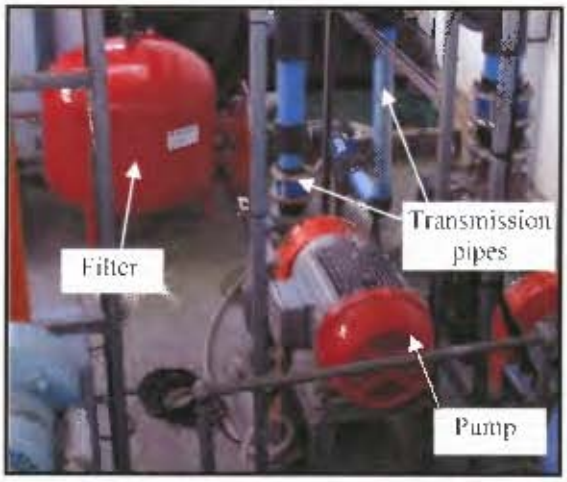

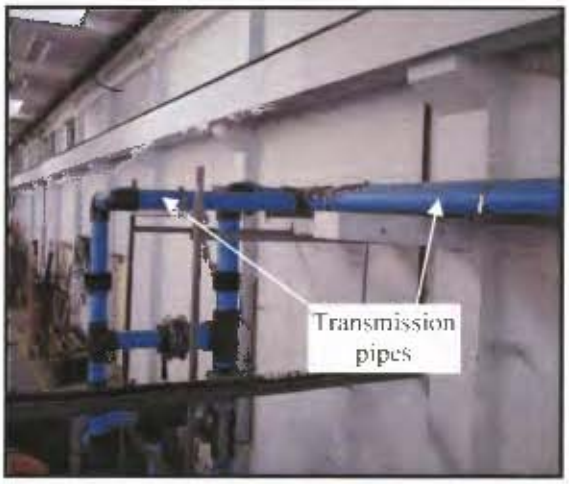

Step 2: The water flowed into the stilling tank first and then into the flume.

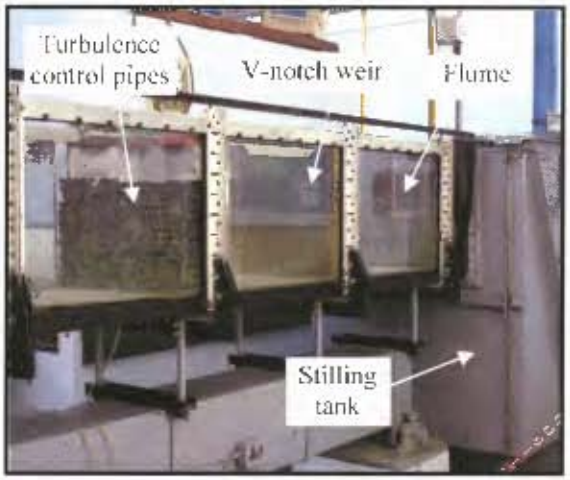

Step 3: The water flowed over the upstream false floor to the test region.

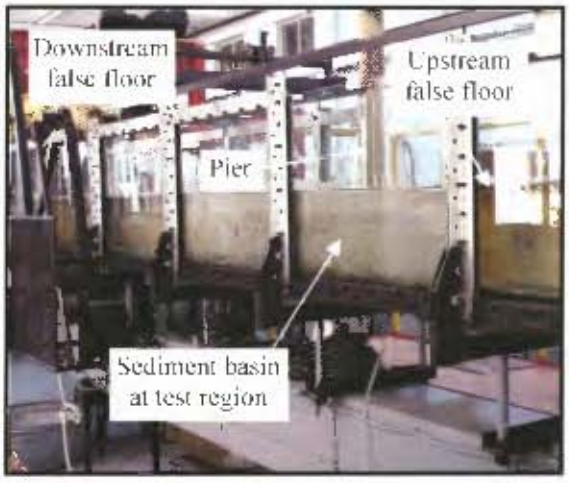

Step 4: The water exited the flume over a tail gate into a return channel which directed it back to the sump.

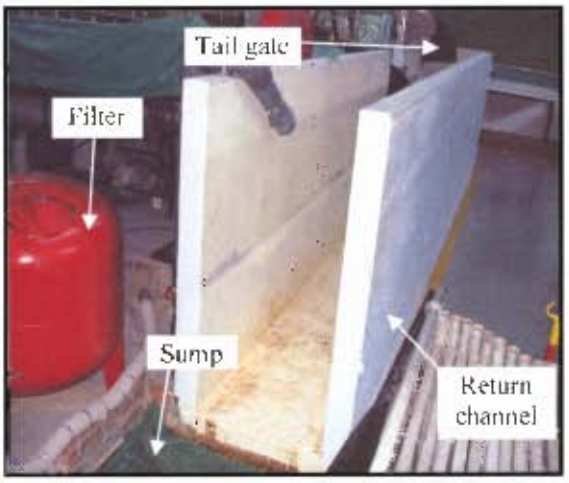

4.3 Flume setup

The experiments were carried out in a straight 13.7m long, 0.61m wide and 0.55m deep tilting flume. The main frame of the flume was made of steel. The side walls were made of smooth transparent glass. A layer of glass was also glued to the bed of the flume. Steel rails were fixed at the top of the flume. A sand spreader was placed on the rails in a manner such that it could glide along the length of the flume. The bed slope of the flume was maintained at 0° for all the experiments. Attached to the upstream end of the flume was a 2.12m × 1.2m × 1.3m stilling tank. Water from a sump was pumped into the tank, from whence it flowed into flume. Valves, fixed at various points on the supply line from the pump to the tank, were used to regulate the flow. A tail gate was connected at the downstream end of the flume. This gate was also used to control flow conditions in the flume. Water flowing out of the flume was directed back into the sump via a return channel.

4.3.1 Scour region

Two false floors were placed on the bed of the flume to create a recess in the region where scouring was expected to occur under turbulent flow conditions. The upstream false floor was lined with a thin layer of sand. This was done to ensure an appropriate upstream bed roughness, which would give rise to the required flow conditions at the pier. The downstream false floor ensured that the water surface level throughout the test region remained fairly constant. Unlike the upstream false floor, it was not coated with sand. The recess was 1.52m long × 0.61m wide × 0.20m deep as it was estimated that the maximum scour depth would not exceed 0.20m. The pier was represented by a cylindrical tube, which made of perspex glass. This cylinder was placed at the centre of the recess and glued to the glass at the bottom of the flume. Sand was then placed in the recess, around the cylinder, to represent the river bed. The recess was filled until the sand surface was flush with the thin layer of sand that was glued onto the upstream false floor

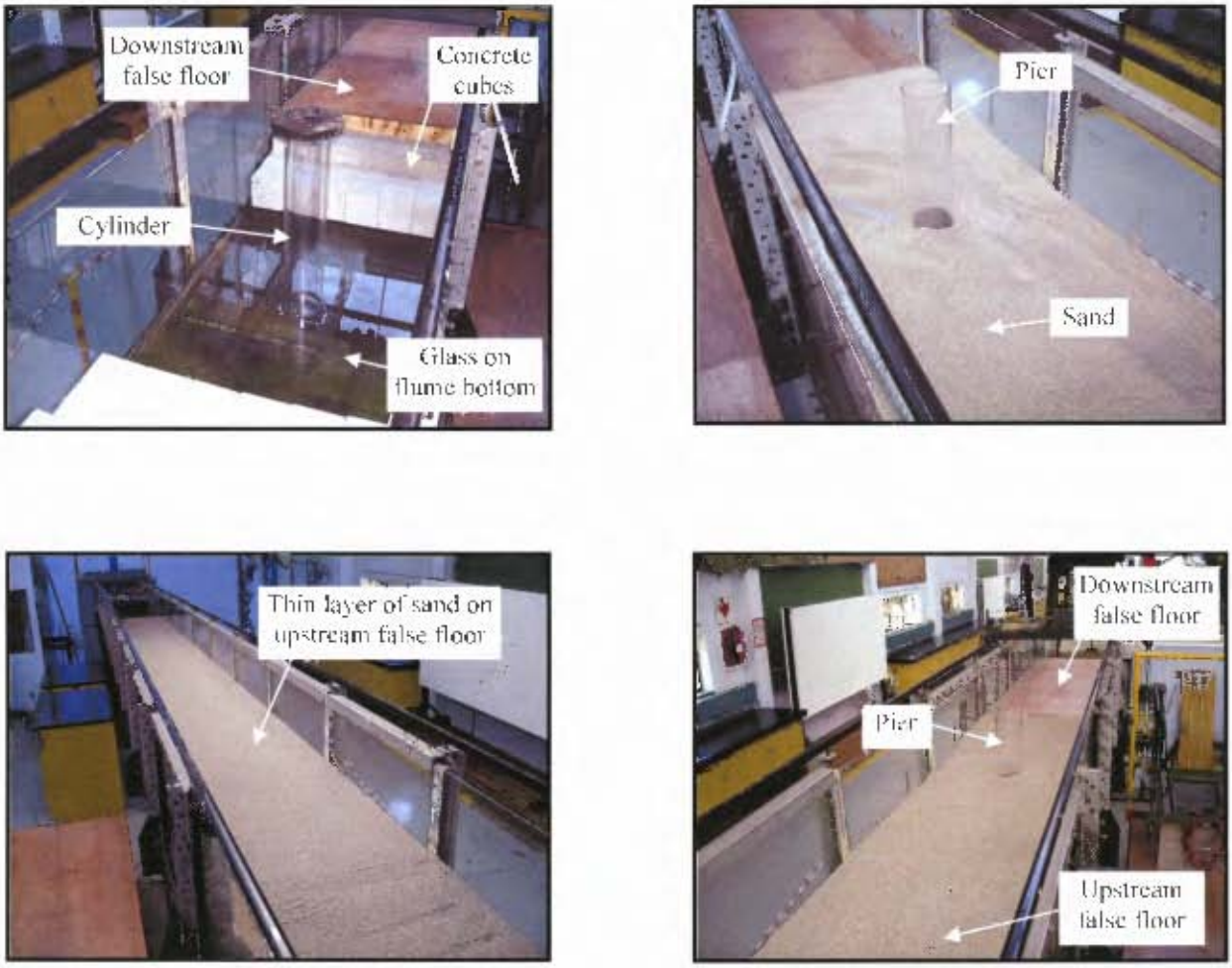

Figure 4-2: Snapshots of scour region and platform setup

4.3.2 Contamination and turbulence control

Water from the sump was passed through a sand filter. This served two purposes. The main purpose was to filter out any contaminants that were in the water. The sand filter also served as a form of regulator which ensured that the flow of water through the pipes into the stilling tank was fairly steady. Water flowing into the flume from stilling tank first had to go over a v-notch weir for measurement purposes. A turbulence control structure was placed just downstream of the weir. The structure consisted of 20mm diameter pipes arranged in layers across the width of the flume. Each pipe was approximately 150mm long. Weights were placed on the top layer to hold the pipes in place. The pipes were to ensure that eddies generated by the flow over the weir were controlled and the streamlines of flow approaching the test region were as parallel as possible.

Figure 4-3: Contamination control

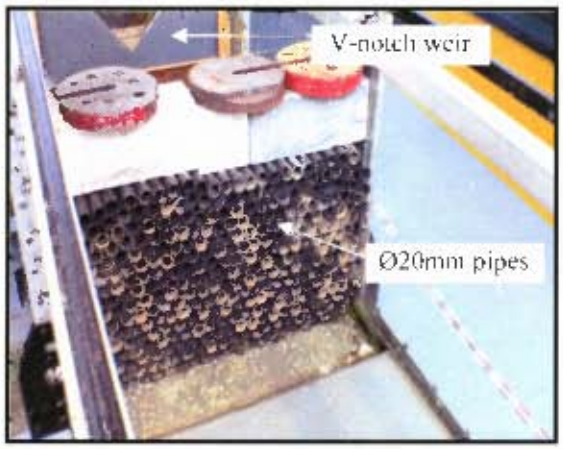

Figure 4-4: Turbulence control structure

A small weir was constructed in the return channel that led water from the flume back into the sump. The purpose of this weir was to allow sediment that had been transported from the test region in the flume to settle in the drainage structure before the water entered the sump. This would serve to filter the water and also permit the re-use of sediment for subsequent experiments. The weir was constructed using concrete cubes. The cubes were arranged so that there were spaces within the structure through which the water could flow. The structure was wrapped in shade cloth. Additional weights had to be placed on the structure to prevent the pressure forces from pushing it down the channel.

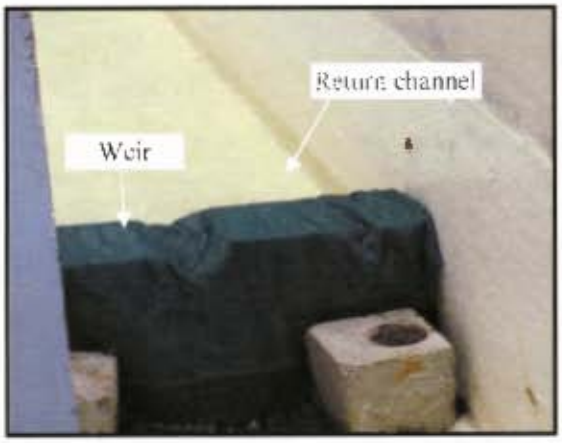

Figure 4-5: Weir in return channel

4.4 Measuring equipment

4.4.1 Flow measuring equipment

Flow rate measurements were carried out using an electronic flow rate meter and a v-notch weir. For each experiment, the flow rate, Q, over the v-notch weir was determined using the following Equation (Lyons, 2003):

$$Q = 1.37 h_w^{5/2} \tag{4.1}$$

where h_w is the head of water above the weir.

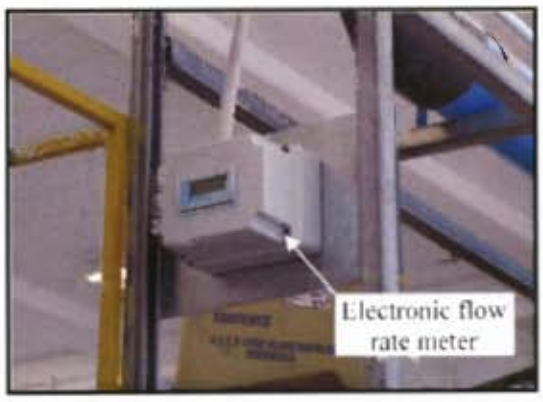

Figure 4-6: Flow measuring devices

4.4.2 Scour measuring equipment

It was imperative that there were no external disturbances to the flow during the experiments. A laser pointer was used in conjunction with a rule to measure the extents of the scour hole that developed. The laser pointer was attached to a rig, which could glide over the rails on the flume (see Figure 4-7). The rig permitted the laser pointer to be moved in both horizontal and vertical directions. The extents were measured at 0°, 30°, 60° & 90° to the approaching flow respectively (See Figure 4-8). Care was taken to ensure that the laser pointer was always vertical and the readings were taken at locations where the water surface was fairly horizontal. This was done to prevent refraction of the laser beam. There was no distinct line indicating the extent of the scour hole. Location of the extents was thus based on the experimenter's judgement and so yielded only approximate values. Scales were stuck onto the inside of the cylinder at angles the same as those above. A periscope was used to take readings of the scour depths from within the cylinder. The periscope was made out of two 90mm × 50mm mirrors and an 80mm diameter, 1m long *poster tube*. This is shown in the Figure 4-9. Once the experiment was stopped and the water had been allowed to drain, a depth gauge vernier was used to determine the maximum scour depth.

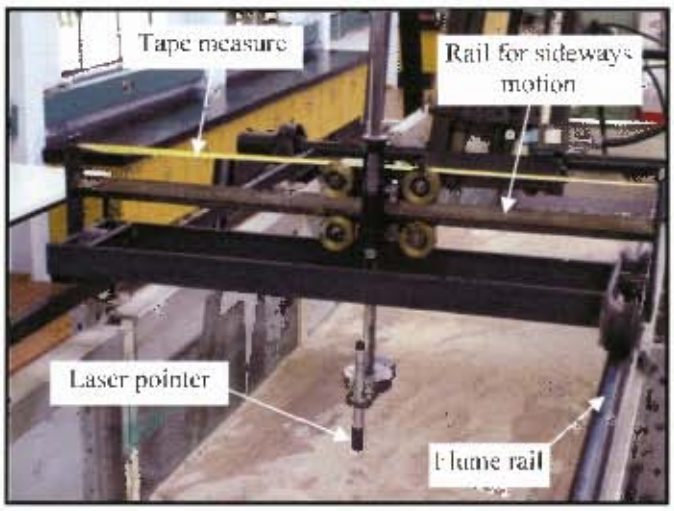

Figure 4-7: Laser pointer rig

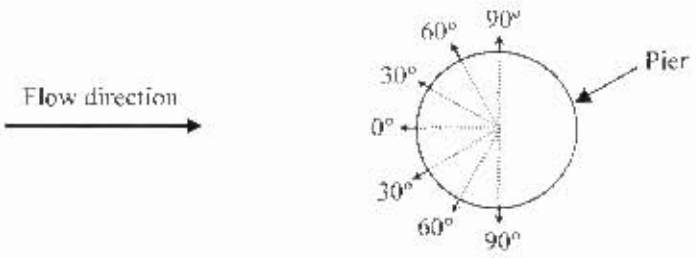

Figure 4-8: Angles at which the extents of the scour hole were measured

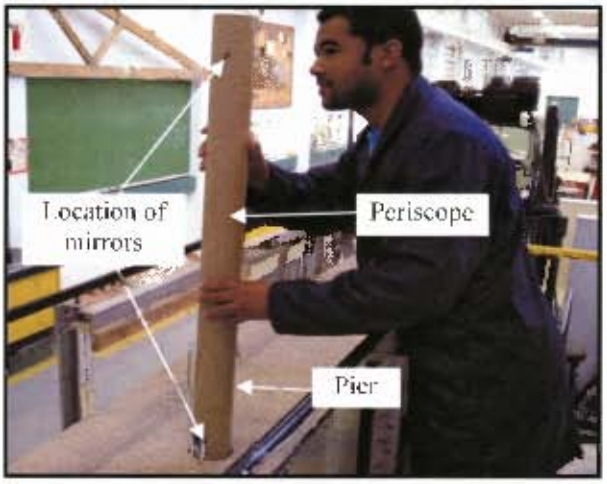

Figure 4-9: Periscope for scour depth measurement

4.5 Experimental methods

4.5.1 False floors

The false floors were created using plywood to allow for the construction of the sediment basin. Both floors were at the same height. The height was selected to allow for appropriate scour depths to fully develop. A ramp, with an approximate slope of 1:3, was fixed to the upstream end of the upstream floor and the flume bed. This was to provide a smooth transition of the water from the flume bed onto the floor. A similar ramp was placed at the downstream end of the downstream floor to ensure that the water exited smoothly from the test region without affecting the flow depth. The length of the upstream floor was 6.1m and that of the downstream floor was 1.91m. These lengths were to ensure the proper development of the required flow profile at the test region.

The false floors were fixed to and supported by hollow substructures. When the apparatus was initially run, some of the water flowed over floors whilst some filled the spaces within the substructure. Air was thus trapped just underneath the floors. As the water level beneath the upstream floor rose, the air pressure caused it to float and move out of place. It was thus decided that holes be drilled into the floor to allow the trapped air to escape. In the subsequent run, the trapped air was able to escape but unfortunately the floor was still buoyant. It was then decided that the region beneath the floor be completely sealed of using silicone. The idea was to prevent water from entering the region beneath the floor so that the water pressure above would hold it in place. The problem with this approach was that water still found its way beneath the floor through very small crevices that were exposed in the silicone. The rate of influx of water into the region was however much slower and the trapped air managed to escape through the same crevices. The silicone held the floor in place as the water level beneath it rose and eventually the region below was completely filled with water. This last setup was thus used for the experiments as it was acknowledged that it would be extremely difficult to completely prevent water from flowing into the region within the substructure.

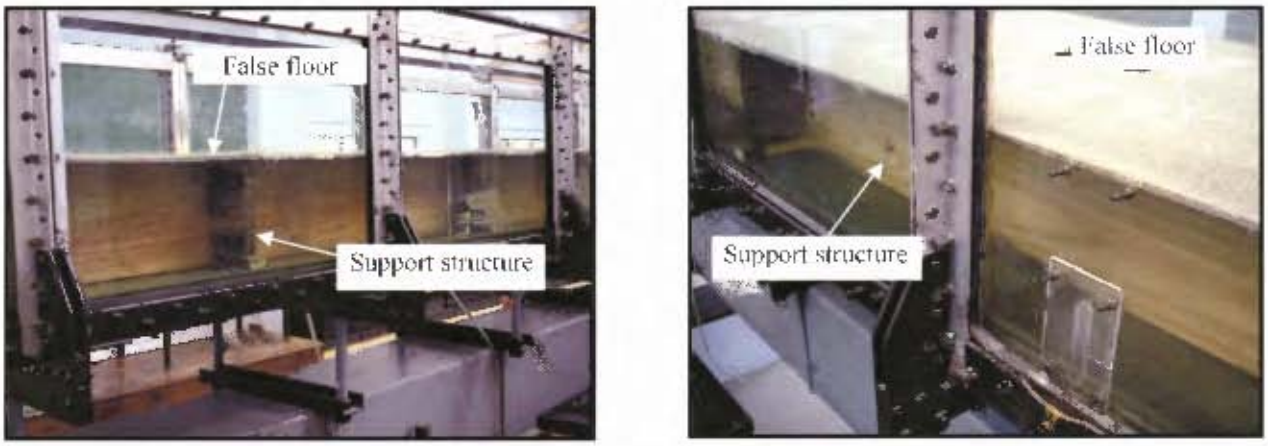

Figure 4-10: Upstream false floor indicating the support structure

4.5.2 Spreading sand

The sand used for the experiments had to be uniform, cohesionless and non-ripple forming. According to Melville (1997), sand is considered to be uniform when the geometric standard deviation is less than 1.3. The sand is also non-ripple forming when the median diameter is greater than 0.7mm. Quartzitic sand was used for the experiments. The sand was sieved through two sieves of sizes 0.8 and 0.65mm respectively. Sand retained on the 0.65mm sieve was used for the experiments. Particle sizes thus ranged between 0.65 to 0.8mm with an average of 0.725mm (Chien & Wan, 1999). The approach employed by Lyons (2003) to determine whether or not the sand was uniform and non-ripple forming was employed. This is a conservative approach which assumes that the limits 0.65 and 0.8mm correspond to $d_{15.9}$ and $d_{84.1}$ respectively. A geometric standard deviation of 1.11 was obtained when Equation 2.21 was applied, indicating the sand was uniform. Also, Equation 2.19 yielded a median diameter of 0.725mm which implied that the sand would not form ripples.

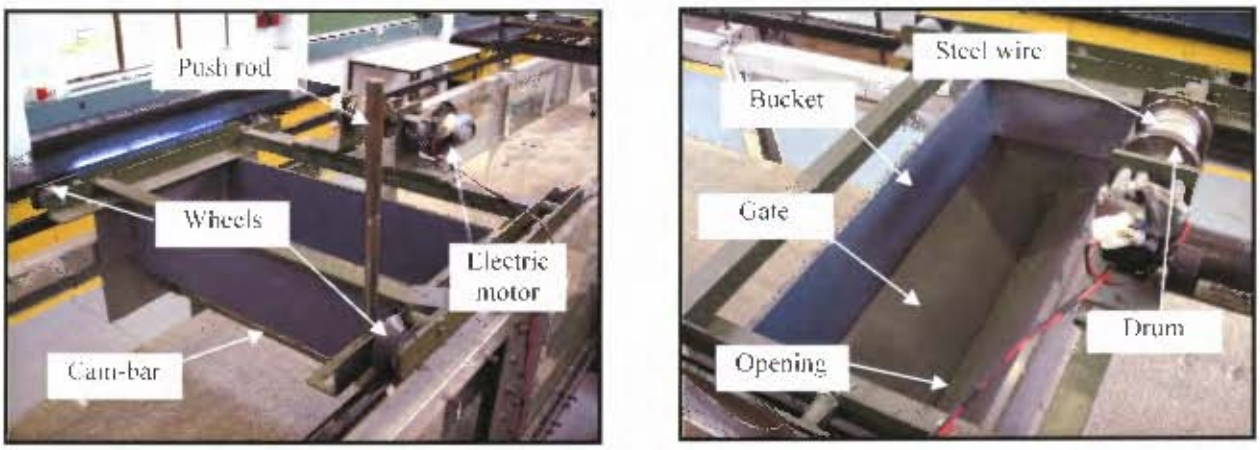

Figure 4-11: Sand spreader

It was required that the roughness of the upstream floor be the same as that in the test region. A uniform layer of sand was glued to the top of the floor. The sand used was the same as that used for the tests. A sand spreader designed by Lyons (2003) was employed for this activity. The sand spreader was made up of a PVC bucket which had metal sides connected to a moveable frame. This moveable frame had wheels which permitted it to move along the rails on the flume. The bucket had a spring-loaded gate that was controlled with a push rod connected to a cam-bar. The gate could open to a maximum of 2.8mm.

Movement of the spreader over the rails was controlled by a reversible 12V DC motor. The motor provided a maximum speed of 64rpm at 12V. The motor was controlled by a stabilized variable dual DC power supply which could provide 0-30V at 3A. Connected to the motor was a 50mm drum. Attached to this drum was one end of a steel wire which had a total length of approximately 7m when completely unwound. The other end of the wire was attached to a bracket on the flume located a distance away from the spreader. The winding action of the steel wire around the drum due to the rotation of the motor gave rise to the motion of the spreader in the direction of the bracket. Once the spreader got to the bracket, the wire had to be unwound (by reversing the polarity of the power supply) and the spreader rolled back manually.

The potential difference was varied and various speeds of the spreader were considered for spreading the sand. After a couple of trial spreader runs, it was determined that a power supply of 10V at 3A would provide the required thickness of sand when the spreader was run twice. Once this was determined, the surface of the upstream false floor was coated with a layer of varnish and the sand spread over it immediately to the required thickness. The layer of varnish was thick enough for the sand to settle in. The sand spreading was performed on a Friday and so the varnish was left to dry over the weekend.

The sand basin also had to be filled with sand. In order to conserve sand, the regions in the basin where scour was not expected to occur were filled with concrete cubes. The basin was then filled until the level of the sand surface was flush with the top of the thin layer of sand on the upstream false floor. A horizontal line was drawn along the sides of the flume to help identify the required level of sand. The top of the sand was levelled using a rectangular board first and then the bottom of a scoop (see Figure 4-12) until the surface was smooth and horizontal. This proved to be an arduous and time-consuming exercise. The level of the surface was checked using a builder's level and a depth gauge vernier. Care was taken not to disturb the surface.

Figure 4-12: Placement and levelling of sand

4.5.3 Establishing flow

The scour experiments were carried out once the setup was ready. The starting of the pump marked the beginning of each experiment. The flow entering the flume was regulated with a gate valve. Initially, the tail gate was raised and water was allowed into the flume at a very small flow rate. This was done to prevent any significant sediment transport and the bed from rippling. The water level was allowed to rise slowly until it was about 10 to 20mm lower than the required depth. The valve was then adjusted quickly until the required flow rate was showing on the

electronic flow meter. The reading on the meter fluctuated by about ±0.4l/s and so was only used as a guide. The final flow rate was determined from the head of water over the v-notch weir which remained constant. Once water was flowing through the flume at the required rate, the tail gate was adjusted to maintain the flow at the required depth. Achieving this took about a minute. Scouring normally started before the desired flow conditions were attained. As the scour hole was very small in the initial stages, it was judged that this would not affect the dimensions of the equilibrium scour hole that would develop eventually.

4.5.4 Taking measurements

Measurements were taken of the scour depth and the extents of the scour hole as it progressed. The times at which measurements were taken were dependent on the rate at which the scour hole advanced. As explained in Section 3.3.4.2, the scour hole progresses rapidly in the initial stages and its growth slows down with time. Readings were taken at short intervals in the initial stages. These were spaced out as time progressed. Typically, readings were taken at 5, 10, 15, 30, 45 and 60 minutes in the first hour of the experiment. Readings were spaced out to 30minute intervals afterward. This interval was increased as the experiment progressed, with the increase being dependent on the rate of scour hole evolution. The clear water scour hole approaches equilibrium asymptotically and so it was difficult to know when to stop an experiment. It was thus necessary to define a point at which an equilibrium hole was deemed to have been reached. The approach adopted by Melville & Chiew (1999) was employed. In this approach, the time to equilibrium was defined as the time at which the scour hole developed to a depth at which the rate of increase of scour did not exceed 5% of the pier diameter in any 24hr period i.e.

$$\frac{d(d_{se})}{dt} \leqslant \frac{0.05 b_p}{24} \tag{4.2}$$

where d_{se} is the equilibrium scour depth in mm, t is the time in hours and b_p is the pier diameter in mm. The diameter of the pier that was used for the experiments was 100mm. The experiments were therefore stopped (equilibrium was deemed to have been reached) when the increase in the scour depth was less than 5mm within any 24hr period. The times to equilibrium for the experiments ranged between 40 to 77hrs. It was noted during the experiments that the maximum scour depth occurred a short distance away from the cylinder. The periscope readings however gave the scour depth right next to the cylinder. Measurements taken at the end of the experiments indicated that the average percentage difference between the read values and the actual maximum depths was about 3%.

4.6 Criteria for flow selection

Three criteria were used to select the flow rates and depths that would be modelled. The criteria were developed based on considerations of the local Reynolds number, the particle Reynolds number and the physical space available for the equilibrium scour depth. These considerations and the criteria are presented in the following paragraphs.

According to French (1998), fully developed turbulent flows occur when $Re_x > 10^6$ (See Section 2.2). Since the experiments were being performed for fully developed turbulent flows, the mean approach velocity, U, had to be (from $Re_x > 10^6$ and Equation 2.8):

$$U > \frac{10^6 \times \nu}{x} \tag{4.3}$$

Taking x as the length of the platform (x = 6.1m) and substituting ν with 10^{-6}m²/s, the **first criterion** for flow selection was obtained as follows:

$$U = \frac{Q}{A} = \frac{Q}{0.61h} > 0.164 \tag{4.4}$$

where Q is the flow rate, A is the cross-sectional area of flow and h is the depth of flow.

The particle Reynolds number had to be considered for the experiments as well. For turbulent beds, the criterion developed by Armitage & McGahey (2003) requires that:

$$\frac{u_* k_s}{\nu} > 6.23 \tag{4.5}$$

Substituting Equations 2.4 and 2.11 into Equation 4.5 and multiplying both sides by ν / k_s results in:

$$\sqrt{ghS} > \frac{6.23\nu}{k_s} \tag{4.6}$$

For uniform flows, the bed slope, S, may be replaced with the friction slope, S_f. The square root of the slope, $S^{1/2}$, may be obtained from Manning's equation, as follows:

$$S^{\frac{1}{2}} = \frac{nQp^{\frac{2}{3}}}{A^{\frac{5}{3}}} \tag{4.7}$$

Where p is the wetted perimeter and n is Manning's coefficient. Since the side of the walls and the bed are of different roughness, the equivalent Manning's coefficient may be determined from (Chow, 1959):

$$n = \frac{\left(B_c n_b^{3/2} + 2h n_g^{3/2}\right)^{2/3}}{\left(B_c + 2h\right)^{2/3}} \tag{4.8}$$

where n_b and n_g are the Manning's roughness for the bed and the side walls respectively and B_c is the channel width. For the glass side walls, n_g was assumed to be 0.010 (Armitage, 2002). The value for n_b was obtained from Strickler's relationship for shallow flows (Nalluri & Featherstone, 2001):

$$n_b = \frac{k_s^{1/6}}{26} = \frac{(0.000725)^{1/6}}{26} = 0.012 \tag{4.9}$$

Substituting Equations 4.7 and 4.8 into Equation 4.6 yields the following condition:

$$\frac{Q\left(B_c n_b^{3/2} + 2hn_g^{3/2}\right)^{2/3}}{B_c^{5/3} h^{7/6}} > \frac{6.23\nu}{k_s g^{1/2}} \tag{4.10}$$

Substituting the appropriate values and simplifying resulted in the **second criterion**:

$$\frac{Q(0.001 + 0.002h)^{2/3}}{h^{\frac{7}{6}}} > 0.0012 \tag{4.11}$$

The flow rates and depths that were chosen for the experiments had to satisfy both Equations 5.4 and 5.11. Also, the flow conditions had to be such that the scour hole was not greater than 0.2m. This constraint was due to the amount of space that was available in the recess (the depth of the recess). The **third criterion** was therefore:

$$d_s < 0.2m \tag{4.12}$$

The equation presented by Melville and Coleman (2000) was used as a guide in the estimation of d_s for the selected flows. This equation is as follows:

$$d_s = K_h K_I K_d K_t \tag{4.13}$$

Where the K's are empirical expressions accounting for the various influences on scour depth. K_h accounts for flow shallowness, which represents the effects of the depth of flow in relation to the pier width; K_I accounts for flow intensity, which represents the effects of the mean flow velocity in relation to the threshold velocity; K_d accounts for the effects of sediment size or coarseness; and K_t accounts for the time effects. For the equilibrium scour depth, $K_t = 1$. The other factors were determined as follows (Melville & Coleman, 2000):

For $U/U_c<1$,

$$K_I = U/U_c \tag{4.14}$$

For $0.7 < B_c / h < 7$,

$$K_h = 2(hB_c)^{1/2} \tag{4.16}$$

For $B /d_{50} > 25$,

$$K_d = 1 \tag{4.17}$$

Table 4-1 shows the flows that were modelled and the values that were obtained when Equations 4.4, 4.11 and 4.12 were applied.

Table 4-1: Flow rates and mean flow depths for modelled flows

Experiment	Q (m^3/s)	h (m)	Criteria for flow selection		
			$\frac{Q}{0.61h} > 0.164$	$\frac{Q(0.001+0.002h)^{2/3}}{h^{\frac{7}{6}}} > 0.0012$	$d_s < 0.2$
1	0.0114	0.095	0.196	0.00200	0.116
2	0.0104	0.085	0.200	0.00205	0.115
3	0.0114	0.075	0.250	0.00257	0.138
4	0.0125	0.076	0.270	0.00278	0.148

4.7 Summary of experiments

A summary of the experiments that were undertaken is presented in Table 4-2.

Table 4-2: Summary of physical experiments

Experiment No.	Q(m³/s)	h(m)	U(m/s)	d_{50} (mm)	n	S_f	u_* (m/s)	U_c(m/s)	t_e(hrs)	d_{se}(mm)
1	0.0114	0.095	0.196	0.725	0.011541	5.73×10^{-7}	0.00073	0.3202	77	68
2	0.0104	0.085	0.200	0.725	0.011579	5.39×10^{-7}	0.00067	0.3148	56	61
3	0.0114	0.075	0.250	0.725	0.011619	7.44×10^{-7}	0.00074	0.3087	40	104
4	0.0125	0.076	0.270	0.725	0.011615	8.81×10^{-7}	0.00081	0.3093	42	113

4.8 Scour hole evolution

Figures 4-13 & 4-14 show scour depth results obtained from the experiments. They indicate the variation of the dimensionless scour depth with the dimensionless time. These values have been compared to the profiles suggested by Ahmed (1995) and Melville & Chiew (1999) (Equations 2.55 & 2.56), which are represented by A and MC respectively.

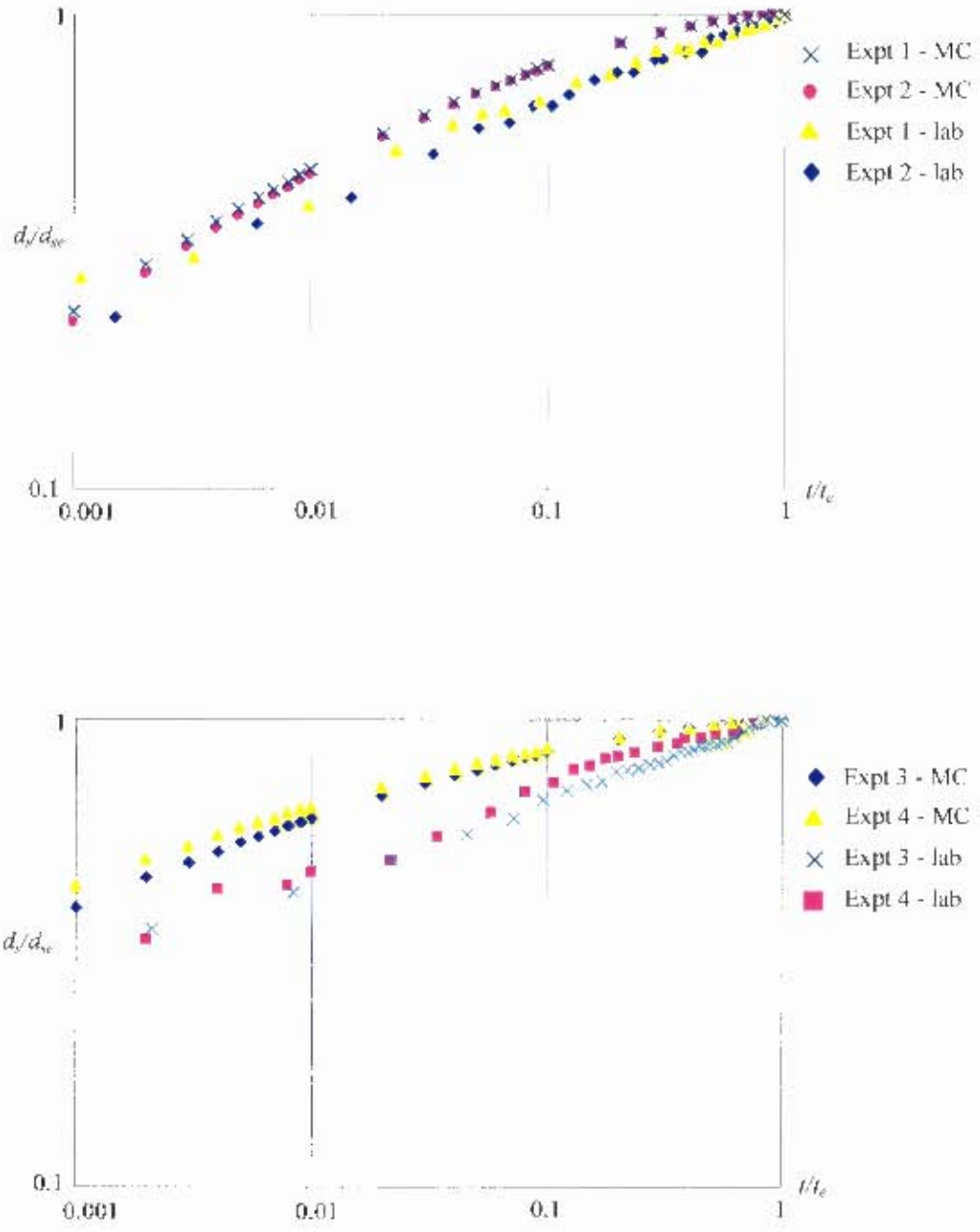

Figure 4-13: Scour results vrs Melville & Chiew's empirical formula

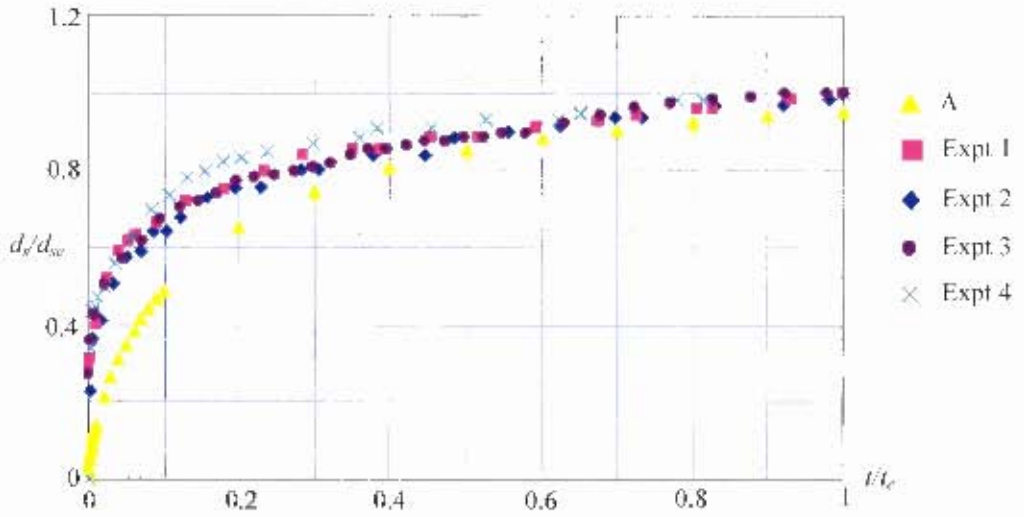

Figure 4-14: Scour results vrs Ahmed's empirical formula

It can be noted from the figures that the scour profiles generally follow the same pattern as those suggested by the empirical formulae. The profiles are also satisfactorily close to the suggested ones. Despite the closeness, the profiles are consistently lower than those suggested by Melville & Chiew (1999) and are consistently higher than the curve suggested by Ahmed (1995), which does not take flow intensity into account. Both the Ahmed (1995) and Melville & Chiew (1999) relationships were obtained from a wide variety of data with a fair amount of scatter. There could therefore be various reasons for the differences. These reasons could vary from experimental procedures, sediment sizes, flow intensity ratios, etc. It could also be that the suggested equations do not account for other scour dependent factors. In general, however, the plots indicate that the results obtained from the experiments are good enough for use in the validation of the numerical model.

4.9 Error estimation

It was mentioned in Section 4.4.1 that the flow rate for each experiment was determined using an electronic flow rate meter and a v-notch weir. The reading on the electronic flow meter continually fluctuated by about ±0.4l/s. It was thus only used as a guide in approximately establishing the flow conditions that were required. The overflow height of water above the v-notch remained constant throughout each experiment and so was used to estimate the flow rate through the flume. The water surface level had to be read of a chart on the weir. The readings were taken from the side of the flume trying as much as possible to avoid parallax. It is estimated that any errors in the reading of the overflow height would be to the order of 1mm. The estimated overflow heights for the experiments ranged between 142 – 153mm. This implies that the error range in estimating the overflow height was 0.65 – 0.70 %. Since the flow rate is

proportional to the overflow height raised to the power 2.5 (See Equation 4.1), the error range in flow rate estimation was estimated to be between 1.63 – 1.75%.

Mean flow depth measurements were taken using a rule along the sides of the flume. It is estimated that the error in taking the measurements were also to the order of 1mm. The flow depths ranged from 75 – 95mm implying that the percentage error ranged between 1.1 – 1.3%. Using the maximum percentage errors, the total error estimated in determining the mean flow velocity was 2.05%.

Measurements of the scour depth were taken from within the cylinder. It was noticed after each experiment that the maximum scour depth did not occur right by the cylinder but rather it occurred a short distance away from the cylinder. The difference in the read maximum scour depths and the actual maximum scour depths was roughly 2mm. The scour depths that were read ranged from 68mm – 113mm. The percentage errors for the maximum scour depth readings therefore ranged from 1.8% – 2.9%.

The extents of the scour hole were estimated using the laser pointer. Care had to be taken to ensure that refraction was prevented. Values read at the end of every experiment before and after the flow was stopped predicted roughly the same value. The location of the extents was selected based on the experimenter's judgement and the error is estimated to be to the order of 2mm. In addition, the distance from the pier to the extent was determined using a rule and so an additional error of 1mm was estimated. The total error in determining the extent of the scour hole at any particular time was therefore estimated to be in the order of 3mm.

Chapter 5
Procedures adopted for numerical modelling

5.1 Current research

This section outlines the numerical methodologies that were adopted for the research. The current research stems from those carried out by Armitage & McGahey (2004) and Cunninghame (2005). Results from these were encouraging enough to suggest that the Movability Number approach could be used to predict the maximum scour depth in clear-water scour with a fair degree of accuracy. The current research was therefore based on the Movability Number approach. It focused on the automation and improvement of the bed adjustment routine that had been developed. All the simulations were performed using an Intel P4 chip with a clock speed of 2.8GHz and 2GB RAM. The procedures adopted for the research are described in the following sections. These procedures, which include grid generation, boundary conditions specified, definition of fluid properties, models employed, solvers controls etc, are crucial as they dictate the level of accuracy of the solution.

5.1.1 Computational grids

The grids used for the simulations were generated in GAMBIT 2.2.3. Since the flow about a cylinder is thought to be fairly symmetrical, only half of the domain was modelled. The computational domain was divided into two main sub domains, with each sub domain representing an expected phase of fluid (i.e. air or water). The domain boundary representing the bed was divided into two zones; namely a deforming zone and a non-deforming zone. The deforming zone was the zone close to the pier where scouring was expected to take place. This zone would be modified to reflect scour as the simulations progressed. Similarly, the sub domain representing water was further divided into two regions; a deforming region and a non-deforming region. This was necessary as it was expected that the section of the grid within the vicinity of the pier and near the bed would have to be modified as the simulation progressed to conform to the deforming bed. The general layout of the domain is shown in Figure 5-1.

Unstructured grids were employed for all the simulations; each grid was unstructured in the horizontal plane but structured in the vertical plane. These are shown in Figure 5-2. The vertical dimensions of the domain were selected such that the expected ratio of the initial depth of air to the initial depth of water was one-third or greater. Salaheldin *et al.* (2004) found that this ratio was necessary to prevent the boundary at the top of the domain from having an effect on the flow. Cunninghame (2003), found that mixing of air and water occurred in long domains when the air occupied less than two-third of the domain depth. Different vertical dimensions were tried to assess if there would be any differences in the solutions. Cell sizes of the grid were kept small to avoid grid dependent solutions. The cell sizes of the bed-adjacent cells were selected based on the type of wall treatment that was used for the simulations. The sizes were specified such that the points at which the flow variables were determined (cell centres) fell within the range $11.225 < y^+ < 300$.

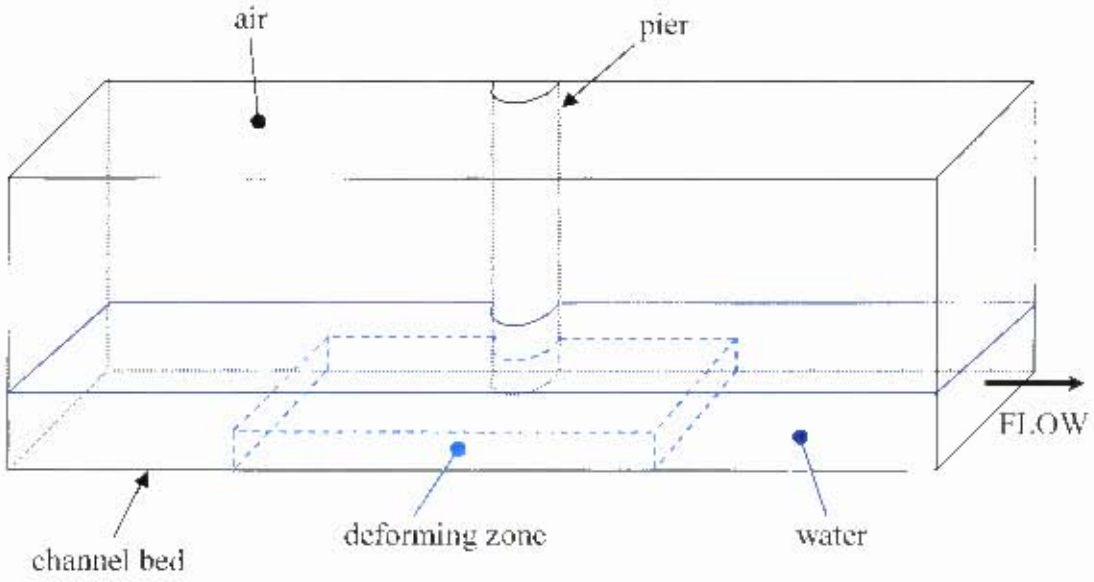

Figure 5-1: Layout of computational domain

According to Fluent (2005), the logarithmic law for mean velocity is valid for the range $30 < y^+ < 300$ for equilibrium turbulent boundaries. In FLUENT 6.2, however, the logarithmic law is applied when $y^+ > 11.225$. Cell sizes were thus selected so that their centres would be close to but greater than 11.225. This was necessary since turbulent boundary flows were being modelled. It would be pointless to perform computations in the laminar sub-layer ($y^+ < 11.225$). The grid was fined up close to the pier, the bed and in the region of the expected free surface. This was done so that the rapidly changing velocity gradients and flow features could be adequately resolved. The grid was generated in a manner such that it was roughly aligned with the expected flow. This was to limit false diffusion, a common numerical error that occurs when the flow is not aligned with the grid. False diffusion reduces with reducing cell sizes. Although the expected changes in the bed elevation were small enough to suggest a very fine vertical mesh in the region of the surface, the level of refinement was restricted by the aspect ratio of the cells. Care had to be taken to prevent very high aspect ratios (excessive skewness) as this could lead to problems with solution convergence. A fine vertical mesh would imply that the mesh be fine in the horizontal plane as well. This would, however, lead to a domain with millions of cells that would be computationally expensive to solve.

Ali & Karim (2002) placed the inlet boundary and the outflow boundary at 3 and 6 times the pier radius respectively. Sarker (1998) noted that flow remained undisturbed approximately 12 times the pier diameter downstream. Salaheldin *et al.* (2004) therefore placed the downstream outflow based on this constraint and the upstream inlet at a distance which was sufficient enough for the flow to become fully developed. For the current simulations, the inlet and outlet boundaries were placed at 15 times the pier diameter upstream and downstream respectively. The approximate flow profiles of the developed flows were specified at both the inlet and the outlet. The position of the outlet boundary was thus in accordance with Sarker's (1998) observation. Also, it was not necessary to place the inlet at a further distance upstream as the specified flow profile was

considered to be for the developed flow. During the simulations it was found that this arrangement resulted in the correct prediction of the mean flow depth at the test region.

In developing each grid, an unstructured face mesh was first created in the horizontal plane. This mesh was then extruded in the vertical direction to create volume meshes with prismatic or hexahedral cells. An example of the grids used is shown in Figure 5-2.

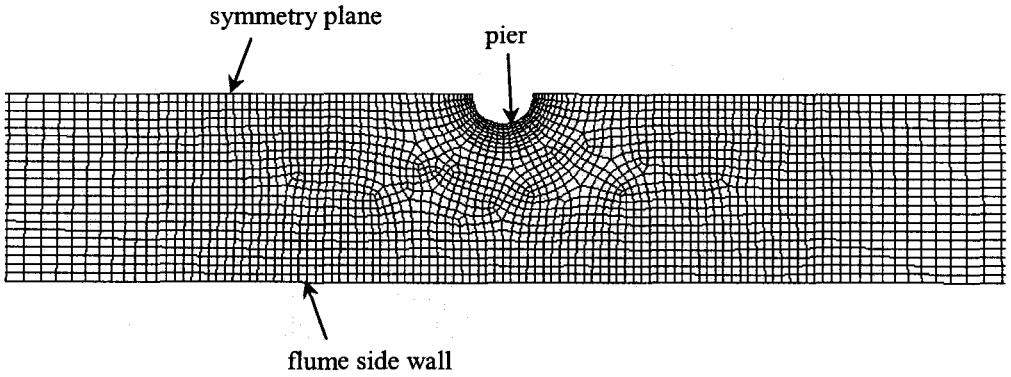

Figure 5-2a: Horizonal section through computational grid

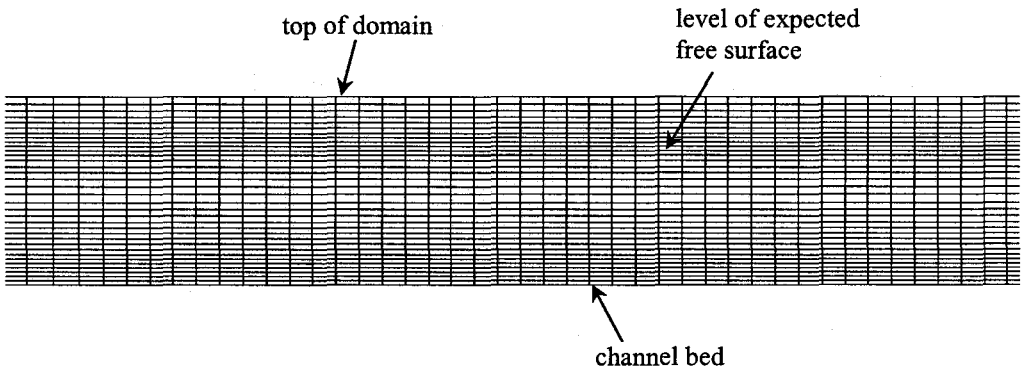

Figure 5.2b: Vertical section through computational grid

5.1.2 Numerical solutions

The CFD solver, FLUENT 6.2 (double precision segregated solver) was employed for all the numerical simulations. FLUENT is a finite volume based program written in the C language and is generally employed in modelling fluid flow and heat transfer in complex geometries. FLUENT offers interactive menu-driven interfaces which aid the user in accessing the necessary functions and in post-processing. The functions used, the specifications made and procedures that were employed in FLUENT in order to obtain the solutions are described hereafter. Most of the approaches used were similar to those employed by Cunninghame (2005).

5.1.2.1 Boundary conditions

Being able to accurately describe the boundary conditions to any domain is an essential part of the quest to obtain a good solution to a problem. Care has to be taken when specifying the boundary conditions as specification of the wrong conditions will lead to the solution of another problem altogether. The boundary conditions employed for the simulations are described in the following paragraphs.

Inflows & outflows

The flow inlets and outlets of the domains were all specified as velocity inlets. At these locations, point profiles of the velocity, the turbulent kinetic energy, its rate of dissipation, and the volume fraction of water were specified. Point profiles of the water velocity were estimated from the equation presented by Rooseboom (1992) for flows influenced by the channel sidewalls. This equation is as follows (McGahey, 2001; Cunninghame, 2005):

$$u(y,z) = \frac{\ln\left(\frac{y}{y_0}\right)\ln\left(\frac{B/2-|z|}{z_0}\right)}{\ln\left(\frac{h}{ey_0}\right)\ln\left(\frac{B/2}{ez_0}\right)}U \tag{5.1}$$

where y and z are the grid coordinates, y_0 and z_0 are the distances from the walls where the magnitude of the velocity is 0, and h and B are the water depth and channel breadth respectively. y_0 and z_0 are dependent on the wall roughness. It was suggested by Simons & Senturk (1977) that the bed roughness could be related to y_0 as follows:

$$y_0 = \frac{k_s}{29.6} \tag{5.2}$$

The bed roughness was taken as the mean diameter of the sediment particles ($d_{50} = 0.000725m$) and so a value of 2.45×10^{-5} was used for y_0. For the glass side walls, the value of z_0 was assumed to be 1×10^{-6} (McGahey, 2001; Cunninghame, 2005). Typically, 120 coordinates were selected for each inlet or outlet and the point velocities determined using Equation 5.1. Selection of the coordinates was based on the expected velocity gradients. The point values of k and ε were obtained from the estimated point velocities. They were related to the point velocity as follows (McGahey, 2001; Cunninghame, 2005):

$$k = 1.5(0.037u)^2 \tag{5.3}$$

$$\varepsilon = \frac{k^{1.5}}{0.3R} \tag{5.4}$$

where R is the hydraulic radius.

The volume fractions of water were specified such that the level of the incoming flow was the same as the expected mean depth. The velocity distribution of air at the inlet was specified such that the air velocity at the air-water interface was approximately equal to the velocity of the water surface. The air velocity was made to gradually reduce as it approached the top boundary.

It was ensured that the velocity and water level profiles for the inlets and outlets were the same to satisfy mass conservation across the domain. The point profiles were specified in text files as required by FLUENT. These were loaded into FLUENT when the boundary conditions were being specified. Details needed in the text files include the number of points, the *x-y-z* coordinates of each point and the corresponding parameter values. FLUENT assigned the parameter values at the inlet and outlet boundary adjacent cells based on the nearest point value.

Walls and symmetry planes

As mentioned earlier, the flows about cylinders are considered to be fairly symmetrical and so only half of the flume was modelled. This approach was adopted by Olsen & Melaaen (1993), Olsen & Kjellesvig (1998), Ali & Karim (2002), Armitage & McGahey (2004) and Cunninghame (2005). It was used to reduce computational expenses. The plane of symmetry was in the *x-y* (vertical) plane and passed through the centre of the pier in the same direction as the approaching flow. FLUENT recognizes that some flows are symmetrical and so permits the specification of boundaries as planes of symmetry. Once a boundary is specified as a symmetry boundary, FLUENT assumes that there is a zero flux of all the quantities across the boundary. In other words, the normal velocity components and normal gradients of all the flow variables are zero at the boundary. Also, the shear stress at a symmetry plane is zero (i.e. it is slip wall).

The flume side walls, the pier, the channel bed, and the top of the domain were specified as wall boundaries. They were all specified as stationary, no-slip boundaries. The effects of wall roughness are significant in turbulent boundary flows. FLUENT accounts for wall roughness effects by modifying the law-of-the-wall. The law-of-the-wall modified for roughness in FLUENT is given as follows (Fluent, 2005):

$$\frac{u_p u^*}{\tau_w / \rho} = \frac{1}{\kappa} \ln\left(E \frac{\rho u^* y_p}{\mu} \right) - \Delta B \tag{5.5}$$

where $u^* = C_\mu^{1/4} k^{1/2}$, u_p is the mean flow velocity at computational point p, y_p is the distance from p to the wall, κ is the Von Karman's constant, E is a roughness parameter and τ_w is the wall shear stress. The term, ΔB, accounts for wall roughness and is determined based on the type of boundary being modelled, which is in turn dependent on the boundary roughness k_s. FLUENT estimates the dimensionless roughness height $k_s^+ (k_s u^* / \nu)$ and estimates ΔB using one of the following formulae:

$k_s^+ \leq 2.25$ (hydraulically smooth flows):

$$\Delta B = 0 \tag{5.6}$$

$2.25 < k_s^+ \leq 90$ (transitional flows):

$$\Delta B = \frac{1}{\kappa}\ln\left(\frac{k_s^+ - 2.25}{87.75} + C_s k_s^+\right) \times \sin\left\{0.4258\left(\ln k_s^+ - 0.811\right)\right\} \tag{5.7}$$

$k_s^+ > 90$ (fully turbulent flows):

$$\Delta B = \frac{1}{k}\ln\left(1 + C_s k_s^+\right) \tag{5.8}$$

where C_s is a constant dependent on the type of wall roughness. The values of C_s and k_s were specified for each simulation. The default value of C_s (0.5) was used in each case. According to Fluent (2005), the use of this value with the k–ε turbulence models reproduces Nikuradse's resistance data for pipes roughened with tightly-packed, uniform sand-grain roughness. There is no clear guideline in the selection of a value for C_s. The roughness height, k_s, for the channel bed was taken as the mean particle diameter ($d_{50} = 0.000725m$). The value of k_s for the pier, side walls and the top of the boundaries were specified as 0.

5.1.2.2 Operating conditions

The operating pressure set equal to the atmospheric pressure (101325Pa) and the reference pressure location was selected such that the operating pressure coincided with the water surface. A value of 9.81m²/s was used for the acceleration due to gravity. Default values recommended by FLUENT for the properties of water and air were used. The density and viscosity of air were given as 1.225kg/m³ and 1.7894×10^{-5}kg/ms respectively. For water, 998.2kg/m³ and 1.003×10^{-3} kg/ms were used respectively.

5.1.2.3 Models employed

Fluid flow model

Automation of the bed adjustment procedure required that a user defined function be written in FLUENT to perform the task. The nature of the user-defined function that was adopted was such that only transient conditions could be modelled. Therefore, the unsteady time averaged Navier-Stokes equations and the continuity equation were solved for all the simulations. These equations were presented in Section 3.1.1.

Multiphase models

In FLUENT, multiphase flows are generally categorised into four regimes; namely gas-liquid or liquid-liquid flows, gas-solid flows, liquid-solid flows and three phase flows (which is a combination of all the three phases). The scour phenomenon that was modelled falls under three phase flow; the free surface flow generally falls under gas-liquid flows whereas the sediment laden flow falls under liquid-solid flows. There are currently two main numerical approaches for solving multiphase flows; the Euler-Lagrange approach and the Euler-Euler approach. The Euler-Lagrange approach is a discrete phase approach in which the fluid is treated as a continuum and the dispersed phase (particles, bubbles or droplets) is tracked through the flow

field. Exchange in momentum, mass and energy between the phases is accounted for. The discrete phase model in FLUENT based on this approach is based on the assumption that the dispersed phase occupies a low volume fraction. In the Euler-Euler approach, the different phases are normally treated as interpenetrating continua. Conservation equations are solved for each phase. The volume fraction of each phase in a cell is computed for each step. The sum of the volume fractions per cell should be 1. Constitutive relationships obtained from empirical data or the kinetic theory (for granular flows) are used to close the conservation equations.

FLUENT provides four models based on the Euler-Euler approach. These are the Volume of Fluid (VOF) model, the Mixture model, the Eulerian model, and the Wet Steam model. The VOF model is a technique used to track the interface between fluids of concern. It is applicable two or more immiscible fluids. A single set of momentum equations is shared by the fluids but the volume fraction of each fluid is tracked in each cell of the domain. It is recommended by Fluent (2005) for stratified flows, free-surface flows, filling, sloshing, the motion of large bubbles in liquids, etc. The Mixture model is similar to the VOF model but is designed for two or more phases which may be either fluid or particulate. It is recommended for particle-laden flows with low loading, bubbly flows, sedimentation, and cyclone separators. Here, the momentum equation for the mixture is obtained by combining the individual momentum equations for all phases. Unlike the VOF model, the Mixture model allows the different phases to move at different velocities by utilizing the concept of slip velocities. The Eulerian model is the most complicated of the four models and solves momentum and continuity equations for each phase. The equations are coupled through the use of pressure and inter-phase exchange coefficients. These are dependent on the type of phases involved i.e. whether granular or non-granular flows are being modelled. Kinetic theory is applied to obtain the properties for granular flows. The Eulerian model is recommended for bubble columns, risers, particle suspension, fluidized beds etc. The Wet Steam model is particularly for modelling wet steam flow. It involves the use of the compressible Navier-stokes equations and two transport equations for the liquid-phase mass-fraction and the number of liquid-droplets per unit volume. More information on the models is provided in Fluent (2005).

Free surface modelling

The free surface in the current model was tracked using the VOF model. As stated previously, a single set of momentum equations is solved for all the phases. A continuity equation is solved for the volume fraction of one or more of the phases in order to track the interface. For a phase, q, the continuity equation is given as:

$$\frac{1}{\rho_q}\left[\frac{\partial}{\partial t}\left(\alpha_q\rho_q + \nabla\bullet\left(\alpha_q\rho_q\mathbf{v_q}\right) = S_{\alpha_q} + \sum_{p=1}^{n}\left(m_{pq} - m_{qp}\right)\right)\right] \tag{5.9}$$

where m_{qp} is the mass transfer from phase q to phase p, m_{pq} is the mass transfer from phase p to phase q, $S_{\alpha q}$ is a source term, ρ_q is the density of q, α_q is the volume fraction of q in the cell and $\mathbf{v_q}$ is the velocity of q. If there are only two phases, the volume fraction of the other phase is determined using the constraint $\alpha_p + \alpha_q = 1$, where α_p is the volume fraction of p in the cell

In each cell that contains different phases, the properties appearing in the transport equations are obtained using a weighted average approach using the volume fractions. For example, for a cell containing two phases, p and q, the dynamic viscosity is estimated as follows:

$$\mu = \alpha_q \mu_q + \alpha_p \mu_p \tag{5.10}$$

where α_p and α_p are the volume fractions of p and q respectively, and μ_p and μ_q are the dynamic viscosities of p and q respectively.

Modelling scour

Examination of the guidelines for the selection of a multiphase model indicates that the ideal model to use in modelling a sediment laden flow like that which occurs at a bridge pier is the Eulerian model. The implications, however, suggest that it will be a while before it would be practical to use this model. Firstly, additional cells would have to be created to accommodate the sand bed. The depth of the bed layer would have to be greater than the depth of the expected scour. Selection of this model would mean that different sets of continuity and momentum equations would have to be solved for each phase i.e. air, water and sediment. It would thus take much longer to solve a particular time step compared to the solution of free surface flow over a rigid bed using the VOF model. Using a time step of length 0.1s on a computational grid of approximately 110,000 cells, it took approximately 45 minutes of real time to simulate 10s of free surface flow over a rigid bed. The time taken to achieve equilibrium scour holes in the laboratory ranged between 48 to 72 hours (2 to 3 days). This implies that solving just one set of momentum and continuity equations for the same duration on a rigid bed would take approximately 12960 to 19440 hours (540 to 810 days) in real time. It would thus be impractical to use the Eulerian model for scour prediction with the computational capacity that was available.

Turbulence model

It can be noted from the discussion on the previous experiments that most of the previous models that were used to predict flow fields about cylindrical piers used some form of the k-ε model for turbulence closure. The k-ε model has been presented in Section 3.1.1.2. According to Olsen (2000), the standard k-ε is mostly used because of the universal nature of its constants. Salaheldin *et al.* (2004) found that both the standard and the RNG tended to overestimate the area of scour and the near-bed velocities but the results were good enough to suggest that they could be used in scour prediction. The most promising model was found to be the RSM. It however solves seven transport equations for the Reynolds stresses as compared to two by the k-ε model. Hence, since the computational expenses of the k-ε model is less than the RSM, it was decided that the k-ε model would be used in the initial stages of the research whilst the automated bed deformation procedure was being developed. The decision was made to examine the scour holes produced by both the k-ε model and the RSM if there was time. The RSM has also been presented in Section 3.1.1.2. The various types of turbulence closure models have been described by Cunninghame (2005) and Fluent (2005).

The RSM and k-ε models are mainly valid in the turbulent region. A suitable procedure must thus be used to adequately model the region near the boundary where viscous effects are of

importance. There are generally three options offered by both the RSM and the k-ε model for treatment of the region near the boundary. These are the use of standard wall functions, non-equilibrium wall functions and by what is known as "enhanced wall treatment". These options may be grouped into two categories based on the type of wall modelling approach employed; namely the wall function approach and the near-wall model approach. In the wall function approach, the need to completely resolve the inner region with a mesh is avoided through the use of semi-empirical formulae. These semi-empirical formulae, referred to as wall functions, are used to represent the region and account for the influence of the wall on the solution variables of the wall-adjacent cells. Turbulence models are thus not modified to account for the effect of the wall. Wall functions consist of laws-of-the-wall for mean velocity and temperature, and formulae for near-wall turbulent quantities. The wall function approach is ideal for flows with high Reynolds numbers since they produce reasonably accurate results and save computational resources (owing to the fact that the viscosity affected region is not resolved). In the near wall modelling approach, the turbulence models are modified in the viscosity affected inner region allowing the entire region to be resolved with the mesh. The near-wall modelling approach is recommended for flows with low Reynolds numbers and flows where the assumptions made for wall functions are invalid.

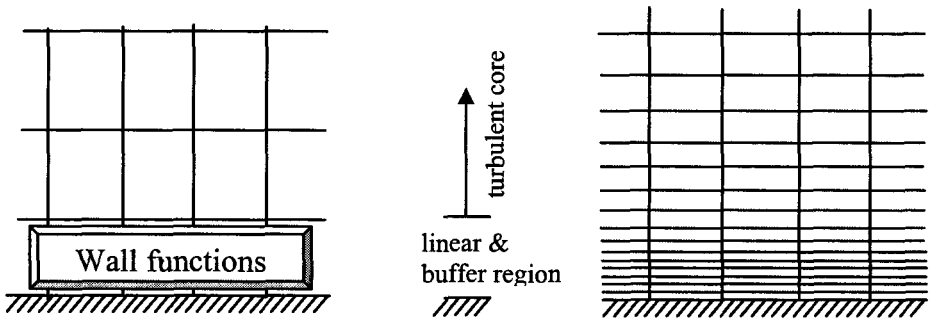

Wall function approach

Near wall model approach

Figure 5-3: Wall treatment approaches

As the names suggest, the standard and non-equilibrium wall functions fall under the wall function approach. The main difference between the two options is the set of equations that are used to represent the viscosity-affected region. Standard wall functions are based on the assumption of constant-shear and local equilibrium. In the non-equilibrium wall functions approach, the effects of pressure gradient and departure from equilibrium are partly accounted for. It is recommended for modelling flows with complex features such as separation, reattachment, and instances where the mean flow and turbulence are affected by severe pressure gradients and rapid changes (Fluent, 2005).

Enhanced wall treatment is a type of near-wall modelling approach in which the model used is dependent on the level of refinement of the mesh. For near-wall meshes that are sufficiently fine for the resolution of the linear sub-layer ($y^+ \approx 0.1$), FLUENT employs a two layer model. The two layer model involves the division of the entire domain into two regions; the viscosity affected region and a fully turbulent region. The normal transport equations for the k-ε models and the RSM are solved in fully turbulent region. For the viscosity affected region, however, a one-

equation model (by Wolfstein, 1969) is employed. The transport equation of k is solved but e is specified using an algebraic equation. A different equation is also used to determine μ_t. The use of a fine near-wall mesh has implications on computational costs. Computational costs may be excessive when the near-wall mesh is fine everywhere. In such cases it is often desirable to have a blend of fine and coarse near-wall meshes. For this scenario, FLUENT is able to combine the two layer approach with enhanced wall functions. The enhanced wall functions are applied to the intermediate meshes (meshes whose near-wall computational nodes fall into the viscosity affected sublayer but are not fine enough to resolve the region) and coarse meshes (meshes with the the near-wall computational nodes falling within the log-law layer). The enhanced wall functions used in FLUENT are obtained by blending the linear and logarithmic laws-of-the-wall into a single wall law that is regarded as valid for the entire region (linear, buffer and turbulent regions). This method ensures that solutions on grids with fine and coarse near-wall meshes possess the accuracy of the two layer approach for the fine near-wall regions but do not compromise significantly on the accuracy of the solution obtained for the relatively coarse near-wall regions.

The wall function approach was employed for all the experiments. Since the solutions involved turbulent boundaries, there was no need to resolve the linear region. The wall-adjacent cells were sized such that computation of the boundary adjacent variables was done in the log-law layer. Cunninghame (2003) studied the effect of the near-wall cell sizes and the different approaches on the estimation of the shear stress profile for flow in an infinitely wide channel. The k-ε model was employed. The enhanced wall treatment and standard wall functions were examined. The results indicate that, for flows in infinitely wide channels, the standard wall functions can produce satisfactory results. The results also showed that the shear stress profile was affected by the level of refinement of the near-bed cells. An important outcome of the study was the fact that even though the depth profile generated was generally satisfactory, the value of the shear stress estimated at the bed level was only fair. Unfortunately, the Movability Number approach is dependent on the variables at the bed. It was therefore anticipated that there would be some error in the estimation of scour.

5.1.2.4 Discretization schemes

The Finite Volume Method has already been introduced in Section 3.1.2. Various schemes are available in FLUENT for obtaining the discretized versions of the governing equations. The different schemes are described by FLUENT. Some are also described by Versteeg & Malalasekera (1995). The options available for the models that were employed were the FIRST ORDER UPWIND, the SECOND ORDER UPWIND, the POWER LAW, the QUICK (quadratic upstream interpolation for convective kinetics), the THIRD ORDER MUSCL (Monotone Upstream-Centered Schemes for Conservation Laws) and the MODIFIED HRIC (High Resolution Interface Capturing).

The FIRST ORDER UPWIND scheme assumes that the cell-centre value holds for the entire cell. The value at the face of each cell is set equal to the centre value of the upstream cell. The SECOND ORDER UPWIND scheme is more accurate than the FIRST ORDER UPWIND scheme. Interpolation of the face values of the cells is obtained from a Taylor series expansion of the cell-centre values. The POWER LAW scheme interpolates the value at the face of a cell through the exact solution of a one-dimensional convection-diffusion equation. The QUICK

scheme utilizes a three-point upstream-weighted quadratic interpolation for the estimation of the cell face values. It is particularly more accurate on a structured grid aligned in the direction of flow. Under such conditions, it is regarded as a third order scheme. The THIRD ORDER MUSCL scheme is obtained by blending the SECOND ORDER UPWIND scheme and the CENTRAL DIFFERENCING scheme (which interpolates the value at a face using the cell centre values of the cells that share the face). The MODIFIED HRIC option was only available for the VOF model and is particularly meant for interface tracking. It is a scheme which uses a non-linear blend of upwind and downwind differencing for face value determination. The QUICK scheme was employed for all the models as it was it believed that it would yield more accurate results, particularly for the grid being used.

5.1.2.5 Pressure-velocity coupling

The pressure and velocity fields are generally unknown prior to the solution of a particular flow field. For incompressible fluids, inspection of the RANS equations reveals that they all contain each of the flow variables (velocity and pressure components). The continuity equation, on the other hand, contains only the velocity components. A way of solving the equations (momentum and continuity) is to discretize the equations in such a way that they can be solved together. According to Shaw (1992), some Finite Element codes have been developed this way but the approach results in large matrices which require a large amount of computational effort to produce a solution. The other approach is dependent on the fact that most of the terms in the RANS equations are functions of the velocity components and so makes the RANS equations desirable for use in the determination of the velocity field. The solution of RANS equations alone however requires that the pressure field be known. Unfortunately, it is not known and it is a normal procedure to determine it as part of the solution. The key to the solution of the equations lies in the fact the correct solution to the momentum equations must satisfy the continuity equation. In other words, if the correct pressure field is applied to the momentum equations the velocity field that is determined has to satisfy the continuity equation. Iterative procedures are normally used to obtain a solution. Generally, the velocity and pressure fields are guessed initially and the discretized momentum equations are solved to obtain a new velocity field. A pressure correction equation derived from the continuity equation is then used to estimate a pressure correction field which is in turn used to update the pressure and velocity fields. The updated fields are then used as the initial values for the next iteration. The iterations are continued until a converged solution is obtained, at which point the correct pressure and velocity fields are deemed to have been determined (Shaw, 1992; Versteeg & Malalasekera, 1995).

Various schemes have been developed for the coupling of pressure and velocity. Differences in the schemes arise from the nature of the pressure correction equations, the stages at which pressure correction is computed and the number of times the pressure and velocity fields are corrected in a single iteration. The schemes offered by FLUENT for iterative time advancements include SIMPLE (Semi-Implicit Method for Pressure-Linked Equations), SIMPLEC (SIMPLE-Consistent) and PISO (Pressure Implicit with Splitting of Operators). The PISO scheme is recommended by FLUENT for all transient flow computations and was employed for all the simulations. Jang *et al.* (1986) illustrated the computational efficiency and robust convergence behaviour of the PISO algorithm for problems in which the momentum equations were not coupled to scalar variables (Versteeg & Malalasekera, 1995; Fluent, 2005).

5.1.2.6 Pressure interpolation

FLUENT's default scheme for pressure estimation at the cell faces performs pressure interpolation using the momentum equation coefficients. The scheme cannot be used in cases where the pressure profile has large gradients at the cell faces as it results in over- or under-estimation of cell velocities. Problems are faced when the default scheme is used for flows with large body forces, such as strong swirling flows. Alternative schemes provided by FLUENT in such cases are the LINEAR scheme, the SECOND-ORDER scheme, the BODY-FORCE-WEIGHTED scheme and PRESTO (Pressure Staggering Option). The different schemes are described by Fluent (2005) as follows:

LINEAR scheme – the face pressure values are determined as the mean of the pressure values in the neighbouring cells.

SECOND-ORDER scheme - the face pressure is reconstructed using the same approach employed in the SECOND-ORDER UPWIND scheme i.e. the face pressure values are estimated through a Taylor series expansion. This scheme is better than the LINEAR scheme but cannot be used for flows with discontinuous pressure gradients (e.g. free surface flows modelled with the VOF model).

BODY-FORCE-WEIGHTED scheme- the face pressure is computed by assuming that the normal gradient of the difference between the pressure and body forces is constant. The scheme works well for buoyancy and axisymmetric swirl calculations.

PRESTO- it is sometimes necessary to employ a staggered grid when estimating the pressure field. This is because problems are sometimes encountered when an attempt is made to use a regular grid to estimate some pressure distributions (highly non-uniform pressure distributions in particular). Issues pertaining to staggered grids and their use are discussed by Versteeg & Malalasekera (1995). The PRESTO scheme uses the discrete continuity balance for a staggered control volume about the cell face to compute the face pressure. The scheme is available for all meshes.

Pressure interpolation in the simulations was performed using the PRESTO option.

5.1.2.7 Under-relaxation

Due to the nonlinear nature of the governing equations that are solved, it is usually necessary to control the change in the values of the variables. Control of the change in variables during the solution process is achieved through the use of 'under-relaxation factors'. The computed changes are reduced by multiplying them by the factors. For example, the new value of a variable ϕ is computed as follows:

$$\phi = \phi_{old} + \alpha \Delta\phi \tag{5.11}$$

Where ϕ_{old} is the old value of ϕ, α is the under-relaxation factor and $\Delta\phi$ is the computed change in ϕ.

The default under-relaxation factors specified in FLUENT were used for most of the simulations as they produced stable solutions. For some simulations, however, solution behaviour was unstable and the under-relaxation factors for pressure, momentum, k, and ε had to be reduced to values between 0.2 and 0.5 as recommended by Fluent (2005).

5.1.2.8 Solution initialization and convergence criteria

Initialization of the flow variables is a part of the solution process that needs to be done with prudence. The initial flow field that is guessed affects the rate at which a solution is attained or convergence is reached. Convergence is achieved much faster when the initial flow variables are close to the actual solution. Initialization of the flow variables for each simulation was performed taking the expected mean flow depth and velocity into account. Since flow was predominantly in one direction (x-direction), the initial flow velocity in each cell was given a value slightly less than the mean flow velocity and specified to be in the x-direction. The lower value was to ensure that the velocities in the near-bed cells would also converge faster. The volume fraction of water in each cell was also specified. The volume fractions of water in the cells below the expected water surface level were set equal to 1 and the values in those above were set equal to zero, representing the water in the channel and the air layer on top.

The flux imbalance of a variable summed over all the cells in a domain and scaled by the flow rate through the domain is referred to as a scaled residual. The convergence criteria were based upon the scaled residuals for each variable. Convergence was assumed to be achieved once the scaled residual for each variable was less than 10^{-3}.

5.1.3 Bed deformation model

For each simulation, it was assumed that bed deformation occurred in stages and flow conditions at each stage were steady. The unsteady RANS equations were solved iteratively at each stage until equilibrium conditions were attained (i.e. flow conditions were constant). Once equilibrium was attained, scour potentials at the bed were computed and the bed was deformed accordingly. The process was repeated until an equilibrium scour hole developed (i.e. the scour potential at each point on the bed was less than or equal to zero for successive stages.

Automation of the bed deformation process required that a User-defined function (UDF) be written to access the flow variables, compute the movability numbers, and to adjust the grid. UDFs in FLUENT are written in the C programming language and are use to enhance its standard features. Besides the normal C syntax, FLUENT provides additional macros to facilitate the programming and use of CFD objects as defined in FLUENT. Knowledge of these macros is necessary for accessing and manipulating the flow variables and the grid. The UDFs are written in text files and saved with the extension .c. The FLUENT 6.2 UDF manual provides the necessary information on the use of UDFs in FLUENT.

The dynamic mesh model in FLUENT was employed for the automated grid deformation procedure. This model is used in simulations where the shape of the domain changes with time due to motion on the boundaries. The motion on the boundaries may or may not depend on the solution at a particular time step. The domain is divided into moving and non-moving regions

and the description of the motion is specified on either face or cell zones of the moving regions. There are generally four 'DEFINE' macros that can be used in FLUENT to control the behaviour of a dynamic mesh. These are DEFINE_CG_MOTION, DEFINE_GEOM, DEFINE_GRID_MOTION, and DEFINE_SDOF_PROPERTIES. The DEFINE_CG_MOTION is for centre of gravity motion. The user provides FLUENT with the linear and angular velocities at each time step and FLUENT updates the node positions on the dynamic zone using the velocities. The node position update is based on solid-body motion. The DEFINE_GEOM macro is used to specify the geometry of a deforming zone. FLUENT by default facilitates the definition of node motion along a planar or cylindrical surface. Node positions are updated by apply a solid-body motion equation and so relative motion between the nodes is not possible. The DEFINE_GRID_MOTION is used in situations where relative motion between nodes is required. The position of each node is updated independently. The last macro, the DEFINE_SDOF_PROPERTIES is used to specify custom properties of moving objects for the six-degrees of freedom (SDOF) solver. The SDOF solver computes the linear and angular velocities from the force balance on a solid body. The computed velocities are then used to update node positions.

Accurate simulation of the scouring process required that relative motion occurred between the nodes. It was necessary that the movement of each node occurred independent of the other nodes. The sediment angle of repose was the only thing that imposed a constraint on the relative movement of the nodes. The appropriate macro for the task at hand was therefore the DEFINE_GRID_MOTION macro. The macro has five arguments; the name of the UDF, a pointer to the domain, *d*, a pointer to the structure that store the dynamic mesh attributes, *dt*, the current time, *time*, and the time step, *dtime*. The variables *d*, *dt*, *time* and *dtime* are passed by FLUENT to the UDF. Thus, the UDF had to be developed about these variables i.e. access to the cells, faces, nodes and their variables were through the variables.

As explained in Section 5.1.1 each domain that was used in the simulations had to be divided into a deforming zone and a non-deforming region. The deforming region was kept close to the region where scour was expected. The aim was to enable cell loops, estimation of Movability numbers and bed adjustments to be performed only in the necessary regions. This would avoid any problems with memory allocation and reduce the time taken by the UDF to perform the bed modification.

The nodes were moved in the vertical direction to reflect scour. The extent of movement was dependent on the scour potential at the node. The definition of scour potential employed by McGahey (2001) & Cunninghame (2005) was used. According to the definition, the scour potential, , is given by:

$$\Omega = Mn - \psi Mn_c \tag{5.12}$$

where Mn is the movability number at a point on the bed, Mn_c is the critical movability number on a flat bed and ψ is the slope correction factor. According to this criterion, a positive value of Ω indicates the extent to which scour is likely to occur.

Deposition was not modelled as it would require particle tracking of some sort and hence increased computational demands. It was believed that this would not significantly affect scour estimates since deposition occurred mainly downstream of the pier and did not considerably affect the flow distribution upstream.

Two relationships were examined for the movement of bed nodes. The first one approximated bed movement using a linear relationship between the scour potential (and hence the movability number) and the depth of scour. The vertical movement, Δy, was estimated as:

$$\Delta y = -C_{scour}\Omega \tag{5.13}$$

where C_{scour} is a translation factor. Its value was estimated based on the value of Ω. For each bed modification stage, C_{scour} was determined so that the maximum displacement at any node was less than or equal to a user-specified value, $\Delta y_{\max}$. The purpose of $\Delta y_{\max}$ was to restrict node movement in order to avoid the risk of distorting the true shape of the scour hole as it progressed. The UDF required that the user specified a scour potential limit, Ω_{limit}. At each bed deformation stage, the largest scour potential on the bed, $\Omega_{largest}$, was determined and if $\Omega_{largest} \geq \Omega_{limit}$, C_{scour} was estimated as follows:

$$C_{scour} = \frac{\Delta y_{\max}}{\Omega_{largest}} \tag{5.14}$$

The estimated value of C_{scour} would then be used to estimate the bed deformations at all the nodes. In this way there would be relative movement between the nodes with the maximum displacement occurring at the location with the largest scour potential. In instances where $\Omega_{largest} < \Omega_{limit}$, $\Delta y_{\max}$ was multiplied by the factor $\Omega_{largest}/\Omega_{limit}$ to obtained a new maximum displacement, $\Delta y_{\max 1}$. Equation 5.14 was then employed to estimate C_{scour} but this time $\Delta y_{\max}$ was replaced with $\Delta y_{\max 1}$. The idea was to mimic the scouring process and gradually reduce the maximum displacement (bed movement) as the scour potential values approached zero (i.e. $\Delta y_{\max} \rightarrow 0$ as $\Omega_{largest} \rightarrow 0$).

The second relationship for bed movement was based on Equation 2.54 which relates the Movability Number to the intensity of motion. It was assumed that the intensity of motion, I, was directly proportional to the depth of scour and the following relationship was obtained:

$$I = C_{scour}\Delta y \tag{5.15}$$

where C_{scour} is the constant of proportionality. The assumption was made because the number of particles being transported from an area is proportional to the scour volume and so if the area remains constant, the number of particles transported within a given period has to be proportional to the scour depth that results within that period. Substituting Equation 5.15 into Equation 2.54 yielded:

$$Mn = \psi\left[0.2405 + 0.0066\ln\left(C_{scour}\Delta y\right) + 0.204\frac{d}{h}\right] \tag{5.16}$$

where Mn is the Movability number, d is the particle size and h is the depth of flow. Making Δy the subject gave the following relationship for node displacement:

$$\Delta y = e^{\frac{1}{0.0066}\left[\frac{Mn}{\psi} - 0.204\frac{d}{h} - 0.2405\right] - \ln C_{scour}} \tag{5.17}$$

Again, $\Omega_{largest}$ and Ω_{limit} were determined at each stage. When $\Omega_{largest} \geq \Omega_{limit}$, C_{scour} was estimated as follows:

$$C_{scour} = e^{\frac{1}{0.0066}\left[\frac{Mn_{largest}}{\psi_{largest}} - 0.204\frac{d}{h} - 0.2405\right] - \ln(\Delta y_{\max})} \tag{5.18}$$

Where $Mn_{largest}$ and ψ_{largest} are the Movability Number and slope correction factor corresponding to the node at which the largest scour potential exists. When $\Omega_{largest} < \Omega_{limit}$, C_{scour} was estimated from Equation 5.18 by replacing $\Delta y_{\max}$ with $\Delta y_{\max 1} = \Omega_{largest}/\Omega_{limit} \times \Delta y_{\max}$.

5.1.4 Slope correction

Estimation of the slope correction factor, ψ, requires that the longitudinal and transverse slopes of the bed with respect to the direction of flow be determined. For each bed-adjacent cell, the horizontal components of the velocity vector, $\mathbf{v}_x$ and $\mathbf{v}_z$, were first determined to get the direction of flow. It was then assumed that the four nodes on the bed face lay on a planar surface and the equation of the plane was determined by computing the area normal vector, $\mathbf{a_n}$, and the face centroid, $\mathbf{c_f}$.

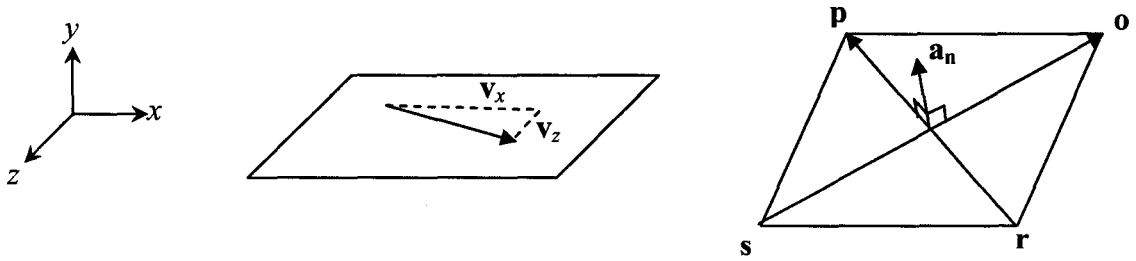

Figure 5-4: Vectors on a horizontal plane and a bed face

If $\mathbf{e} = \mathbf{o} - \mathbf{r}$ and $\mathbf{f} = \mathbf{q} - \mathbf{s}$ are the diagonal vectors of the face (see Figure 5-4), then $\mathbf{a_n}$ was computed as follows:

$$\mathbf{a_n} = \frac{1}{2}(\mathbf{e} \times \mathbf{f}) \tag{5.19}$$

The face centroid was also estimated as follows:

$$\mathbf{c}_f = \frac{1}{4}(\mathbf{p}+\mathbf{o}+\mathbf{r}+\mathbf{s}) \tag{5.20}$$

The equation of the plane was then determined as:

$$ax+by+cz+d=0 \tag{5.21}$$

where x, y, z are points on the plane, $a=\mathbf{a}_{nx}$, $b=\mathbf{a}_{ny}$, $c=\mathbf{a}_{nz}$, and $d=-\left(\mathbf{a}_{nx}\mathbf{c}_{fx}+\mathbf{a}_{ny}\mathbf{c}_{fy}+\mathbf{a}_{nz}\mathbf{c}_{fz}\right)$. Once the equation of the plane was determined, a vector on the plane in the direction of the flow was obtained using $\mathbf{v}_x$ and $\mathbf{v}_z$ i.e. if the starting point of a horizontal vector, $\mathbf{w}=\mathbf{v}_x\mathbf{i}+\mathbf{v}_z\mathbf{k}$, is the centroid of the face, then $\mathbf{w}$ may be projected onto the face to obtain the vector $\mathbf{q}$ as follows:

x-component:

$$\mathbf{q}_x = \mathbf{v}_x \tag{5.22}$$

y-component:

$$\mathbf{q}_y = -\frac{1}{b}\left(a\left(\mathbf{c}_{fx}+\mathbf{v}_x\right)+c\left(\mathbf{c}_{fz}+\mathbf{v}_z\right)+d\right)-\mathbf{c}_y \tag{5.23}$$

z-component:

$$\mathbf{q}_z = \mathbf{v}_z \tag{5.24}$$

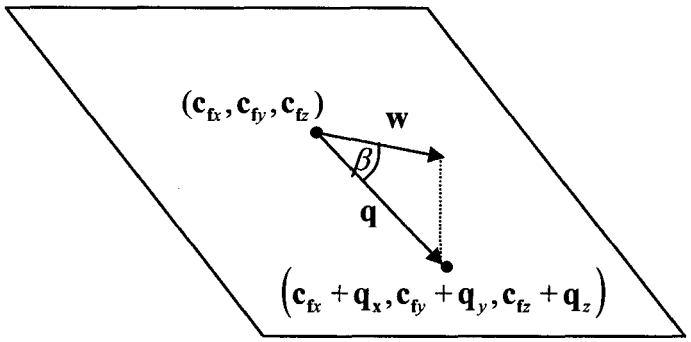

Figure 5-5: Longitudinal slope determination

The longitudinal and transverse slopes, β and γ, were then determined from $\mathbf{q}$ as follows:

Longitudinal slope:

$$\beta = \arctan\left(\frac{\mathbf{q}_y}{\sqrt{\mathbf{q}_x^2 + \mathbf{q}_z^2}}\right) \tag{5.25}$$

Transverse slope:

$$\mathbf{t} = \mathbf{q} \times \mathbf{a}_n \tag{5.26a}$$

$$\gamma = \left|\arctan\left(\frac{\mathbf{t}_y}{\sqrt{\mathbf{t}_x^2 + \mathbf{t}_y^2}}\right)\right| \tag{5.26b}$$

5.1.5 Accounting for angle of repose

In theory, when the bed slope becomes greater than the angle of repose, ϕ_r, the particles begin to slide. The sliding continues until the bed slope eventually returns to the angle of repose. To take this phenomenon into account, it was assumed that the sliding particles also contributed to the scour volume. It is believed that this was a fair assumption since for a bed slope to become steep, the rate of scour at the bottom had to be larger than the rate of scour at the top. In such a case, it would be safe to assume that the particles sliding towards the bottom would be transported away. Once the bed had been deformed using the scour potentials, the maximum angle each cell face made with the horizontal plane, ϕ_{max}, was checked. If it was greater than ϕ_r, the nodes were adjusted vertically so that the ϕ_{max} was equal to ϕ_r. This ensured that the relative angle between any two nodes on the same face was less than or equal to the angle of repose. The node with the lowest vertical coordinate was always used as a reference point for the adjustment. The maximum face angle was determined from $\mathbf{a}_n$ and the unit vector in the vertical direction, $\mathbf{e}_y$ as follows:

$$\phi_{max} = \arccos\left(\frac{\mathbf{a}_n \bullet \mathbf{e}_y}{|\mathbf{a}_n|}\right) \tag{5.27}$$

To adjust the nodes when $\phi_{max} > \phi_r$, ϕ_{max} was set equal to ϕ_r and the vertical coordinate of $\mathbf{a}_n$ was estimated using:

$$\mathbf{a}_{ny} = \frac{\sqrt{\mathbf{a}_{nx}^2 + \mathbf{a}_{nz}^2}}{\tan\phi_r} \tag{5.28}$$

The nodes on the face were adjusted so that they lay on the plane which passed through the lowest point and had $\mathbf{a}_n$ as the normal.

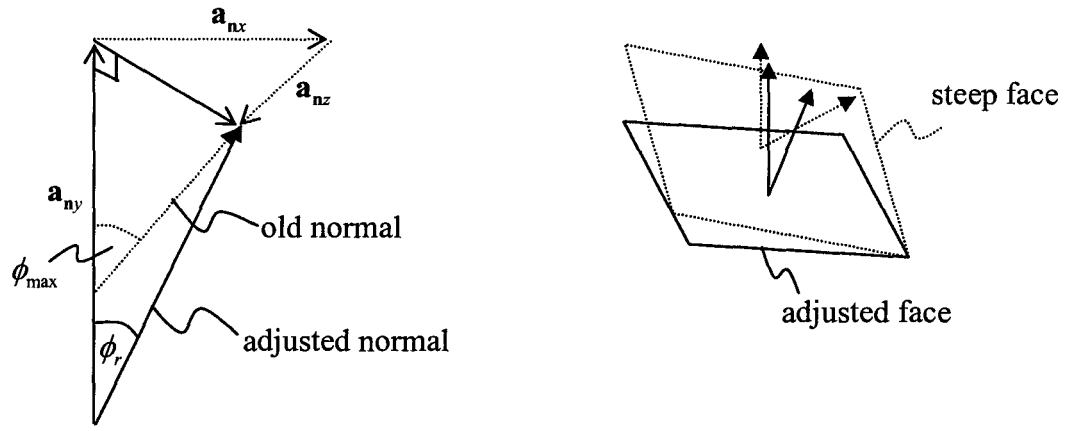

Figure 5-6: Adjustment of bed slope to reflect sliding

5.1.6 Adapting the mesh

Attempts were made to use the adaptive mesh capabilities of FLUENT to modify the mesh within the domain as the solution progressed. It soon became apparent that the user had little control over the manner in which the mesh was modified. An additional UDF was therefore written to modify the mesh. This ensured that the mesh was updated in a desirable way and that cell heights were appropriate for the next stage. The structured nature of the mesh in the vertical direction was taken into consideration when developing the UDF. Only the locations of the nodes were stored for each mesh update stage. It was not necessary to store information on the node connectivity as they were implicitly known in the vertical direction.

Two arrays were used to store the node coordinates and the pointers to the nodes. Two additional arrays were also created to store the coordinates and pointers of nodes with the same horizontal coordinates. These additional arrays were used for manipulating the grid. Problems with memory allocation were encountered when the number of nodes within the deforming region was greater than roughly 115,000. The number of nodes used in the deforming region for each simulation was thus restricted to a quantity smaller than this figure.

The mesh update UDF was called at each stage after the bed had been modified to reflect scour. Nodes below half the mean flow depth with the same horizontal coordinates were determined and their positions are set according to the following relationship (Gambit, 2004):

$$r = e^{\frac{L}{N-1}(x_u - 0.5)} \tag{5.33}$$

where r is the ratio between two successive node intervals, L is the distance from the bed to half the mean flow depth, N is the number of nodes and x_u is a user-specified constant. Half the mean

flow depth was chosen as a reference level because it was expected that flow at the point would be less affected by the bed and free surface, and so the mesh could be relatively coarser in this region. L was estimated as the difference between the vertical coordinates of the highest and lowest nodes. The locations of the vertical coordinates of the other nodes (intermediate nodes) were specified using a geometric progression i.e. if a_n represents the nth interval then a_n was estimated as follows:

$$a_n = ar^{n-1} \tag{5.34}$$

The factor a was obtained using the definition of a geometric series, which may be written in the form:

$$(1-r)\sum_{k=0}^{N-2} ar^k = a - ar^{N-1} \tag{5.35}$$

Rearranging Equation 5.35 and noting that $\sum_{k=0}^{N-2} ar^k = L$ gave:

$$a = \frac{L(1-r)}{1-r^{N-1}} \tag{5.36}$$

The choice of an appropriate value of x_u ensures that the cells closest to the bed are least affected by the bed deformation. The value of x_u selected needs to be less than 0.5 to ensure that cell sizes progressively increase from the bed towards the mean flow depth. The smaller the value of x_u, the smaller the size of the cells close to the bed and the smaller the effect of bed deformation on bed adjacent cells. The value of x_u should be such that bed adjacent cell heights are consistent with the wall treatment approach being used.

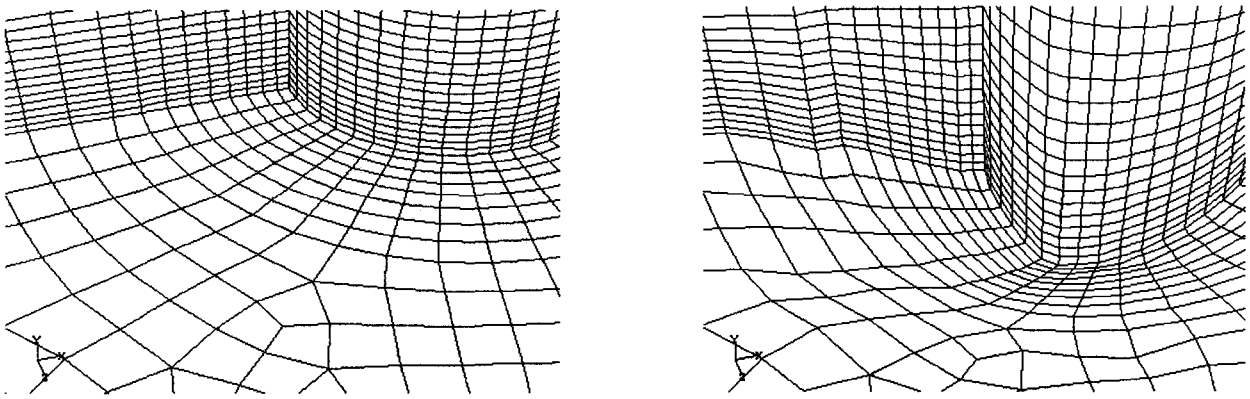

Figure 5-7: Illustration of mesh adaptation

5.2 Summary

The numerical models and methodologies employed in the research have been presented in this chapter. It began with a description of the grids used and how they were generated. It then went on to describe the boundary conditions and the models that were used in FLUENT 6.2. The user-defined function for bed deformation was explained and the chapter concluded with an elaboration on the mesh modification routine. Based on the procedures described herein, numerical simulations of the physical experiments presented in Chapter 4 were performed. The results of these simulations are presented in the following chapter.

Chapter 6
Results and discussions

The numerical simulations performed were of the physical experiments presented in Chapter 4. Different grids were generated for the simulations and their abilities to predict the expected flow fields were assessed. Based on the assessments, an appropriate grid type was selected for the scour hole evolution simulations. The performances of both the standard k-ε model and the Reynold Stress Model in predicting the flow field and the bed Movability Numbers were also examined. Simulations were then performed using the chosen grid type and the standard k-ε model. Results from the assessments and the simulations are presented here. The nature of the predicted scour holes and the general trends in their evolution were very similar for all the simulations. Hence, even though all the predicted scour depths are stated, presentation of the results concentrates mainly on those from one simulation (i.e. simulation of "Experiment 1") for brevity.

6.1 Prediction of flow field

6.1.1 Grids

Three different meshes (coarse, intermediate and fine) were examined to determine the influence the size of the grid had on the predicted flow field and hence Movability Numbers. The grids used are shown in Figure 6-1. The grids consisted of approximately 127,000, 176,000 and 286,000 cells respectively.

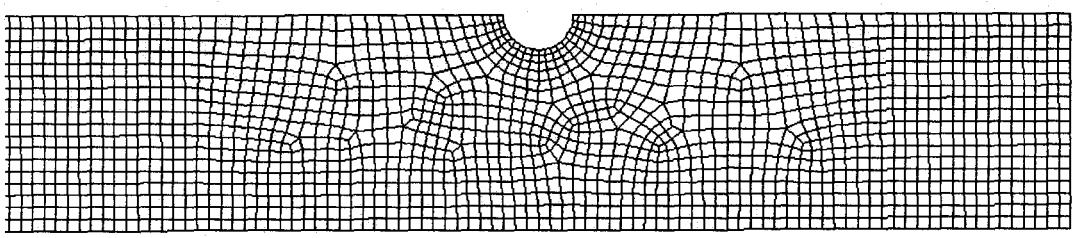

Coarse mesh

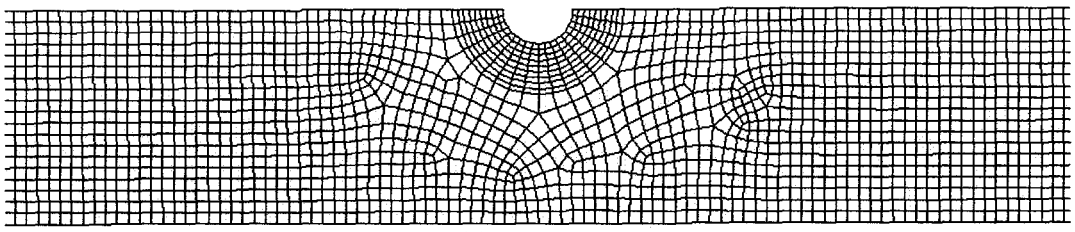

Intermediate mesh

Figure 6-1a: Plan view of assessed meshes - near-pier region

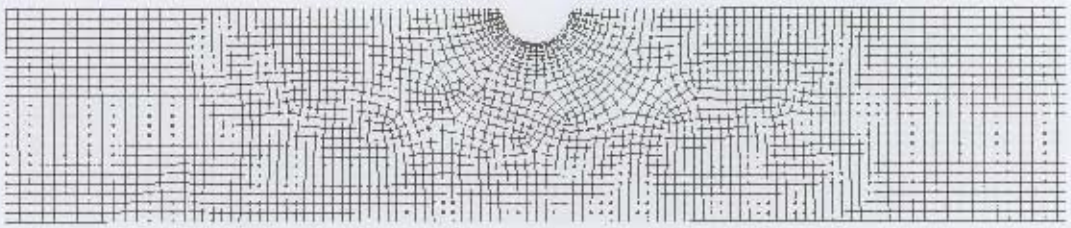

Fine mesh

Figure 6-1b: Plan view of assessed meshes - near-pier region

6.1.2 Free surface

Numerical simulations of Experiment 1 were performed for the examination of flow field prediction on the different grids. The flow had a mean flow velocity of 0.196m/s and a mean flow depth of 0.095m. Transient simulations were run using the standard k-ε model for closure. Figure 6-2 shows the predicted surface profiles at equilibrium within the vicinity of the pier.

Coarse mesh

Intermediate mesh

Figure 6-2a: Depth contours of free surface

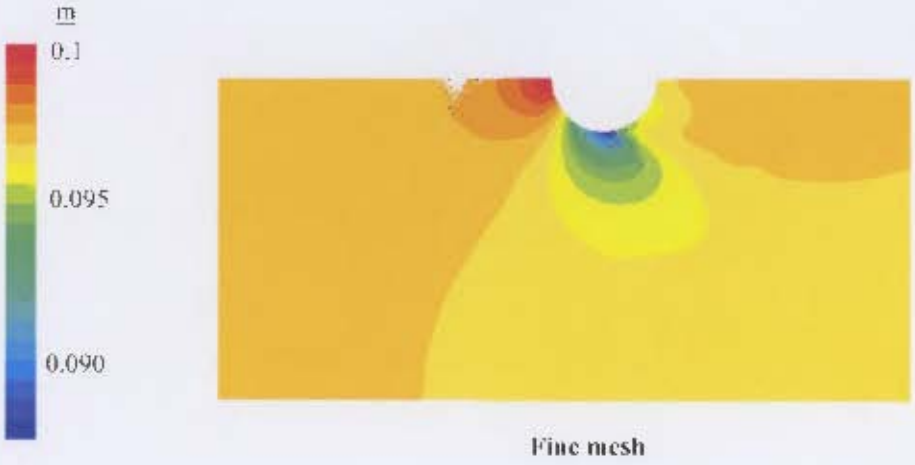

Figure 6-2b: Depth contours of free surface

By and large, the surface contours generated by all the grids were similar. The profiles appeared to be realistic and were in agreement with descriptions in literature (Raudkivi, 1998; Melville & Coleman, 2000 etc). The water level increased at the front of pier due to an increase in pressure and dropped along the sides of the pier where the velocity had increased due to flow acceleration. All grids displayed this trend with the finer grid displaying the greatest relative change in water level between the front and the sides of the pier. The change in water level was also noticed in the laboratory. This is shown in Figure 6-3.

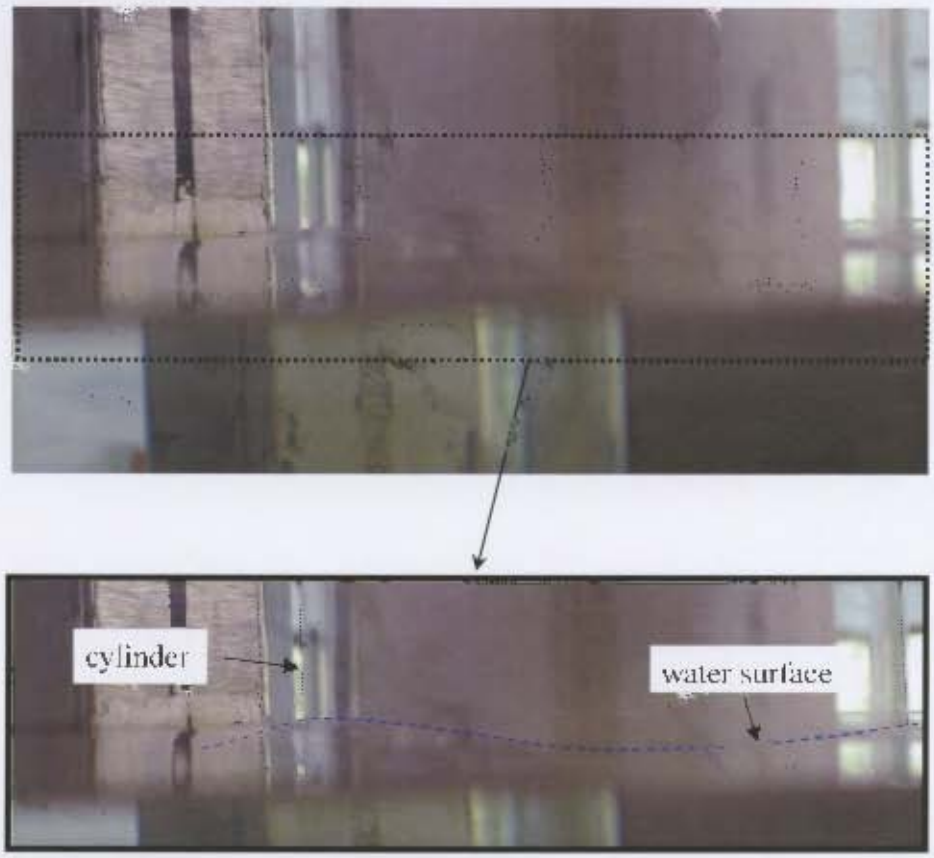

Figure 6-3: Variation of water surface around pier

It was also noticed, both in the numerical simulations and the experiments, that the water surface level was only approximately parallel to the channel bed which was flat. It in fact sloped very mildly from the upstream end towards the downstream end. The slope was however slight enough to permit the assumption of uniform flow.

6.1.3 Velocity field on flat bed

Measurements of the velocity field were not taken in the laboratory and so the predicted flow fields had to be compared to observed fields in literature. The predicted velocity fields at the upstream symmetry plane and on the bed for the simulations carried out in the section above are shown in Figure 6-4 for the different grids.

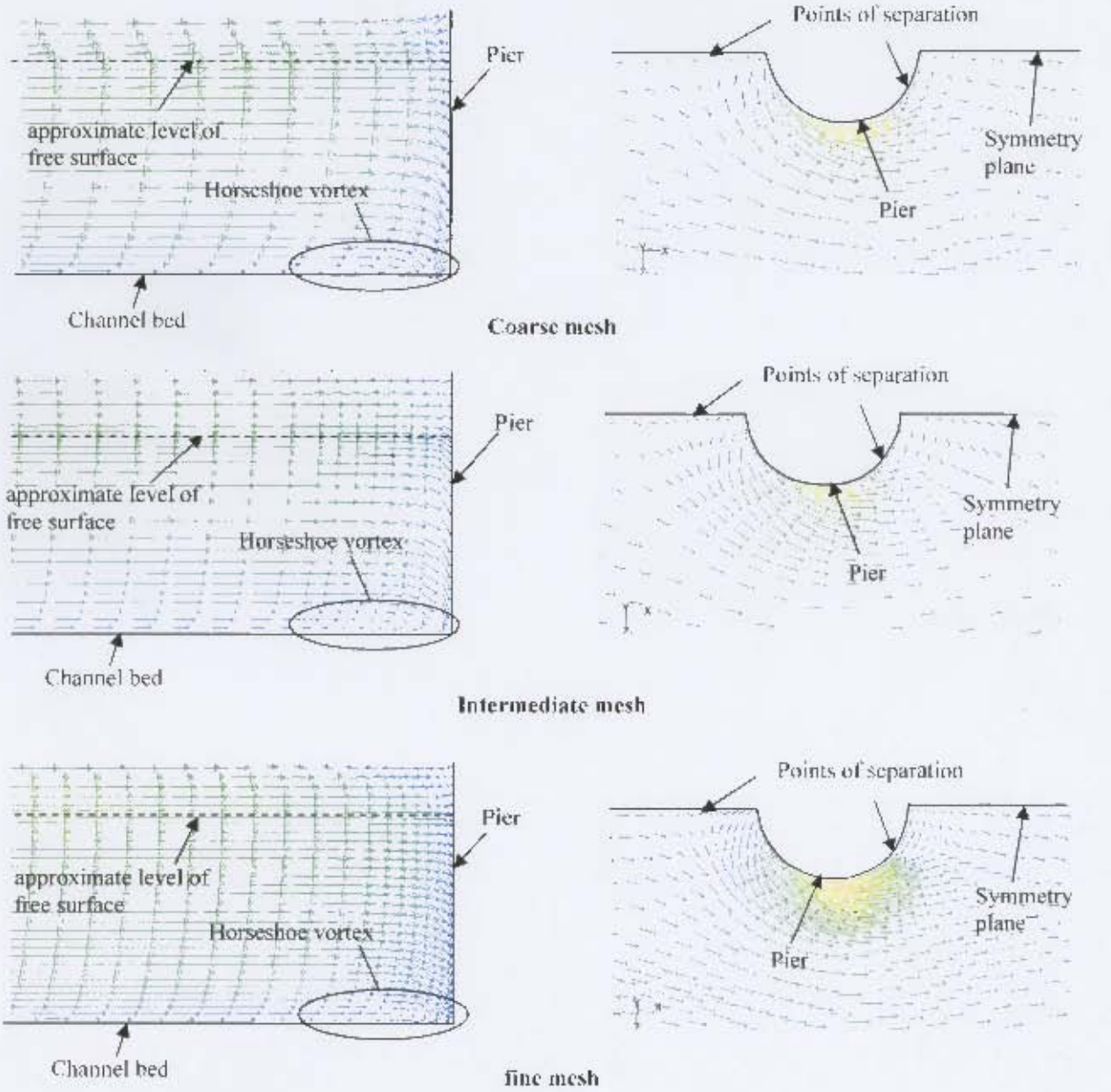

Figure 6-4: Velocity vector fields in front of pier (along symmetry plane) and on bed

The logarithmic profile of the approach velocity is evident in each case. All the models predicted what seemed to be the development of a single vortex in front of and at the base of the pier. The pier Reynolds number for this flow was computed to be 19,600. This value was much lower than that for the flow Dargahi (1990) used to describe the system of horseshoe vortices in front of the pier ($Re_d = 39{,}000$) and so it may be concluded that the flow was not strong enough for all the described vortices to develop. Vortex formations similar to those described by Dargahi (1990) have been reported by Unger and Hager (2005b). However, their experiments also had pier Reynolds numbers between 120,000 and 200,000. Muzzami *et al.* (2004), found that the shape of the primary horseshoe vortex was dependent on the value of Re_d. For flows with $Re_d \leq 5000$, the horseshoe vortex was found to be circular in shape. The shape, however, became more and more elliptical with increasing Re_d. Also the vertical dimension of the vortex was found to be governed by parameters related to the upstream velocity. The size of the vortex increased with the development of the scour hole. As can be seen, the predicted vortices were all elliptical in shape. The vortex is easier to discern in the fine grid.

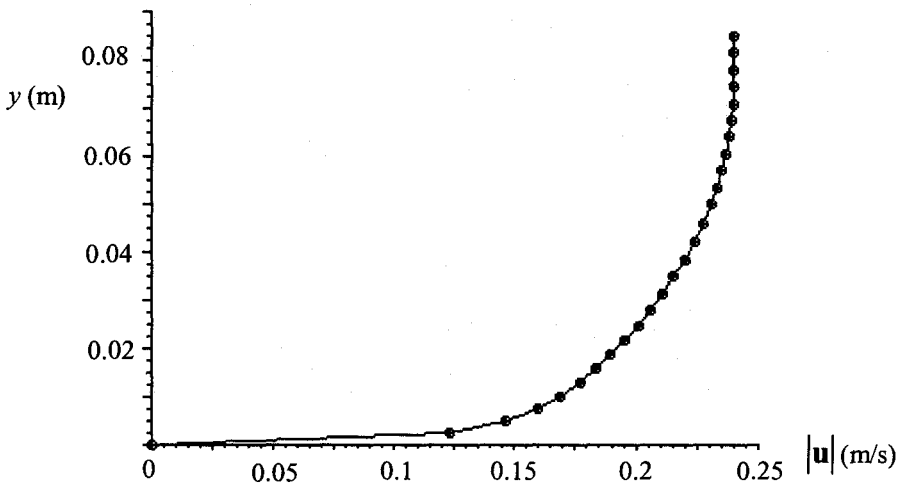

Figure 6-5: Approach velocity distribution (0.3m upstream)

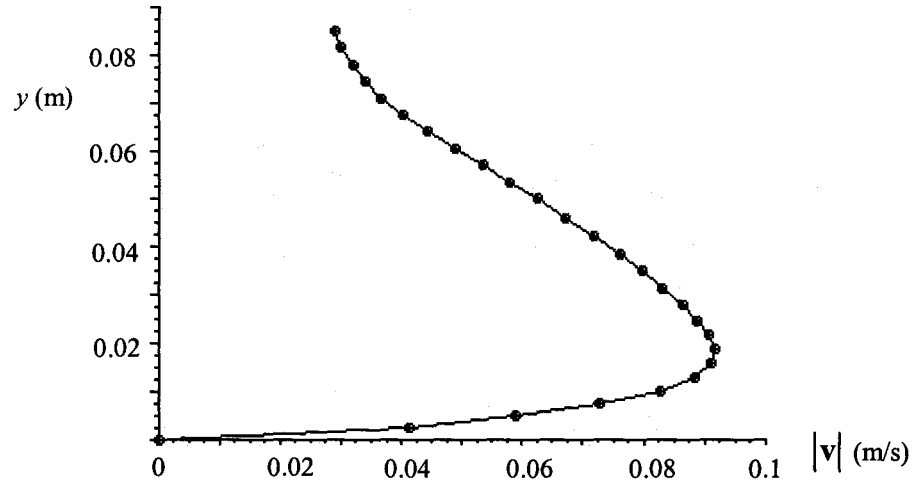

Figure 6-6: Downflow velocity distribution in front of pier

All the grids indicate a general downward flow in front of the pier. Again, it is more evident in the fine grid as it is more refined near the pier. This suggests that the fine grid would be able to provide a better account of the effect of the downflow on the scouring process. An examination of the fine grid indicates that the maximum velocity of the downflow is approximately 0.92m/s, which is 46% of the mean approach velocity. Breusers & Raudkivi (1991) and Raudkivi (1998) state that the maximum velocity of the downflow is approximately 40% of the mean approach velocity in the absence of scour. Ahmed & Rajaratnam (1998) observed from a very limited number of data points that the ratio of the maximum downflow velocity to the mean approach velocity was approximately 38% and occurred at about 35% of the mean flow depth. Figure 6-6 indicates that the maximum velocity occurred at approximately 24% of the mean flow depth.

None of the grids predicted the bow wave which has been noted and described by many experimental researchers. It was interesting to note that none of papers consulted on the numerical modelling of scour at piers reported the prediction of a bow wave at the water surface. Another flow feature that most of the numerical models have not been able to predict is the vortex street behind the pier (e.g. Olsen & Kjellesvig, 1998; Yen *et al.*, 2001; Ali & Karim, 2002; Armitage & McGahey, 2003; Cunninghame, 2005). This could be due to the fact that the cell sizes of the grids used have not been at a small enough scale to capture these features.

A look at the velocity vectors (x-z plane) close to the bed ($y = k_s$) indicates that all the grids predict flow separation at approximately 40mm ($0.4h_p$) upstream of the pier. This flow separation is due to the reversed flow at the base of the pier. This pattern was also noted in results presented by Olsen & Melaeen (1993), Yen et al. (2001), Ali & Karim (2002) and Cunninghame (2005). Streamlines presented by Raudkivi & Sutherland (1982) for flow at a distance of 2mm from a flat bed with a mean velocity of 0.25m/s about a cylindrical pier of diameter 50.8mm display the same pattern. Also, all the grids predicted the flow separation at the sides of the pier. They also predicted vortices in the lee of the pier. These vortices are shown in Figure 6-7. The coarse and intermediate grids only predicted one vortex close to the bed behind the pier. The fine grid predicted two vortices behind the pier; one close to surface and the other near the bed. A highly turbulent zone was seen in the laboratory. It is most probable that the nature of the predicted vortices is affected by the symmetry condition which assumes a zero flux of flow quantities at the boundary and so acts like a wall. If the entire domain had been modelled, interaction between the vortices would have resulted in different flow patterns in the region behind the pier.

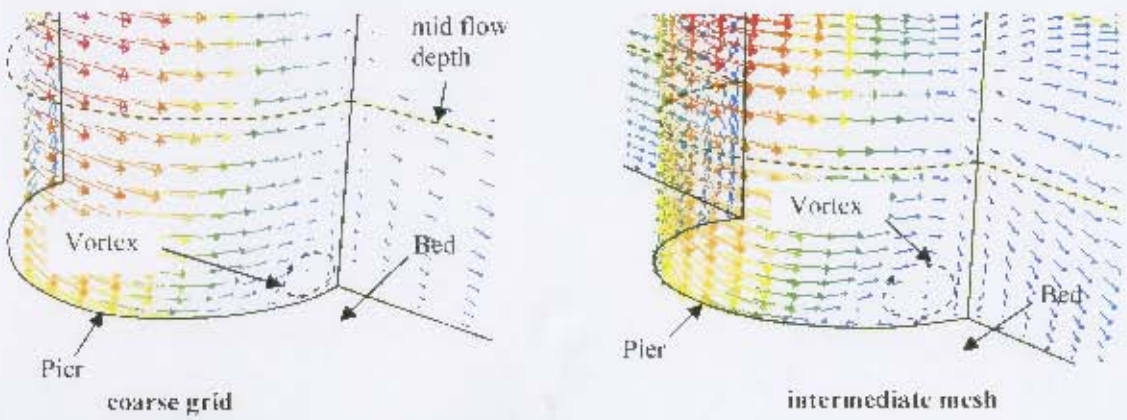

Figure 6-7a: Flow pattern in the lee of the pier

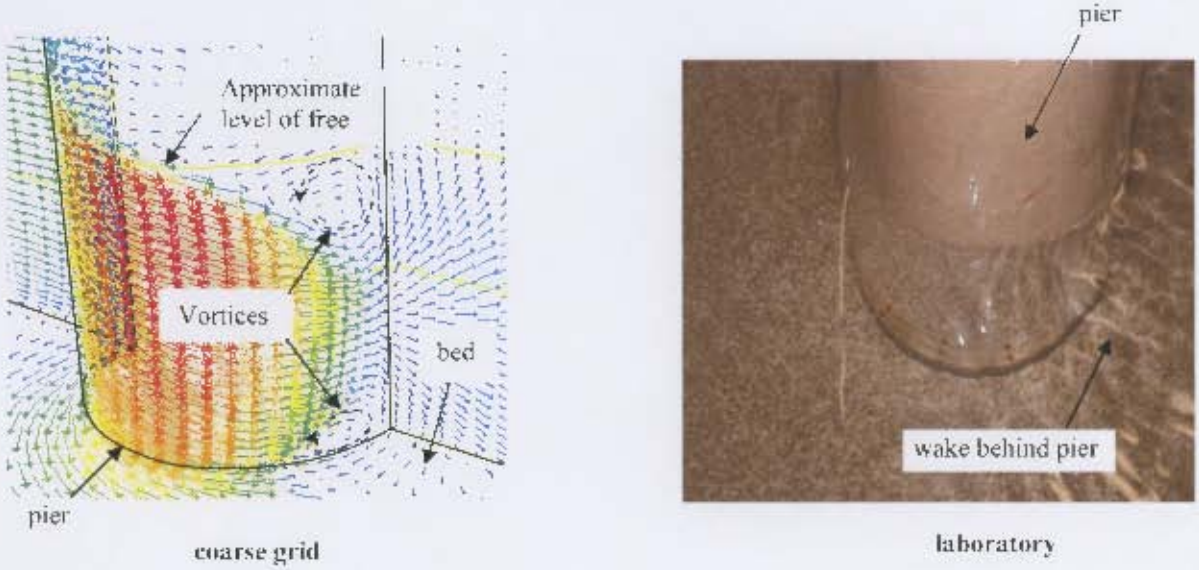

Figure 6-7b: Flow pattern in the lee of the pier

It is apparent from previous research and the predicted results above that it would be difficult to obtain a grid independent solution to the three dimensional flow around a circular pier. The computational demands required to fully resolve all the observed flow features, including the vortex street, the bow wave etc, is excessive. Depending on the conditions of flow, some of the features may play an important part in the scouring process e.g. for flows with small mean depths, the bow wave may interact with the horseshoe vortex at the base of the pier and affect the development of the scour hole. Consideration must therefore be given to the pertinent flow features when generating the grid and analysing the solution. The downflow and the horseshoe vortex at the base of the pier play a very important role in the scouring process. All the grids predicted these features and it was believed that they could be used for the simulations. However, consideration also had to be given to fact that the bed deformation models would work better with cells of smaller sizes. This, together with the fact that the fine mesh picked up more information in the lee of the pier, made it a better option for the scour simulations.

6.2 Scour prediction by different turbulence models

It has already been explained in Section 5.1.2.3 that the wall function approach was used for the modelling. The standard k-ε model and the RSM were examined using both standard and non-equilibrium wall functions. The flow modelled had a mean flow depth of 0.085m and a mean approach velocity of 0.2m/s (Experiment 2).

6.2.1 Flow fields and movability numbers

Figure 6-8 shows the velocity vector fields obtained for the RSM and standard k-ε models with both standard and non-equilibrium wall functions.

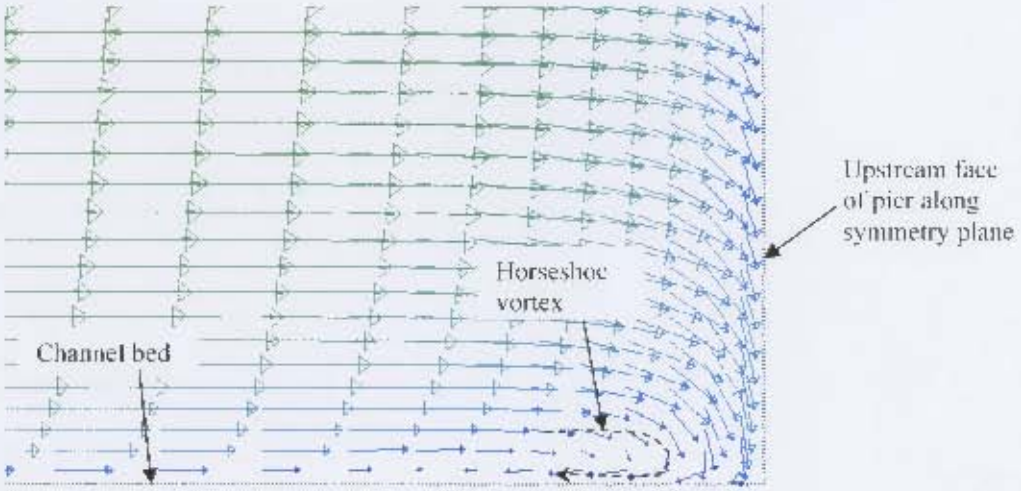

k-ε - standard wall functions

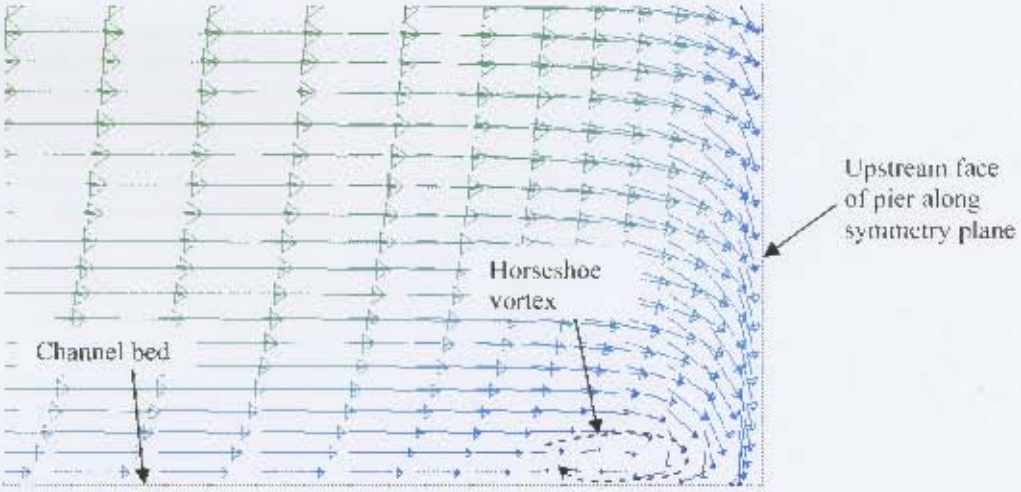

k-ε - non-equilibrium wall functions

Figure 6-8a: Velocity fields predicted by different turbulence models in front of pier

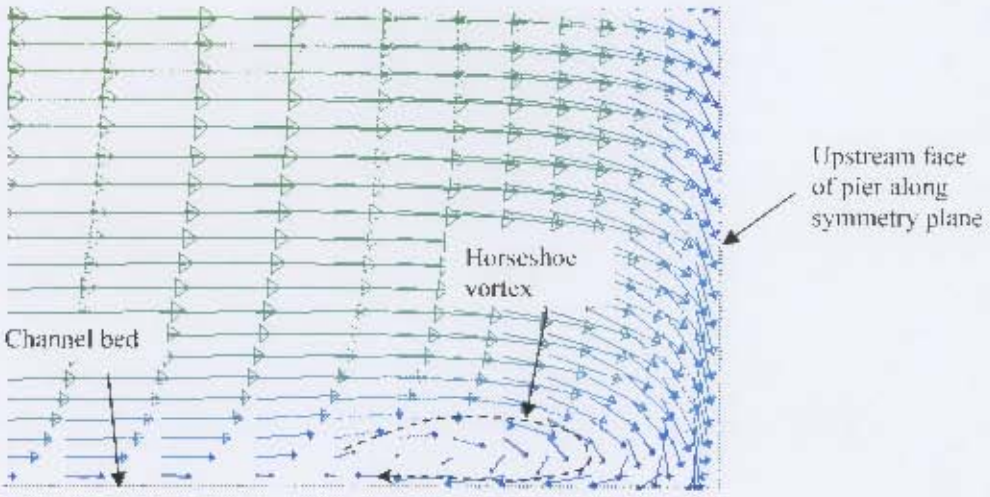

RSM - standard wall functions

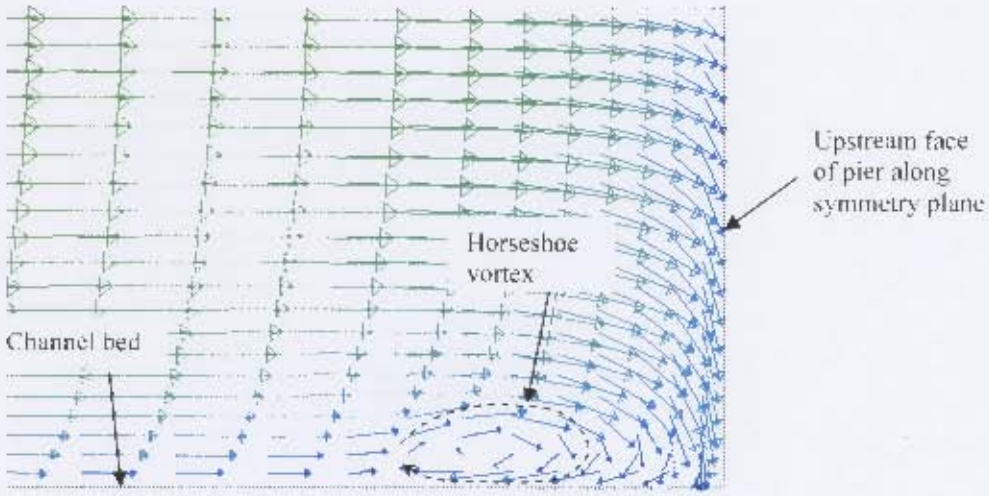

RSM – non-equilibrium wall functions

Figure 6-8b: Velocity fields predicted by different turbulence models in front of pier

The difference between the standard and non-equilibrium wall functions is slightly evident in each case. The non-equilibrium wall functions seem to produce stronger vortices than the standard wall functions. The RSM model with non-equilibrium wall functions appears to produce a stronger vortex and so appears to be a good candidate for use in scour prediction. Unfortunately, a look at the Movability Numbers predicted by the model (see Figure 6-9) indicate scouring in regions where scour was not observed in the laboratory.

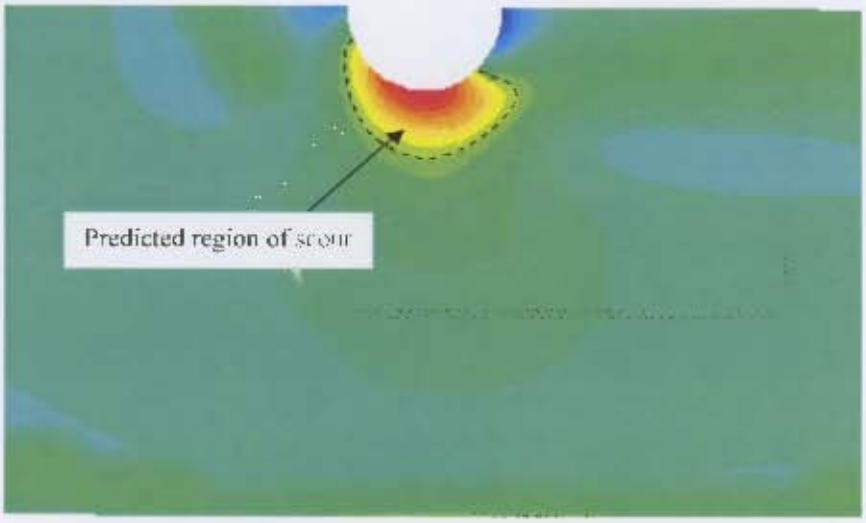

k-ε - standard wall functions

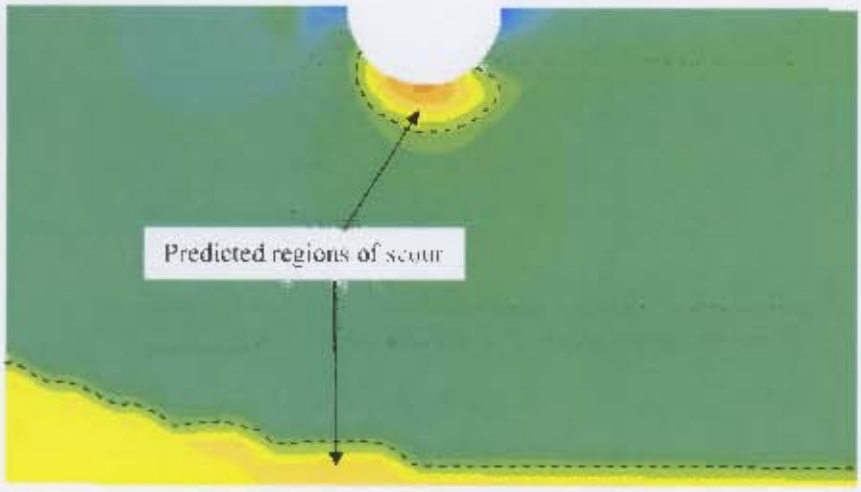

k-ε - non-equilibrium wall functions

Figure 6-9a: Movability Numbers predicted by k-ε model within the vicinity of the pier

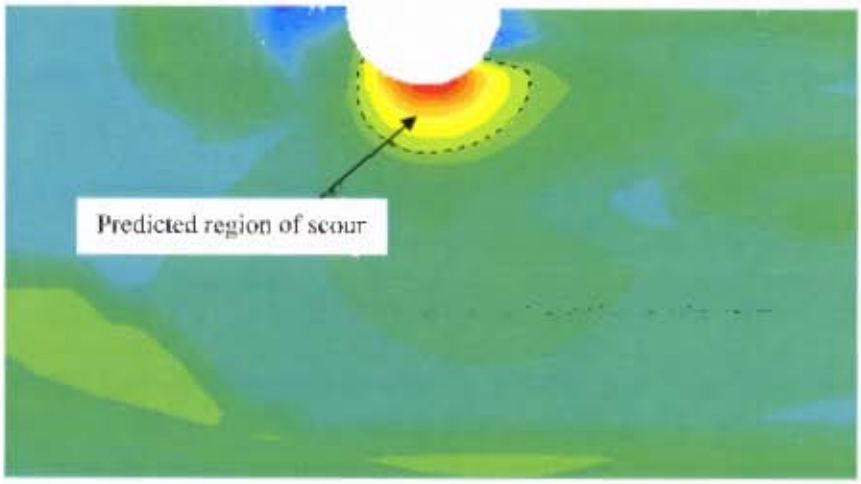

RSM - Standard wall functions

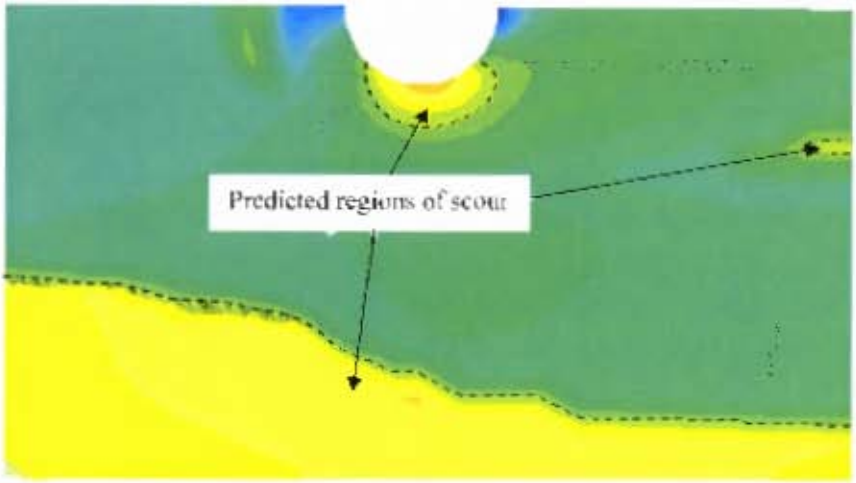

RSM - non-equilibrium wall functions

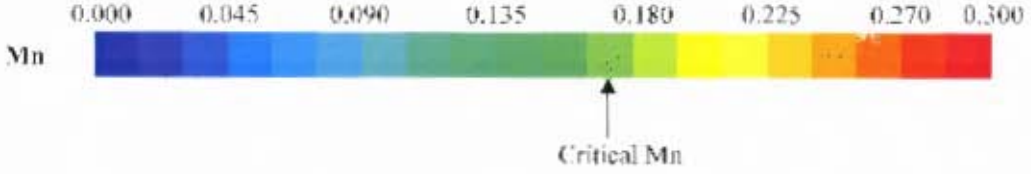

Figure 6-9b: Movability Numbers predicted by RSM within the vicinity of the pier

As can be seen in Figure 6-9 all the models predict an increase in Mn near the side walls of the channel. Even though there was a general increase in the Mn, the standard wall functions gave values that implied that there was no scour near the side walls. The non-equilibrium wall functions on the other hand predicted scouring near the side walls. This was not observed in the physical experiment and so the use of functions sensitised to pressure gradients (non-equilibrium functions) did not appear to be reasonable within this region. However, non-equilibrium conditions exist within the pier vicinity and the flow is influenced to a large extent by pressure gradients. The appropriate method to use close to the pier would therefore be to employ non-equilibrium functions. The decision was made to try both the standard and non-equilibrium functions by restricting bed deformations to the region just close to the pier. Unfortunately, the solution obtained for Experiment 1 predicted scouring from the side wall to regions close to the pier and made it impossible to define a restricted area within which deformation would be allowed (see Figure 6-10). An alternative solution would be to increase the width of the side channel to reduce the influence of the converging flow due to the constriction. This approach would however require extra computational power.

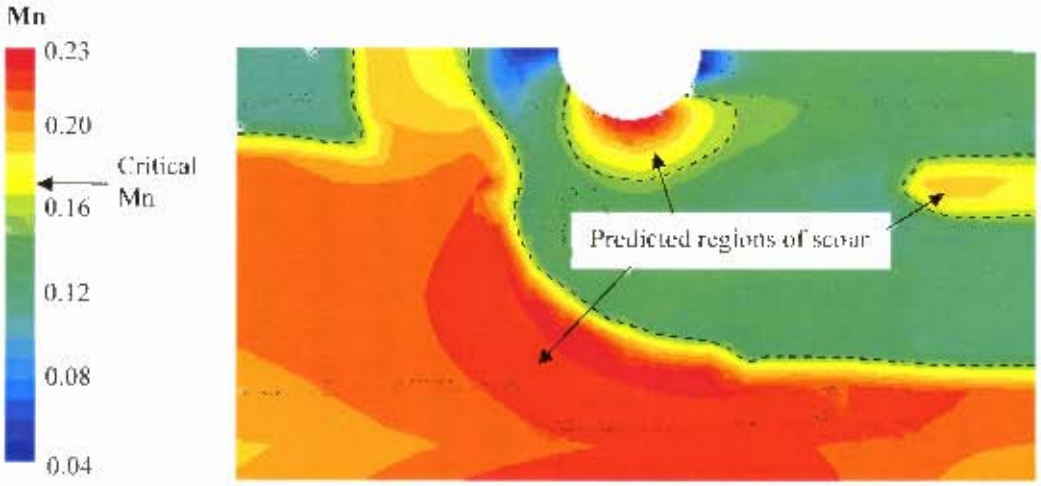

Figure 6-10: Movability Numbers predicted by RSM with enhanced wall functions for Experiment 1

It was also noted that Movability Numbers at the first point of flow separation upstream of the pier were relatively high. The Mn values were quite close to the critical value implying that scouring would have occurred in this region had the flow been any stronger. Scouring was not observed at this location in the physical model. In general, the standard k-ε model predicted slightly larger movability numbers at the pier than the RSM. Salaheldin *et al.* (2003) found that the k-ε models overestimated the velocity field near the bed whereas the RSM gave satisfactory results.

6.3 Modelling scour hole evolution

6.3.1 Mesh adaptation

The mesh adaptation function that was written was applied to a $1m^3$ cube with a coarse mesh to examine if it did indeed worked in the manner intended. Results for the different ratios (0.1, 0.3 and 0.45) that were tried are shown in Figure 6-11. The interior nodes have not been shown as the mesh would be difficult to make out.

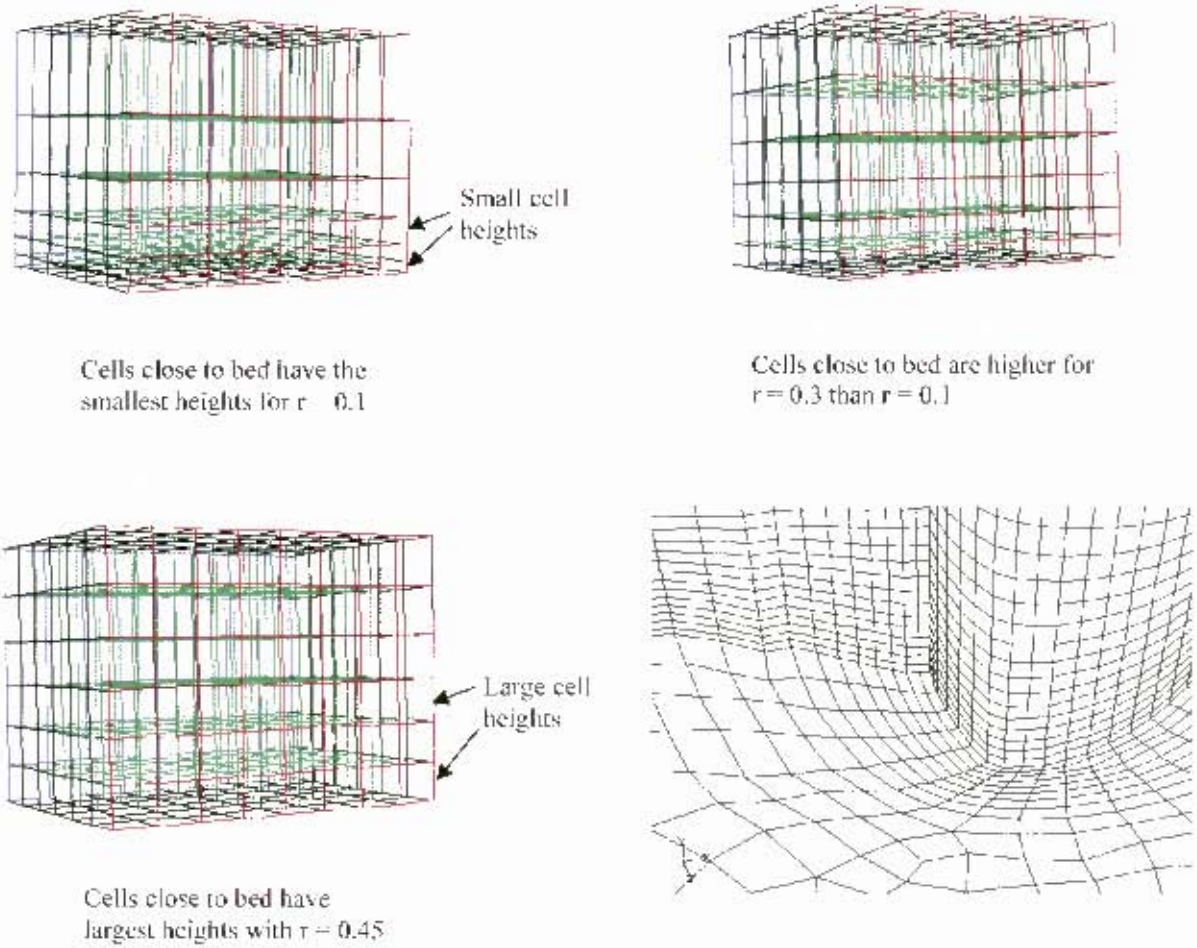

Figure 6-11: Illustration of mesh adaptation for different ratios

The mesh adaptation routine worked well for the cube. The case was a little different for the actual domains due to the units that were being used for the modelling. The function that was written was designed to identify grid nodes with the same horizontal (x-z) coordinates and store them in an array. It became apparent that the precision of the node coordinates changed upon importation into FLUENT e.g. two nodes that were supposed to have the same horizontal coordinates could have z values of 0.12564798 and 0.12564635. As a result, the routine had problems identifying nodes on the same vertical line and did not work so well. A simple solution to the problem was to examine the imported nodes and truncate the coordinates to an appropriate number of decimal places. It appears that there is no direct method for truncating decimals in C.

This was thus achieved by multiplying the coordinates by appropriate factors (e.g. 100, 1000, etc) and storing the results as an integers. This effectively cut off the remaining unwanted digits. Unfortunately, the finer the mesh, the more difficult it is to find an appropriate factor. Since the nodes are much closer, a greater degree of accuracy (number of decimal places) is required to identify each node on a vertical line. As soon as the level of accuracy required goes beyond the tolerance level of importation, the problem is no longer a trivial one. There was therefore a limit on the level to which the grids being generated could be fined up.

6.3.2 Scour hole evolution

A comparison is made here between the evolution of the scour hole in the laboratory and that predicted by the model. In the laboratory, scouring generally started along the sides of the pier and migrated quickly upstream. Figure 6-12 shows the scour depths along the sides of the pier during the first 6 hours of Experiment 1. After 5 minutes, the maximum scour depth was about 19mm and occurred at an angle of 30° to the plane of symmetry. The next largest scour depth was at 60° to the symmetry plane and was about 16mm. This was followed by depths of 12mm and 6mm at 90° and 0° respectively. The trend in the relative deepness of the scour hole at the different angles continued until after about 216minutes into the experiment where the depth of the hole at 0° became larger than that at 90°. Patterns similar to these were noted in the numerical model.

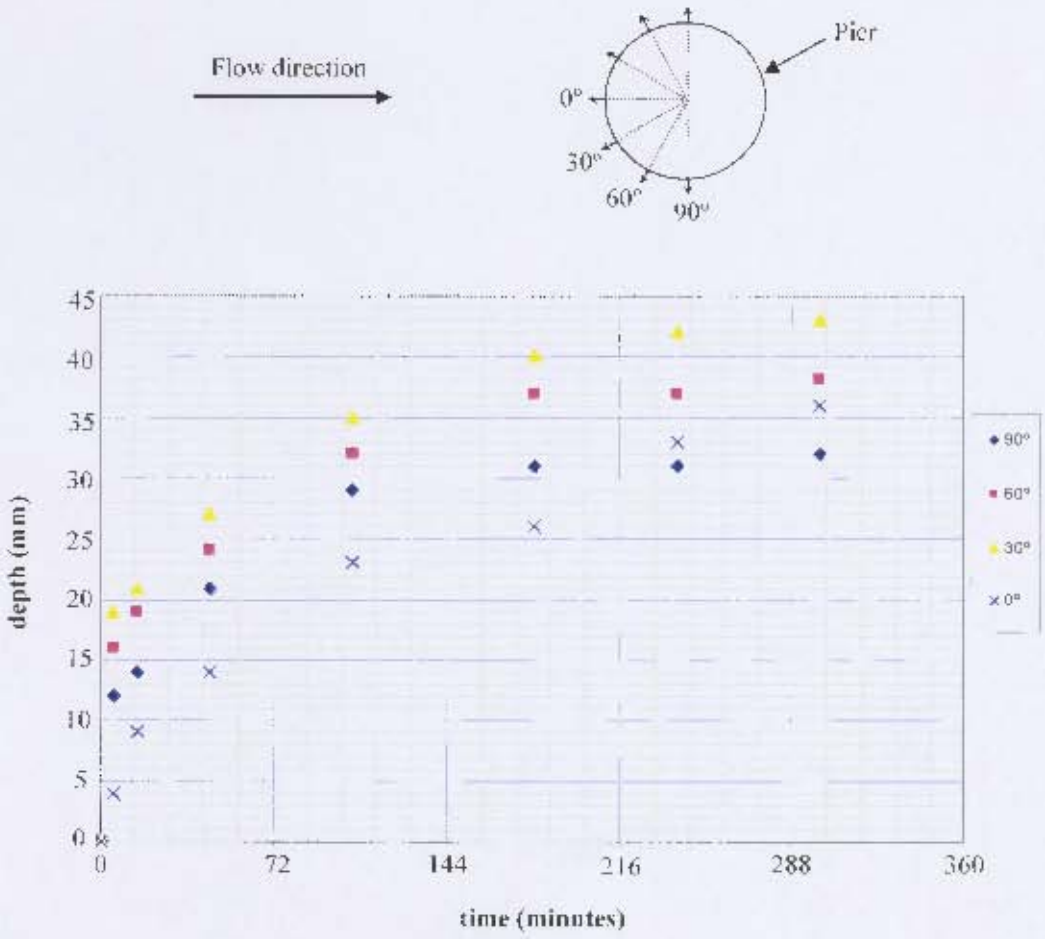

Figure 6-12: Evolution of scour hole near the pier at 0°, 30°, 60° and 90° (physical model)

The colours in Figure 6-13 illustrate the relative depths on the bed predicted by the numerical model for Experiment 1 using the intermediate grid. The solution was obtained using the standard k-ε model with standard wall functions and the linear relationship for bed deformation. The colours vary from red to deep blue which correspond to the highest and lowest elevations respectively. Scouring did in fact start from the sides and migrate upstream. The nature of the migration upstream was however not the same as that observed in the physical model. The numerical model did not predict scour at the symmetry plane (0°) when the maximum scour depth was at 20mm (See 6.13d). In the physical model however, the depth at the point (0°) was already greater than 6mm when the maximum scour depth was at 20mm. Also, the maximum scour depth at this point occurred at about 60° instead of 30° (Figure). This trend persisted for a while before the maximum depth eventually shifted to the 30° position. It can be noted from Figure 6-13 that the scour depth at the 90° mark was greater than that at the symmetry plane but eventually became smaller. This crossover actually occurred when the maximum scour depth was about 45mm (at 30°) which is quite close to the physical results, where the crossover occurred when the maximum scour depth was approximately 42mm (also at 30°).

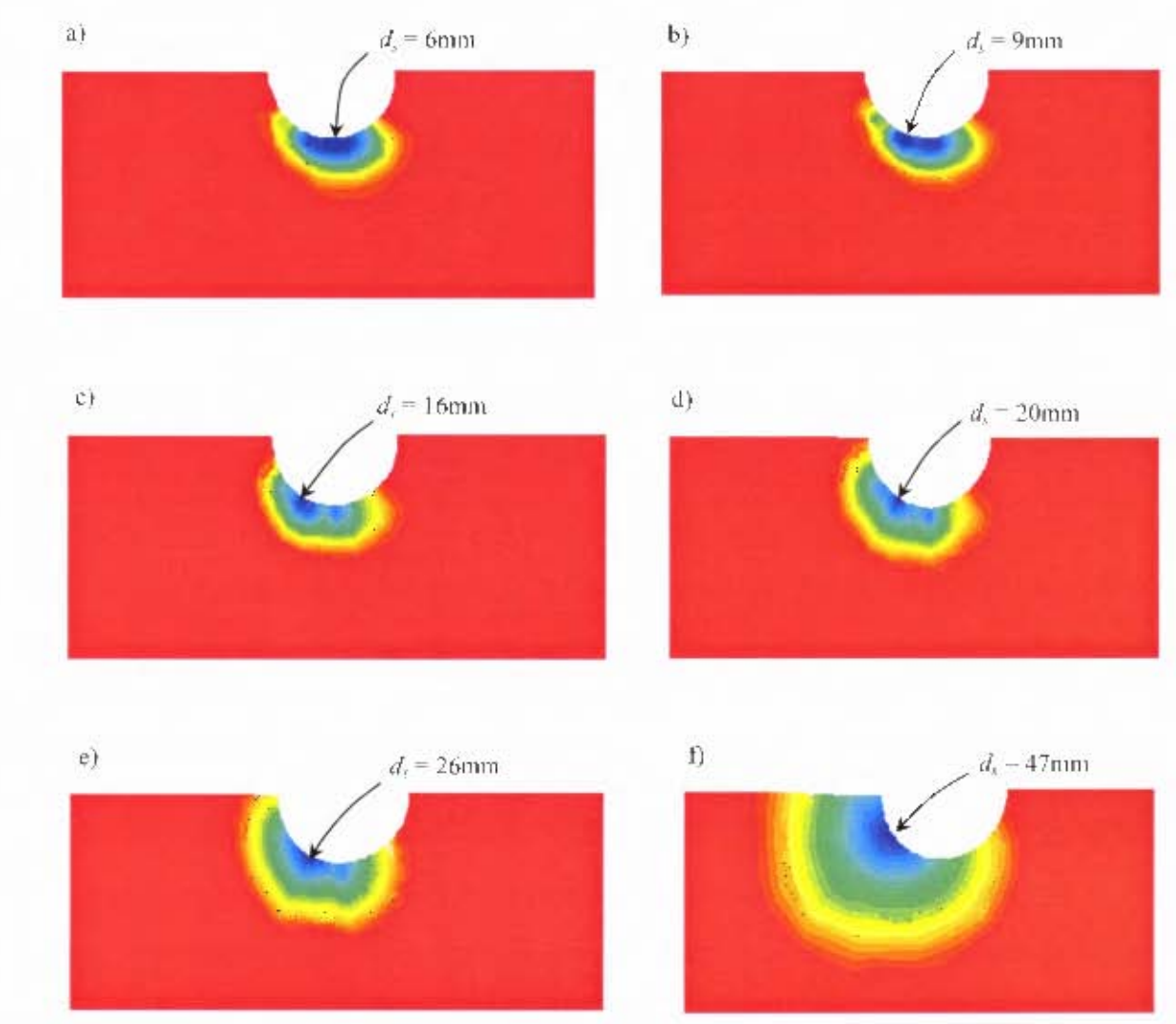

Figure 6-13: Evolution of scour hole predicted by numerical model

The scour hole stopped advancing once all the scour potentials had become equal to or less than zero. Figure 6-14 shows the bed Movability Numbers for the simulated equilibrium scour hole (Experiment 1). It is clear that the Movability Numbers within the scour hole are much lower than the critical value of 0.17 for a flat bed. It is thus easily discerned that the scour potential values were zero or less after the application of the slope correction factor. The region sloping upwards along the immediate side of the pier has Movability Numbers between 0.14 and 0.16. The slope however is in a direction opposite to that of the flow and so the critical Movability Number for the region will generally be larger than 0.17.

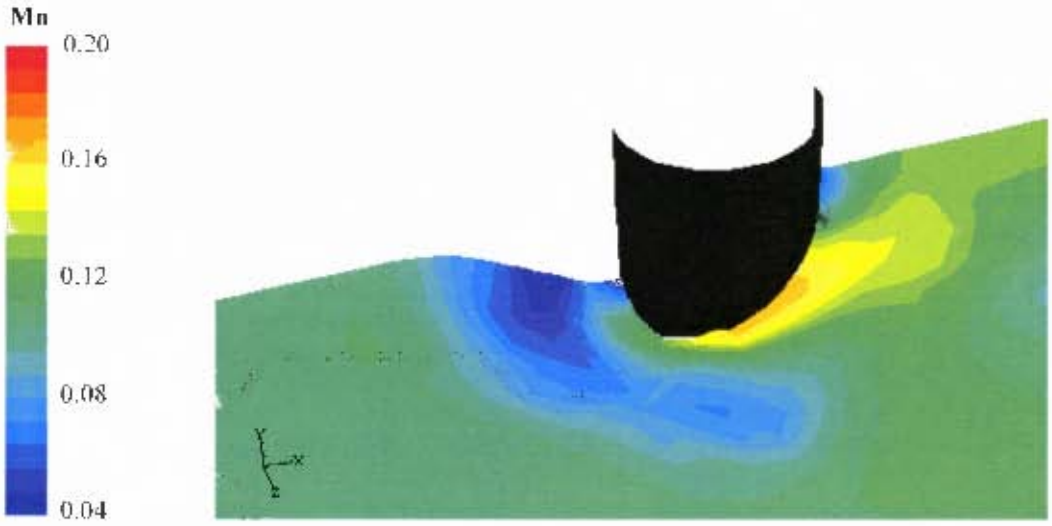

Figure 6-14: Movability Numbers at equilibrium scour hole

The algorithm used to perform the simulations was structured so that the behaviour of the predicted maximum scour depth would mimic the profile of observed maximum scour depths with time. This was done by reducing the rate of change of depth with the scour potential. The aim was to avoid the risk of distortion of the scour hole as it approached equilibrium. Figure 6-15 is a plot of the maximum scour depths at various boundary adjustment steps. The curve is similar to that described in Section 2.6.3.2 for clear-water scour. The main difference is that this curve rises to a definite value whereas the theoretical curve approaches the maximum scour depth asymptotically.

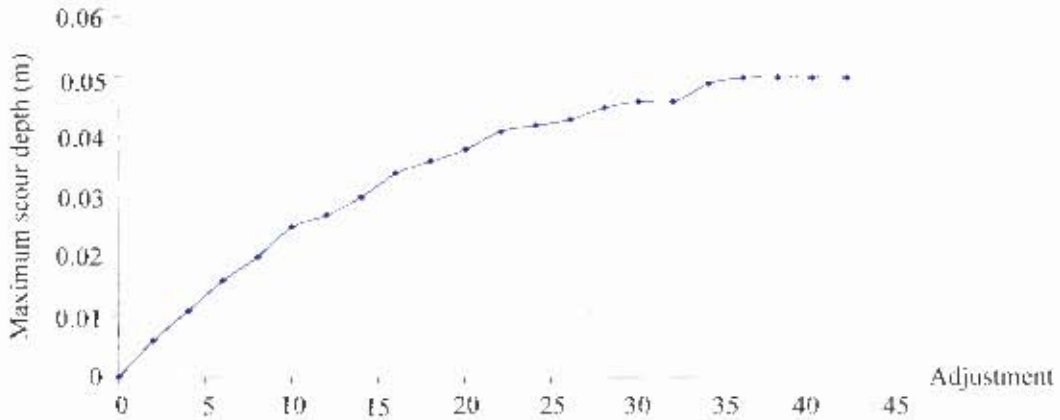

Figure 6-15: Variation of maximum scour depth with boundary adjustment

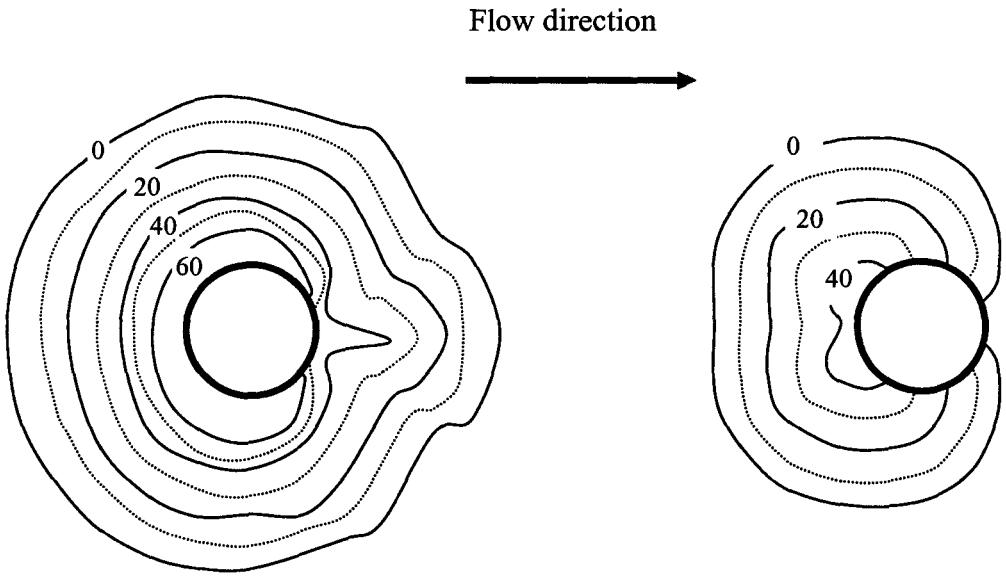

Contours of equilibrium scour hole - laboratory

Contours of equilibrium scour hole – FLUENT

Figure 6-16: Contours of equilibrium scour holes from laboratory experiment and numerical model (Experiment 1)

Figure 6-16 shows the contours of the equilibrium scour holes from both the physical and numerical models for Experiment 1. The numerical model under-predicted the maximum scour depth. The numerical model predicted a maximum scour depth of 50mm whereas the physical model gave a depth of 68mm. It took approximately 115hours of real time for the equilibrium scour hole to develop on the computer as compared with the 77hours for the physical experiment. The maximum scour depth predicted by the model occurred at an angle approximately 30° to the channel centreline. This was in agreement with the location of the maximum scour depth in the physical model. The shape of the scour hole predicted by the numerical model was however not in concurrence with that observed in the laboratory indicating that the estimation of the movability numbers at the bed was inaccurate. This was confirmed by results from the numerical simulations for the other experiments. For Experiments 2, 3 & 4, the model predicted scour depths of 50, 78 & 71mm whereas the actual scour depths were 61, 104 & 113mm respectively. Cunninghame's (2003) study has already been mentioned in Section 5.1.2.3. It looked at the accuracy of different modelling approaches in predicting the near-bed flow field using the standard k-ε model. Results from the study are shown in Figure 6-17. It can be noted that none of the modelling approaches that were assessed correctly predicted the shear stress at the bed (not even the standard wall functions with $30 < y^+ < 300$). It is evident that for an accurate scour hole to develop, scour prediction at the bed has to be accurate. In order for the developed model to be a viable option for scour prediction, a suitable modelling approach that will accurately predict the near-bed flow field needs to be found. Unfortunately, due to lack of time, the Reynolds stress model could not be assessed for its potential in predicting scour.

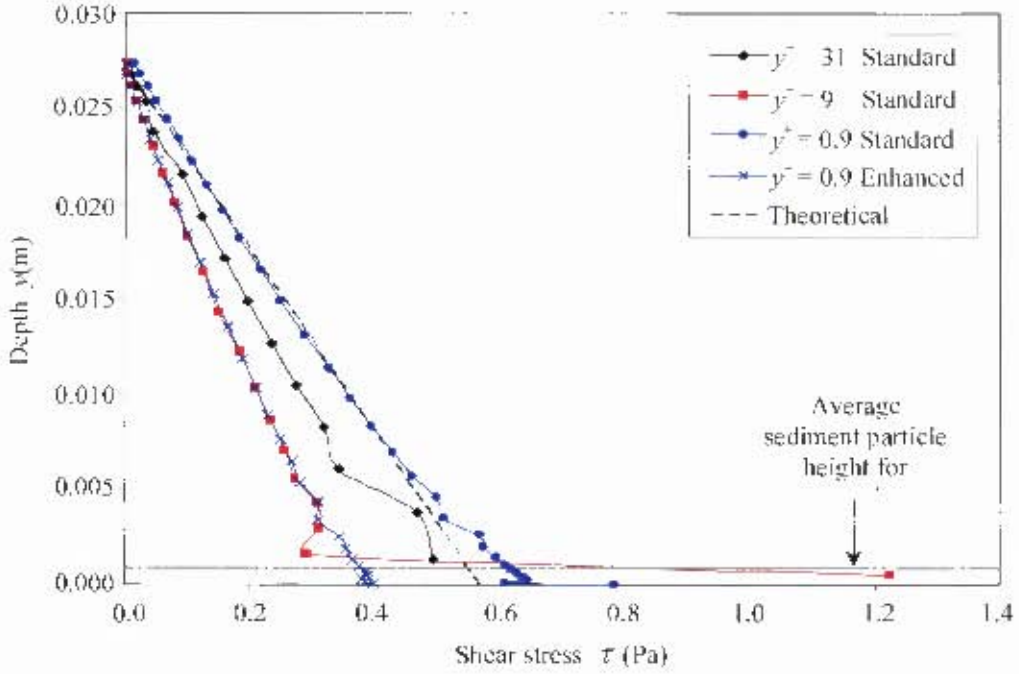

Figure 6-17: Distribution of shear stress with depth for different wall models (Cunninghame, 2003)

A look at the velocity field at angles 0° and 90° (Figure 6-18) indicate that even though the model picks up the horse shoe vortex in front of the pier, the vortex does not wrap around the pier and so its effects are not felt along the sides and the back of the pier. This could explain why the extent of the scour hole does not extend further behind the pier. Unger & Hager (2005a) found that the horseshoe vortex became noticeable only after about 10 minutes into their experiments. It is believed that if the scour hole in the simulations had developed correctly, the characteristics of the horseshoe vortex would be different.

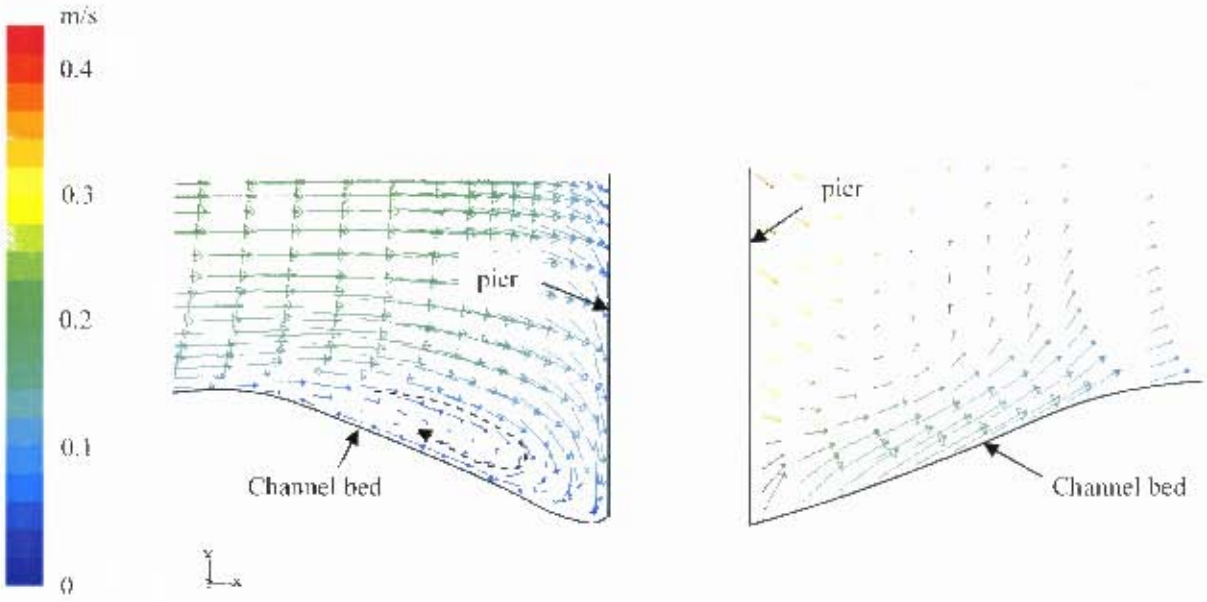

Figure 6-18: Velocity vector fields at symmetry plane (upstream) and 90° to the symmetry plane

It took longer for the scour hole to develop in the case of the exponential deformation model than for the linear model. It took approximately 96 hours of real time to attain a scour depth of 44mm for experiment 1 whereas it took only 90 hours using the linear relationship. This was expected as the relative movement between the nodes for the exponential model was expected to be larger than that for the linear model. The results obtained using the exponential relationship for bed deformation did not differ by much from those obtained using the linear relationship. This is shown in Figure 6-19. It shows the 'exponential' scour hole at an intermediate stage where it is at the same depth as the 'linear' scour hole. Both holes have almost the same shape and fairly similar extents. Unfortunately, during the simulation with the exponential model, the extents of the hole began to distort undesirably and the simulation had to be stopped. Continuing the simulation with a visibly wrong scour pattern and hence wrong flow field was pointless. The differences in the extents tend to indicate that the exponential relationship is more sensitive to the mesh than the linear relationship. It is believed that the exponential relationship would produce much better results for a finer mesh even though it might take much longer. Unfortunately, the current mesh adaptation model places a restriction on the level of refinement of the grid. The shapes produced by both models appear to confirm the belief that the problem with the scour estimation lay in the prediction of the flow field, and hence the Movability Numbers, at the bed.

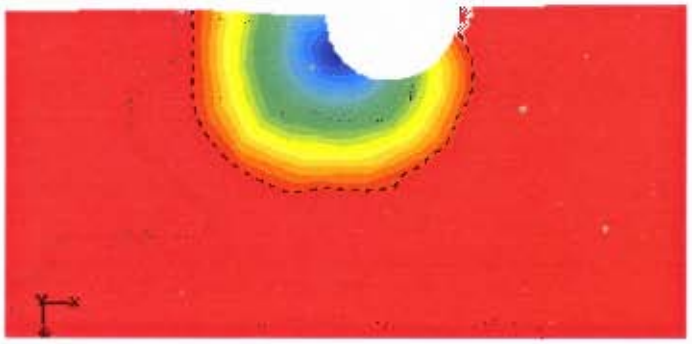

scour hole (d_s = 44mm) linear model

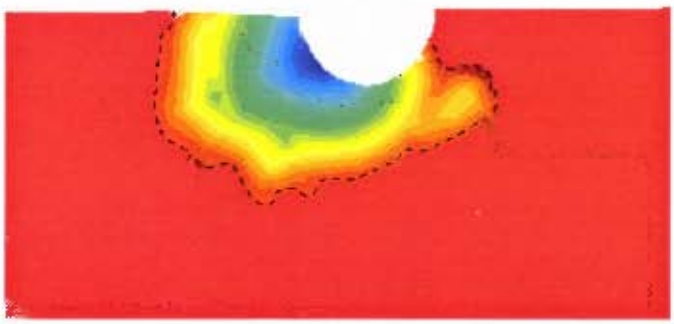

scour hole (d_s = 44mm) exponential model

---------- Extents of predicted scour hole

Figure 6-19: Scour holes predicted by linear and exponential deformation models

The numerical simulations were time consuming. Scour hole simulations typically took between 4 to 9 days per simulation. As a result, simulations could only be performed using the standard k-ε model. It is necessary that the use of other turbulence models (RSM in particular) be assessed to ascertain whether or not they can produce desirable results. Also ways of improving the mesh adaptation routine to allow the use of finer mesh must be found. Recommendations for future research into the use of FLUENT 6.2 for accurate clear-water scour prediction are presented in Chapter 8.

Chapter 7
Conclusions

The aim of the research was to develop an automated procedure for the estimation of local clear-water scour at bridge piers. The commercial CFD code FLUENT 6.2 was customized to achieve this aim. User-defined functions were written to reflect and control the scouring process. The functions were responsible for the deformation of the bed face mesh and the adaptation the domain mesh to the deformed boundaries. Scour estimation was based on the Movability Numbers at the bed. Nodes on the bed which had Movability Numbers greater than the expected critical values were displaced vertically and the location of the interior nodes were modified to maintain the integrity of the mesh.

The developed routine was examined against laboratory results from experiments that were run at the Civil Engineering hydraulics laboratory of the University of Cape Town. Only four laboratory experiments were performed due to time constraints. The resulting scour depth profiles were compared to those measured by Ahmed (1995) and Melville & Chiew (1999). The profiles were in good agreement the measured ones. They were however slightly different. Whereas the experimental profiles were consistently higher than that proposed by Ahmed (1995), they were consistently lower than the profiles suggested by Melville & Chiew (1999). The results were consistent and were considered to be good for model validation.

For the numerical simulations, grids with different degrees of refinement were assessed; namely a coarse grid, an intermediate grid and a fine grid. The standard k-ε model and the Reynolds stress model were employed for turbulence closure. The wall function approach was used for each simulation. Both standard and non-equilibrium wall functions were examined. It was found that the flow patterns for all the grids were largely similar. The main difference was that the fine grid predicted two vortices in the region behind the pier whereas the coarse and intermediate grids predicted only one. For the flat bed, the standard k-ε model predicted higher rates of scour than the Reynolds stress model but the general scour pattern was similar. The non-equilibrium wall functions appeared to generate stronger vortices in front of the pier but could not be used since they predicted scouring in regions on the bed where scouring was not observed in the laboratory.

Linear and exponential expressions for node movement were assessed for the bed modification. Initial results seem to indicate that both expressions are sensitive to the level of refinement of the grid. Hence, another dimension is added to the problem of attaining a grid independent solution. A grid that may offer an independent solution to the flow field may not necessarily offer an independent solution to the bed deformation. Preliminary results indicate that the resulting scour holes from both relationships are not much different in shape or extent. The exponential relationship appeared to be more sensitive to the grid refinement and also took longer than the linear relationship in predicting a particular scour hole. Both relationships will be more reliable when the mesh is relatively fine. Unfortunately, the current mesh adaptation routine places a restriction on the level of refinement of the grid.

Preliminary results from the numerical simulations are encouraging. The scour hole does in fact develop within the vicinity of the pier. The hole starts from the sides of the pier and migrates to the front as it grows deeper. It continues to grow deeper until all the Movability Numbers on the bed are eventually less than the corresponding critical Movability Numbers. The hole then stops growing and an equilibrium scour hole is deemed to have been attained. Even though the numerical model appears to pick up some of the essential patterns in the development of the scour hole, it is evident that the scour hole that develops is inaccurate. This is most likely due to inaccurate estimation of the bed Movability Numbers. The modelling approaches employed need to be reviewed to improve the accuracy of the model.

There is considerable promise in the developed model. Once a trustworthy approach for estimating the bed Movability Numbers is found, this option for scour estimation will be a very useful alternative given the current crop of high end machines that are available.

Chapter 8
Recommendations for future research

It is evident that the Movability Number approach is a viable option for scour prediction. It has been shown that commercial CFD codes with adequate flexibility and functionality may be adapted for use with this approach. The use of FLUENT 6.2 with this approach has been demonstrated. It is however subject to limitations. Results produced by the model are not very satisfactory but do indicate a considerable amount of potential in the approach. The following recommendations are given for future research:

- There is the need for exploration into the appropriate modelling approach that will accurately predict the scour potential values on the bed. Cunninghame (2003) studied various modelling approaches for flow in an infinitely wide channel using the k-ε model and found that standard functions with wall cells having a $y^+ = 0.9$ gave the best prediction of the shear stress profile followed by standard wall functions with $y^+ = 31$. The predicted values at the bed were however not the same as the theoretical value. Also, the conditions that were modelled were different from the flow conditions that develop within the vicinity of the pier. It is therefore suggested that a detailed study should be performed on the effectiveness of different modelling approaches in predicting the flow fields within the vicinity of the pier for both flat bed and scour hole scenarios.

- The current mesh adaptation routine places a restriction on the degree to which a mesh may be refined. The bed deformation models are dependent on the level of refinement of the mesh at the regions where scour is predicted. It is recommended that different methods of modifying the mesh be found to permit further refinement of the mesh within the near-pier region.

- Investigations into the possibility of using non-equilibrium wall functions must be performed. Ways of restricting their influence on the bed to the near-pier region must be found. This will enable their use in scour prediction and provide information on whether or not they produce better results than the standard wall functions.

- The entire domain must be modelled without applying the symmetry condition. It is evident that the symmetry condition affects the nature of the flow behind the pier. However, it is uncertain how this affects the flow upstream of the pier. A detailed study should be carried out on the influence of the symmetry condition on flow prediction. The study should be able to confirm if the use of the symmetry condition is justified.

- Finally, the maximum amount of deformation per stage and its corresponding scour potential value are specified by the user. An investigation into the optimum maximum deformation and its corresponding scour potential value which yield the best results needs to be performed. This will serve as a guide for future users who wish to use the developed approach for scour prediction.

References

Ackers P & White WR (1973). "Sediment Transport: New Approach and Analysis." *J. Hydr. Div. ASCE*, Vol. 99, HY11, pp. 2041 – 2060.

Ahmed F (1995). "Flow and erosion around bridge piers." PhD dissertation, University of Alberta, Canada.

Ahmed F & Rajaratnum N (1998). "Flow around Bridge Piers." *J. Hydr. Engrg.*, ASCE, Vol. 124, No. 3, pp. 288 – 300.

Ali KHM & Karim O (2002). "Simulation of flow around piers." J. *Hydr. Res.*, IAHR, Vol. 40, No. 2, pp. 161 – 174.

Armitage NP (2002). "A unit stream power model for the prediction of local scour." PhD dissertation, University of Stellenbosch, South Africa.

Armitage N & McGahey C (2003). "A unit stream power model for the prediction of local scour in rivers." *Water Research Commission of South Africa*, Report No. 1098/1/03, ISBN 1-86845-955-1, Pretoria, South Africa.

Armitage N & McGahey C (2004). "Scour prediction using the mobility number criteria for incipient motion." *Proc. Second International Conf. on Fluvial Hydraulics*, River Flow 2004, Vol. 1, pp. 511-519.

Bagnold RA (1960). "Sediment Discharge and Stream Power." US Geol Survey Circular 421, 23 pages.

Boussinesq J (1877). *"Essai sur la théorie des eaux courantes."* Mémoire présentés par divers savants a l'Académie de l'Institut de France, Vol 23. In Rouse, 1938.

Breusers HNC & Raudkivi AJ (1991). "Scouring." IAHR Hydraulic Structures Design Manual 2, A.A. Balkema, Netherlands.

Brooks NH (1963). Discussion of "Boundary Shear Stresses in Curved Trapezoidal Channels." by Ippen A.T. and Drinker P.A., *J. Hydr. Engrg.*, ASCE, Vol. 89, No. HY3, pp. 327 – 333.

Chabert J & Engeldinger P (1956). "Etude des Affouil-Lements antour des Piles des Ponts." Laboratoire National d'Hydraulique, Chanton, France. In Raudkivi, 1998.

Chadwick A, Morfett J & Borthwick M (2004). "Hydraulics in Civil and Environmental Engineering." 4th Edition, Spoon Press, London, UK.

Chanson H (2004). "The Hydraulics of Open Channel Flow: An Introduction." 2nd Edition, Elsevier, Oxford, UK.

Chapman DR (1979). "Computational Aerodynamics Development and Outlook." *AIAA J.*, Vol. 17, pp. 1293 – 1313.

Chien N & Wan Z (1999). "Mechanics of sediment transport." ASCE Press, USA.

Chitale SV (1962). Discussion of "Scour at Bridge Crossings." by Laursen E.M. *Trans.*, ASCE, Vol. 217, Part I, pp. 191 – 196.

Chow VT (1959). "Open channel hydraulics". McGraw-Hill, New York.

Cunninghame, ME (2003). "Computational Fluid dynamics modelling of scour around engineering structures in rivers." BSc(Eng) thesis, University of Cape Town, Rondebosch, South Africa.

Cunninghame ME (2005). "Numerical modelling of local scour in rivers using FLUENT 6.2." MSc (Eng) dissertation, University of Cape Town, South Africa.

Dargahi B (1990). "Controlling Mechanism of Local Scouring." *J. Hydr. Engrg*, ASCE, Vol. 116, No 10, pp. 1197 – 1214.

Ettema R (1980). "Scour at Bridge Piers." *Report No. 216*, School of Engrg., University of Auckland, Auckland, New Zealand.

Engelund F & Hansen E (1967). "A Monograph on Sediment Transport." Tecknish Forlag, Copenhagen, Denmarkt.

Ferziger JH & Perić M (1999). "Computational Methods for Fluid Dynamics." 2nd Edition, Springer-Verlag, Germany.

Fletcher CAJ (1991). "Computational Techniques for Fluid Dynamics." Vol. I, 2nd Edition, Springer-Verlag, Germany

Fluent (2005). "Fluent Users' Guide." Fluent Inc., UK.

Fortier S & Scobey FC (1926), "Permissible Canal Velocities." *Trans.*, ASCE, Vol. 89.

French RH (1994). "Open-Channel Hydraulics." International Edition, McGraw-Hill Inc.

Gambit (2004). "Gambit 2.2: User's Guide." Fluent Inc., UK.

Garde RJ, Raju KGR & Kothyari UC (1993). "Effect of unsteadiness and stratification on local scour." International science publisher, NY, USA.

Girvan R (2003). "Go with the flow." Scientific Computing World, March/April Issue
http://www.scientific-computing.com/scwmarapr03cfd_girvan.html
Last accessed: 15/11/2006.

Govers G (1987). "Initiation of Motion in Overland Flow." *Sedimentology*, No. 34, pp 1157 – 1164.

Graf WH (1995). "Local scour around piers." *Annu. Rep.*, Laboratoire de Recherches Hydrauliques, Ecole Polytechnique Federale de Lausanne, Lausanne, Switzerland, B.33.1 – B.33.8.

Graf WH (1998). "Fluvial Hydraulics: Flow and transport processes in channels of simple geometry." John Wiley & Sons, UK.

Hjulstrom F (1935). "The morphological activity of rivers as illustrated by River Fyris." *Bulletin of the Geological Institute*, Uppsala, 25:3.

Hoffmans GJCM & Verheij HJ (1997). "Scour Manual." A.A. Balkema, Netherlands.

Jain SC (1981). "Maximum clear-water scour around circular piers." *J. Hydr. Engrg*, Vol. 107, No.5.

Jang DS, Jetli R & Acharya S (1986). "Comparison of PISO, SIMPLER, and SIMPLEC Algorithms for the Treatment of the Pressure-Velocity Coupling in Steady Flow Problems." *Numer. Heat Transfer*, Vol. 19, pp 209 – 228.

Johnson DA & Coakley TJ (1990). "Improvements to a non-equilibrium algebraic turbulence model." *AIAA J.*, Vol. 28, pp. 2000 – 2003.

Julien PY (2002). "River Mechanics." Cambridge University Press, UK.

Knoros VS (1958). "Non-scouring Velocity for Non-cohesive Soil and its Application." *Proc.*, Soviet National Hydrology Institute, Vol. 59. (In Russian)

Kothyari UC, Garde RJ & Raju KGR (1992). "Temporal Variation of Scour around Circular Bridge Piers." *J. Hydr. Engrg.*, ASCE, Vol. 118, pp. 1091-1106.

Kothyari UC & Raju KGR (2001). "Scour around spur dikes and bridge abutments." *J. Hydr. Res.*, IAHR, Vol. 39, No 4, pp. 367-374.

Kramer H (1935). "Sand mixture and sand movement in fluvial model." *Trans.* ASCE, Vol. 100, pp 798 – 873.

Lam YM (2006) "Boundary Element Method :Brief.", Acoustic Research Centre, Web Resource.
http://www.acoustics.salford.ac.uk/student_area/bsc3/computer_simulation/Boundary%20Element%20Method.pdf
Last accessed: 16/11/2006

Lane EW (1953). "Progress Report on Studies on the Design of Stable Channels by the Bureau of Reclamation." *Proc. ASCE*, Vol. 79, No. 280.

Launder BE & Spalding DB (1972). "Lectures in mathematical models of turbulence." Academic, London. In Salaheldin *et al.*, 2004.

Laursen E.M. (1962). "Scour at Bridge Crossings." *Trans.*, ASCE, Vol 127, part 1, pp. 166-209.

Le Méhauté (1976). "An Introduction to hydrodynamics & Water waves." Springer-Verlag New York Inc, New York, USA.

Li B (1959). "Calculation of Threshold Velocity of Sediment Particles." *J. Sed. Res.*, Vol. 4, No. 1, pp. 71 -77. (In Chinese)

Lin GH (1993). "Study on the Local Scour around Cylindrical Bridge Piers (in Chinese)." MSc Dissertation, Feng-Chia University, Taichung, Taiwan, R.O.C.

Liu HK (1957). "Mechanics of Sediment-Ripple Formation." *J. Hydr. Div.*, ASCE, Vol 84, HY5, paper 1197, pp. 1-23.

Lyons S (2003). "An investigation into the initiation of local scouring around rectangular 'long' contractions." MSc (Eng) dissertation, University of Cape Town, South Africa.

Massey BS & Smith JW (1998). "Mechanics of Fluids." 7th Edition, Spoon Press, UK.

Mavriplis DJ (1996). "Mesh Generation and Adaptivity for Complex Geometries and Flows." *Handbook of computational fluid dynamics*, Edited by Peyret R., Academic press.

May RWP, Ackers JC & Kirby AM (2002). "Manual on scour at bridges and other hydraulic structures." CIRIA C551, London, UK.

McGahey C (2001). "A computational fluid dynamics model for sediment movement based on the unit stream power approach." MSc (Eng) dissertation, University of Cape Town, South Africa.

Melville BW (1973). "Scour at Bridge Sites." *Report No. 104*, School of Engrg., University of Auckland, Auckland, New Zealand.

Melville BW & Raudkivi AJ (1977). "Flow characteristics in local scour at bridge piers." *J. Hydr. Res.*, Vol. 15, No. 4, pp. 373 – 380.

Melville BW (1984). "Live-Bed Scour at Bridge Piers." *J. Hydr. Engrg.*, ASCE, Vol. 110, pp. 1234-1247.

Melville BW (1997). "Pier and Abutment Scour: Integrated Approach." *J. Hydr. Engrg.*, ASCE, Vol. 123, No. 2, pp. 125-136.

Melville BW & Chiew YM (1999) "Time Scale for Local Scour at Bridge Piers." *J. Hydr. Engrg.*, ASCE, Vol 125, No. 1. Paper No. 16274, pp. 59-65.

Melville BW & Coleman SE (2000). "Bridge Scour." Water Resources Publications, LLC, Colorado, USA.

Migniot C (1968). "Etude des Proprietes Physiques de Differents Sediments Tres Fins et de Leur Comportement Sous des Actions Hydrodynamiques." *Houille Blanche*, Vol. 7, pp. 591 – 620.

Muzzammil M, Gangadharaiah T & Gupta AK (2004). "An Experimental Investigation of a Horseshoe Vortex Induced by a Bridge Pier." *Proc. ICE, WM*, Vol. 157, No. 2, pp. 109 – 119.

Nagata N, Hosada T, Nakato T, Muramoto Y (2005). "Three-Dimensional Numerical Model for Flow and Bed Deformation around River Hydraulic Structures." *J. Hydroscience & Hydraulic Engineering*, Vol. 20, No. 1, pp 113 – 125.

Nalluri C & Featherstone RE (2001). "Civil Engineering Hydraulics." 4th Edition, Blackwell Science Ltd, UK.

Nikuradse J (1933). "Stromungsgesetze in Rauben Rohren (Laws of turbulent pipe flow in rough pipes)." *VDI, Forschungsheft*, No. 361. In German; translated in NACA Tach. Memo No. 1292, 1950.

Ninomiya H & Onishi K (1991). "Flow analysis using a PC." Computational Mechanics Publications, CRC Press Inc., Southampton Boston, UK.

O'Connor & Robertson (2000). "Adhémar Jean Claude Barré de Saint-Venant." http://www-groups.dcs.st-and.ac.uk/~history/Mathematicians/Saint-Venant.html Last accessed: 15/11/2006.

Oliveto G & Hager WH (2002). "Temporal Evolution of Clear-Water Pier and Abutment Scour." *J. Hydr. Engrg*, ASCE, Vol. 131, No. 2, pp. 97-105.

Olsen NRB & Melaaen MC (1993). "Three-dimensional Calculation of Scour around Cylinders." *J. Hydr. Engrg.*, ASCE, Vol. 119, No. 9, pp. 1048-1054.

Olsen NRB & Kjellesvig HM (1998). "Three-dimensional numerical flow modelling for estimation of maximum local scour depth." *J. Hydr. Res.*, IAHR, Vol. 36, No. 4, pp. 579-590.

Olsen NRB (2000). "CFD Algorithms for Hydraulic Engineering." Department of Hydraulic and Environmental Engineering, The Norwegian University of Science and Technology, Report Ref ISBN 82-7598-044-5.

Peyret R (1996). "Handbook of computational fluid dynamics." Academic press, UK.

Potter MC & Wiggert DC (1997). "Mechanics of fluids." 2nd Edition, Prentice Hall.

Prandtl L (1925). "Über die Ausgebildete Turbulenz (On fully developed turbulence)." *Z. Angew. Math. Mech.,* Vol. 5, pp. 136 – 139 (in German).

Raudkivi AJ (1982). "Grundlagen des Sedimenttransports." Springer-Verlag.

Raudkivi AJ & Sutherland AJ (1982) *"Scour at Bridge Crossings."* Road Research Unit, National Roads Board, Wellington, New Zealand. Bulletin 54.

Raudkivi AJ (1986). "Functional trends of scour at bridge piers." J. Hydr. Engrg. ASCE, Vol. 112, No. 1, pp. 1- 13.

Raudkivi AJ (1998). "Loose Boundary Hydraulics." 4th Edition, A.A. Balkema, Rotterdam, Netherlands.

Reynolds O (1894). "On the dynamical theory of Incompressible Fluids and the Determination of the Criterion." *Phil Trans. A*, Vol. 186; Papers, Vol. 2, p 535.

Reynolds AJ (1974). "Turbulent Flows in Engineering." John Wiley & Sons.

Richardson & Davis (2001). "Evaluating Scour at Bridges." Hydraulics Engineering Circular 18, 4th Edition, US Department of Transportation, Federal Highway Administration, Publication No. FHWA NHI 01-001.

Richardson JE & Panchang VG (1998). "Three-dimensional simulation of scour-inducing flow at bridge piers." J. *Hydr. Engrg*, ASCE, Vol 124, No. 5, pp. 530 – 540.

Roache PJ (1982). "Computational Fluid Dynamics." Hermosa publishers, Albuquerque, New Mexico.

Rooseboom, A (1992). "Sediment Transport in Rivers and Reservoirs – A Southern African Perspective." Report No. 297/1/92 of the Water Research Commission of South Africa.

Rouse H (1938). "Fluid Mechanics for Hydraulic Engineers." McGraw-Hill Inc., New York, USA.

Salaheldin TM, Imran J & Chaudhry MH (2004). "Numerical modelling of three-dimensional flow field around circular piers." *J. Hydr. Engrg.*, ASCE, Vol. 130, No. 2, pp. 91-100.

Sargent RG (1998), "Verification and Validation of Simulation Models", Proceedings of the 1998 Winter Simulation Conference, pp 121 – 130.

Sarker Md A (1998). "Flow measurements around scoured bridge piers using acoustic-doppler velocimeter (ADV)." *Flow Meas. Instrum.*, Vol. 9, pp. 217 – 227.

Schlesinger *et al.* (1979), *"*Terminology for Model Credibility*"*, *Simulation*, 32, 3, pp. 103-104. As found in Sargent (1998)

Schlichting H (1979). "Boundary layer theory." 7th Edition, McGraw-Hill Book Co., New York, USA.

Schlichting, H & K Gersten (2000). "Boundary Layer Theory." Eighth edition, Springer-Verlag, Berlin, Germany.

Shaw CT (1992). "Using Computational Fluid Dynamics." Prentice Hall.

Shen HW, Schneider VR & Karaki S (1969). "Local scour around bridge piers." *J. Hydr. Engrg.*, Vol. 95, No. 6.

Shields A (1936). "Anwendung der Aenlichkeitsmechanik und der Turbulenzforschung auf die Geschiebebewegung." Mitteilungen der Preussischen Versuchsanstalt für Wasserbau und Schiffbau, Heft 26 (in German). English translation by WP Ott and JC van Uchelen, Hydrodynamics Laboratory Publication No. 167, Hydrodynamics Lab., California Institute of Technology, Pasadena.

Shih TH, Liou WW, Shabbir A & Zhu J (1995). "A new k-ε eddy-viscosity model for high Reynolds number turbulent flows – Model development and validation." *Comput. Fluids*, Vol. 24, No. 3, pp. 227 – 238.

Shvidchenko AB & Pender G (2000a). "Flume study of the effect of relative depth on the incipient motion of coarse uniform sediments." *Water Resources Research*, Vol. 36, No. 2, pp. 619 – 628.

Shvidchenko AB & Pender G (2000b). "Initial motion of streambeds composed of coarse uniform sediments." *Proc. Instn Civ. Engrs Water & Mar. Engrg*, 142, pp. 217 – 227.

Simons DB & Richardson EV (1966). "Resistance to Flow in Alluvial Channels." US Geological Survey Professional Paper 422-J.

Simons DB & Senturk F (1977). "Sediment transport technology." US Water Resources Publications, Fort Collins, Colorado.

Smith GD (1985). "Numerical solution of partial differential equations: finite difference methods." Oxford University Press, Oxford, UK.

Talapatra SC & Ghosh SN (1983). "Incipient Motion Criteria for Flow over a Mobile Bed Sill." *Proc. 2nd International Symposium on River Sedimentation*, Nanjing, China, pp. 459 – 471.

Tannehill JC, Dale AA & Pletcher RH (1997). "Computational Flud Mechanics and Heat Transfer." Taylor & Francis, Philadelphia, USA.

Unger J & Hager WH (2005a). "Spatial and temporal scour features of circular bridge piers." Paper submitted to XXXI IAHR Congress, September 2005, Seoul, Korea.

Unger J & Hager WH (2005b). Discussion of "The mean characteristics of horseshoe vortex at a cylindrical pier." by Muzzammil M & Gangadhariah T (2003), *J. Hydr. Res.*, Vol. 43, pp. 584 – 587.

Van Rijn LC (1984). "Sediment Transport, Part II: Suspended Load Transport." *J. Hydr. Engrg.*, ASCE, No. HY11.

Van Rijn LC (1986). "Sediment transport, part 1: bed load transport." *J. Hydr. Engrg*, ASCE, Vol. 112, pp. 433-455.

Van Rijn LC (1987). "Mathematical modelling of morphological processes in the case of suspended sediment transport." PhD dissertation, Delft University of Technology, Deflt, The Netherlands.

Van Rijn LC (1993). "Principles of sediment transport in rivers, estuaries and coastal seas." Aqua Publications, Netherlands.

Vanoni VA (1977). "Sedimentation Engineering." ASCE Manuals and Reports on Engineering Practice No. 54, *ASCE*, New York, USA.

Versteeg, HK & Malalasekera W (1995). "An Introduction to Computational Fluid Dynamics: The Finite Volume Method." Longman Group Limited, Essex, UK.

Weisstein EW (2005). *"Finite Volume Method."* From MathWorld--A Wolfram Web Resource, Wolfram Research, Inc.
http://mathworld.wolfram.com/FiniteVolumeMethod.html
Last accessed: 25/07/2005

Weisstein EW (2006). "Elementary Cellular Automaton." From MathWorld--A Wolfram Web Resource.
http://mathworld.wolfram.com/ElementaryCellularAutomaton.html
Last accessed: 16/11/2006.

Wesseling P (2001). "Principles of Computational Fluid Dynamics." Springer Series in Computational Mathematics, Vol. 29, Heidelberg Berlin.

White CM (1940). "The Equilibrium of Grains on the Bed of an Alluvial Channel." *Proc. Royal Society of London*, Series A, Vol. 174, pp. 332 – 338.

White FM (1991). "Viscous Fluid Flow." 2nd Edition, McGraw-Hill Inc., New York, USA.

Wikipedia (2006a). "FLOPS." From Wikipedia Encyclopedia, Web Resource.
http://en.wikipedia.org/wiki/Gflops
Last accessed: 16/11/2006.

Wikipedia (2006b). "Cellular Automaton." From Wikipedia Encyclopedia, Web Resource.
http://en.wikipedia.org/wiki/Cellular_automata
Last accessed: 16/11/2006.

Wikipedia (2006c). "Boundary Element Method." From Wikipedia Encyclopedia, Web Resource.
http://en.wikipedia.org/wiki/Boundary_element_method
Last accessed: 16/11/2006.

Wilcox DC (1993). "Turbulence Modeling for CFD." DCW Industries, Inc., La Cañada, CA.

Wolfstein M (1969). "The Velocity and Temperature Distribution of One-Dimensional Flow with Turbulence Augmentation and Pressure Gradient." *Int. J. Heat Mass Transfer*, Vol. 12, pp. 301-318.

Yakhot V & Orszag SA (1986). "Renormalization group analysis of turbulence I: Basic theory." *J. Sci. Comput.*, Vol. 1, No 1, pp. 1 – 51. In Salaheldin *et al.*, 2004.

Yalin MS (1972). "Mechanics of Sediment Transport." Pergamon Press, Oxford, UK.

Yang CT (1972). "Unit stream power and sediment transport." *J. Hydr. Div.*, ASCE, Vol. 98, HY10, 1805 – 1826.

Yang CT (1973). "Incipient motion and sediment transport." *J. Hydr. Div.*, ASCE, Vol. 99, HY10, pp.1679 – 1703.

Yang CT & Stall JB (1976). "Applicability of Unit Stream Power Equation." J. *Hydr. Div.*, ASCE, Vol. 102, HY5, pp. 559 – 568.

Yang CT (1996). "Sediment Transport: Theory and Practice." McGraw-Hill, Singapore.

Yanmaz AM & Altinbilek HD (1991). "Study of Time-Dependent Local Scour around bridge piers." *J. Hydr. Engrg.*, Vol. 117, No. 10, pp. 1247 – 1268.

Yen CL, Lai JS & Chang WY (2001). "Modelling of 3D flow and scour around circular piers." *Proc. Natl. Sci. Counc., ROC(A)*, Vol. 25, No. 1, pp. 17-26.

Zanke U (1978) "Zusammenhange zwischen Stromung und Sedimenttransport, Teil 1: Berechnung des Sedimenttransportes, -allgemeiner Fall-, Teil 2: Berechnung des Sedimenttransportes hinter befestigten Sohlenstrecken, -Sonderfall sweidimensionaler Kolk-." Mitteilungen des Franzius-Instituts der TU Hannover, Heft 47, 48.

Zeng, Zhaozen & Shangyi Wang (1963). "Study of Threshold Criteria for Granular Sediment." *Journal of Tianjin University*, pp. 19 – 40. (In Chinese).

Appendix
Sample user-defined functions

Mesh update routine

```
#include "udf.h"

DEFINE_GRID_MOTION(check, d, dt, time, dtime)
{
      /*Domain */
      int currentTimeStep;
      currentTimeStep = N_TIME;


      if ((currentTimeStep-1) % 400 == 0 && currentTimeStep > 2000)
      {

            Node *v; /*pointer to node*/
            Node *globalNodeID[20000]; /*to store global node IDs*/
            Node *uniqueGlobalNodeID[20000]; /*to store unique node IDs*/
            real nodes[20000][4]; /*to store face node coordinates*/
            real uniqueNodes[20000][2]; /*to store unique node coordinates*/
            int n = 0; /*counter*/
            int nn = 0; /*counter*/
            int ll = 0; /*counter*/
            int kk = 0; /*counter*/
            int count;  /*counter*/
            int count2; /*counter*/
            int mm = 0; /*counter*/
            int x, z, xx, zz, no, noo; /*counters*/
            int i, j; /*counters*/
            real t;
            int tt; /*index*/
            int l, lll; /*indices*/
            Node *ttt; /*index*/
            real ratio, lastLength, distance; /*parameters-exponential eqn*/
            real userRatio = 0.35;
            Thread *ct = DT_THREAD(dt); /*cell thread*/

            cell_t c;
            count = 0;


            begin_c_loop(c, ct)
            {
                  c_node_loop(c, ct,n)
                  {
                        v = C_NODE(c, ct,n);
                        /*store each node once*/
                        if (NODE_POS_NEED_UPDATE(v))
                        {
                              nodes[mm][0] = NODE_X(v);
                              nodes[mm][1] = NODE_Y(v) *100;
                              nodes[mm][2] = NODE_Z(v); nodes[mm][3] = 0;
                              globalNodeID[mm] = v;
                              NODE_POS_UPDATED(v);
                              count++;
                              mm++;

                        }
                  }
            }
            end_c_loop(c, ct)

            Message("no = %g\n", count);
```

```
/*sorting of id's according to which value is minimum*/

for (nn = 0; nn < count; nn++)
{
      x = nodes[nn][0]*170;    z = nodes[nn][2]*170;
      count2 = 0;

      /*read unique values*/
      for(kk = 0 ; kk < count; kk++)
      {
            xx = nodes[kk][0]*170;  zz = nodes[kk][2]*170; no = nodes[kk][3];

            if (xx == x && zz == z && no == 0)
            {
                  uniqueNodes[count2][1] = nodes[kk][1]; /*store y value*/
                  uniqueNodes[count2][0] = kk; /*store position*/
                  uniqueGlobalNodeID[count2] = globalNodeID[kk]; /*get
                  corresponding global node pointer*/
                        nodes[kk][3] = 1;/*1 for updated*/
                        count2++;
                  }
      }


      if(count2!=0)
      {
            /*sort uniqueNodes*/
            for(i = 0; i < count2 - 1; i++)
            {
                  for(j = 0; j < count2 - 1 - i; j++)
                  {
                        if (uniqueNodes[j+1][1] < uniqueNodes[j][1])
                        {
                              t = uniqueNodes[j][1];
                              tt = uniqueNodes[j][0];
                              ttt = uniqueGlobalNodeID[j];
                              uniqueNodes[j][1] = uniqueNodes[j+1][1];
                              uniqueNodes[j][0] = uniqueNodes[j+1][0];
                              uniqueGlobalNodeID[j]= uniqueGlobalNodeID[j+1];
                              uniqueNodes[j+1][1] = t;
                              uniqueNodes[j+1][0] = tt;
                              uniqueGlobalNodeID[j+1] = ttt;
                        }
                  }
            }


            ratio = exp(((uniqueNodes[count2-1][1] -
            uniqueNodes[0][1])/(count2 - 1))*(userRatio - 0.5)); /*ratio for
            mesh*/

            lastLength = (uniqueNodes[count2-1][1] - uniqueNodes[0][1]) * (1
            - ratio) / (1 - pow(ratio, (count2-1)));


            /*modify mesh according to the geometric progression*/
            for (i = 1; i < count2 - 1; i++)
            {
                  distance = lastLength * pow(ratio, (count2 - i - 1));

                  v = uniqueGlobalNodeID[i];

                  l = uniqueNodes[i-1][0];
                  lll = uniqueNodes[i][0];
```

```
                        NODE_Y(v) = (nodes[1][1] + distance)/100;
                        nodes[111][1] = nodes[1][1] + distance;

                        Message("new y = %g\n", NODE_Y(v));

                    }

                }
            }

}
```

Bed deformation routine – exponential model

```
#include "udf.h"

DEFINE_GRID_MOTION(check, d, dt, time, dtime)
{
      int currentTimeStep;
      currentTimeStep = N_TIME;


      if (currentTimeStep % 100 == 0 && currentTimeStep > 10)
      {
            /*parameters*/
            Thread *t = DT_THREAD (dt);
            face_t f;
            Thread *ct;
            cell_t c;
            Node *v;
            int n = 0;
            int xx;
            int mm = 0;
            real gridMotion[10000];
            Node *globalNodeID[10000];
            real mn, phi;
            real slopeCorrection;
            real txy, tzy, tres, ustar, settlingVelocity;
            real deformationConstant, maxScourPotential, scourPotential;
            real maxMn, maxSlopeCorrection;
            real nn;
            real NV_VEC(centroidRef), NV_VEC(transverse);
            real NV_VEC(faceNormal),NV_VEC(vecPlane), NV_VEC(newPoint);
            real alpha, beta;
            real a,b,e,k;
            real maxAllowableScourPotential, relativeRoughness;
            real maxDeformation;

            /*************************************************************/
            phi = 0.6; /*angle of repose*/
            maxAllowableScourPotential = 0.015; /*value of Mn corresponding
            to maximum allowable deformation*/
            relativeRoughness = 0.00853; /*ratio of mean particle diameter to
            mean depth*/
            maxDeformation = 0.002;/*maximum deformation per stage*/
            settlingVelocity = 0.10;/*settling velocity*/

            /*************************************************************/
            /*set deforming flag on adjacent cell zone*/
            SET_DEFORMING_THREAD_FLAG(THREAD_T0(t));

            /*************************************************************/
            /*loop for determining the maxScourPotential and corresponding Mn
            and slopeCorrection*/
            begin_f_loop(f,t)/*loop over all faces on boundary*/
            {
                  c = F_C0(f,t);/*cell next to boundary face*/
                  ct = THREAD_T0(t);/*thread of cell next ot boundary face*/
```

```
        /*compute movability number*/
        txy = (C_MU_L(c,ct) + C_MU_T(c,ct)) * (C_DUDY(c,ct) +
        C_DVDX(c,ct));
        tzy = (C_MU_L(c,ct) + C_MU_T(c,ct)) * (C_DWDY(c,ct) +
        C_DVDZ(c,ct));
        tres = sqrt(txy*txy + tzy * tzy);
        ustar = sqrt(tres/C_R(c,ct));

        mn = ustar/settlingVelocity;

        /*compute equation of face plane ax + bz + ey - q = 0*/
        F_CENTROID(centroidRef,f,t);
        F_AREA(faceNormal,f,t);

        a = -faceNormal[0];
        b = -faceNormal[2];
        e = -faceNormal[1];
        k = a * centroidRef[0] + b * centroidRef[2] + e *
        centroidRef[1];


        /*get line on the plane in the direction of the vector*/
        newPoint[0] = centroidRef[0] + C_U(c,ct); newPoint[2] =
        centroidRef[2] + C_W(c,ct);
        newPoint[1] = (k - a * newPoint[0] - b * newPoint[2]) / e;

        vecPlane[0] = C_U(c,ct); vecPlane[1] =  newPoint[1] -
        centroidRef[1]; vecPlane[2] = C_W(c,ct);

        /*angle vector on plane makes with the horizontal*/
        beta = atan( -vecPlane[1] / (sqrt(vecPlane[0]*vecPlane[0] +
        vecPlane[2]*vecPlane[2])));

        /*transverse vector*/
        NV_CROSS(transverse,faceNormal,vecPlane);

        /*transverse angle*/
        alpha = fabs(atan( transverse[1] /
        (sqrt(transverse[0]*transverse[0] + transverse[2]*
        transverse[2]))));

        /*slope correction*/
        if (beta < phi && alpha < phi)
        {
        slopeCorrection = sqrt (cos(beta)*(1 -
        (tan(beta)/tan(phi))) * cos(alpha) * sqrt(1 -
        (tan(alpha)*tan(alpha))/(tan(phi)*tan(phi))));
        }
        else
        {
              slopeCorrection = 1;
        }

        scourPotential = mn - 0.17 * slopeCorrection;

        if (scourPotential > maxScourPotential)
        {
              maxScourPotential = scourPotential;
              maxMn = mn;
              maxSlopeCorrection = slopeCorrection;
        }
}
end_f_loop(f,t)

/*************************************************************/
```

```
if (maxScourPotential >= maxAllowableScourPotential)
{
      deformationConstant = ((maxMn/maxSlopeCorrection) - 0.2405
      - 0.0066 * log(maxDeformation) - 0.204 *
      relativeRoughness)/0.0066;  /*determine deformation
      constant*/
}
else if (maxScourPotential < maxAllowableScourPotential &&
maxScourPotential > 0)
{
      deformationConstant = ((maxMn/maxSlopeCorrection) - 0.2405
      - 0.0066 * log(maxDeformation/maxAllowableScourPotential *
      maxScourPotential) - 0.204 * relativeRoughness)/0.0066;
}
else
{
      deformationConstant = 0;
}

/*************************************************************/
begin_f_loop(f,t)/*loop over all faces on boundary*/
{

      c = F_C0(f,t);/*cell next to boundary face*/
      ct = THREAD_T0(t);/*thread of cell next ot boundary face*/

      /*compute movability number*/
      txy = (C_MU_L(c,ct) + C_MU_T(c,ct)) * (C_DUDY(c,ct) +
      C_DVDX(c,ct));
      tzy = (C_MU_L(c,ct) + C_MU_T(c,ct)) * (C_DWDY(c,ct) +
      C_DVDZ(c,ct));
      tres = sqrt(txy*txy + tzy * tzy);
      ustar = sqrt(tres/C_R(c,ct));

      mn = ustar/settlingVelocity;
      Message("mn = %g\n", mn);

      /*slope correction*/
      /*compute equation of face plane ax + bz + ey - q = 0*/
      F_CENTROID(centroidRef,f,t);
      F_AREA(faceNormal,f,t);

      a = -faceNormal[0];
      b = -faceNormal[2];
      e = -faceNormal[1];
      k = a * centroidRef[0] + b * centroidRef[2] + e *
      centroidRef[1];

      /*get line on the plane in the direction of the vector*/
      newPoint[0] = centroidRef[0] + C_U(c,ct); newPoint[2] =
      centroidRef[2] + C_W(c,ct);
      newPoint[1] = (k - a * newPoint[0] - b * newPoint[2]) / e;

      vecPlane[0] = C_U(c,ct); vecPlane[1] =  newPoint[1] -
      centroidRef[1]; vecPlane[2] = C_W(c,ct);

      /*angle vector on plane makes with the horizontal*/
      beta = atan( -vecPlane[1] / (sqrt(vecPlane[0]*vecPlane[0] +
      vecPlane[2]*vecPlane[2])));

      /*transverse vector*/
      NV_CROSS(transverse,faceNormal,vecPlane);

      /*transverse angle*/
      alpha = fabs(atan( transverse[1] /
      (sqrt(transverse[0]*transverse[0] + transverse[2]*
      transverse[2]))));

      /*slope correction*/
```

```
                if (beta < phi && alpha < phi)
                {
                      slopeCorrection = sqrt (cos(beta)*(1 -
                      (tan(beta)/tan(phi))) * cos(alpha) * sqrt(1 -
                      (tan(alpha)*tan(alpha))/(tan(phi)*tan(phi))));
                }
                else
                {
                      slopeCorrection = 1;
                }

                Message("slopeCorrection = %g\n", slopeCorrection);


                /*set deforming flag on adjacent cell zone*/
                SET_DEFORMING_THREAD_FLAG(THREAD_T0(t));


                if (mn >= 0.17 * slopeCorrection)/*criterion for
                incipience*/
                {
                      f_node_loop(f,t,n)/*loop over face nodes*/
                      {
                            v = F_NODE(f,t,n);/*node pointer*/

                            if (NODE_POS_NEED_UPDATE(v) && NODE_Z(v) <
                            0.25)
                            {
                                  globalNodeID[mm] = v;
                                  gridMotion[mm]= exp((mn/slopeCorrection -
                                  0.2405 - 0.0066 * deformationConstant -
                                  0.204 * relativeRoughness)/0.0066);
                                  NODE_POS_UPDATED(v);
                                  mm++;
                            }
                      }
                }
          }
          end_f_loop(f,t)

          for (xx = 0; xx < mm; xx++)
          {
                NODE_Y(globalNodeID[xx]) -= gridMotion[xx];
          }

          /*************************************************************/

          adjustAngles(f, t, phi);

          modMaxAngles(f, t, phi);

    }
}


/*---------------------------------------------------------------------------*/
/*Function to adjust angles of relative nodes to ensure the maximum angles
are less than the angle of repose        */


void adjustAngles(face_t f,   Thread *t, real phi)
{
    Node *v;
    int n = 0;
    int ii = 0;
    int jj, kk;
    real max = 0;
    real min = 0;
    Node *pointer[4];
```

```
real nodes[4][3]; /*to store coordinates of nodes on a face*/
real angle, diffInY; /*variables for ensuring that face angles are less
than angle of repose*/
real watch; /*watch to check if all angles are less than angle of
repose*/


do
{
      watch = 0;
      max = 0;
      min = 0;
      begin_f_loop(f,t)
      {
            ii = 0;
            f_node_loop(f,t,n) /*get node coordinates*/
            {
                  v = F_NODE(f,t,n);/*node pointer*/
                  nodes[ii][0]= NODE_X(v);
                  nodes[ii][1]= NODE_Y(v);
                  nodes[ii][2]= NODE_Z(v);
                  pointer[ii] = v;
                  ii++;
            }

            /*check angles node vectors make with horizontal plane*/
            for (jj = 0 ; jj < 4 ; jj++)/*loop over nodes*/
            {
                  for(kk = 0 ; kk < 4 ; kk++)/*loop over nodes*/
                  {
                        if(kk > jj)/*check two different nodes without
                        repeating check for the same nodes*/
                        {
                              angle = atan((nodes[jj][1] -
                              nodes[kk][1])/(sqrt(pow((nodes[jj][0]-
                              nodes[kk][0]),2) + pow((nodes[jj][2]-
                              nodes[kk][2]),2))));

                              if (fabs(angle) > max)
                              {
                                    max = fabs(angle);
                              }
                              if (fabs(angle) < min)
                              {
                                    min = fabs(angle);
                              }

                              if (fabs(angle)*10000 > phi*10000)

                              /*check if angle is greater than angle of
                              repose*/
                              {
                                    diffInY = (sqrt(pow((nodes[jj][0]-
                                    nodes[kk][0]),2) +
                                    pow((nodes[jj][2]-
                                    nodes[kk][2]),2))) * tan(phi -
                                    0.001);
                                    if (nodes[jj][1] <
                                    nodes[kk][1])/*reduce angles*/
                                    {
                                          v = pointer[kk];
                                          NODE_Y(v) = nodes[jj][1] +
                                          diffInY;
                                          nodes[kk][1] = NODE_Y(v);
                                          watch = 1;
                                    }
                                    else
                                    {
                                          v = pointer[jj];
```

```
                                                NODE_Y(v) = nodes[kk][1] +
                                                diffInY;
                                                nodes[jj][1] = NODE_Y(v);
                                                watch = 1;
                                          }
                                    }
                              }
                        }
                  }
            }
            end_f_loop(f,t)
            Message("max = %g\n", max);
            Message("min = %g\n", min);

      }while(watch != 0);

}
/*--------------------------------------------------------------------------*/
/*Function to ensure that maximum plane angle is less than angle of repose*/


void modMaxAngles(face_t f,   Thread *t, real phi)
{
      Node *v;
      int n = 0;
      int ii = 0;
      real max = 0;
      real a,b,e,k;
      real node[4][3]; /*for nodes of plane*/
      real NV_VEC(centroidRef), NV_VEC(faceNormal);
      real NV_VEC(vecOne), NV_VEC(vecTwo);
      real watch; /*watch to check if all angles are less than angle of
      repose*/

            do{
            watch = 0;
            max = 0;

            begin_f_loop(f,t)
            {

            /*compute equation of face plane ax + bz + ey - d = 0*/
            f_node_loop(f,t,n)
            {
                  v = F_NODE(f,t,n);
                  node[ii][0] = NODE_X(v); node[ii][1] = NODE_Z(v);
                  node[ii][2] = NODE_Y(v);
                  ii++;
            }
            ii = 0;

            vecOne[0] = node[0][0] - node[2][0];
            vecOne[1] = node[0][2] - node[2][2];
            vecOne[2] = node[0][1] - node[2][1];

            vecTwo[0] = node[1][0] - node[3][0];
            vecTwo[1] = node[1][2] - node[3][2];
            vecTwo[2] = node[1][1] - node[3][1];

            NV_CROSS(faceNormal,vecOne,vecTwo);

            centroidRef[0] = (node[0][0] + node[1][0] + node[2][0] +
            node[3][0])/4;
            centroidRef[1] = (node[0][2] + node[1][2] + node[2][2] +
            node[3][2])/4;
            centroidRef[2] = (node[0][1] + node[1][1] + node[2][1] +
            node[3][1])/4;
```

```
a = -faceNormal[0]/2;
b = -faceNormal[2]/2;
e = -faceNormal[1]/2;
k = a * centroidRef[0] + b * centroidRef[2] + e * centroidRef[1];


if (acos(e/sqrt(a*a+b*b+e*e)) > (phi + 0.01))
{
      Message("angle before = %g\n", acos(e/sqrt(a*a+b*b+e*e)));

      e = sqrt((a*a + b*b) * cos(phi) * cos (phi) / (1 -
      cos(phi)*cos(phi)));


      if (node[0][2]< node[1][2] && node[0][2]< node[2][2] &&
      node[0][2]< node[3][2]){
            k = a * node[0][0] + b * node[0][1] + e * node[0][2];
      }

      if (node[1][2]< node[0][2] && node[1][2]< node[2][2] &&
      node[1][2]< node[3][2]){
            k = a * node[1][0] + b * node[1][1] + e * node[1][2];
      }

      if (node[2][2]< node[1][2] && node[2][2]< node[0][2] &&
      node[2][2]< node[3][2]){
            k = a * node[2][0] + b * node[2][1] + e * node[2][2];
      }

      if (node[3][2]< node[1][2] && node[3][2]< node[2][2] &&
      node[3][2]< node[0][2]){
            k = a * node[3][0] + b * node[3][1] + e * node[3][2];
      }


      f_node_loop(f,t,n) /*get node coordinates*/
            {
                  v = F_NODE(f,t,n);/*node pointer*/
                  NODE_Y(v) = (k - a * NODE_X(v)-b*NODE_Z(v))/e;
                  watch = 1;
      }

}
}
end_f_loop(f,t)
Message("max1 = %g\n", max);

}while(watch != 0);
}
```